Challenge Journal of STRUCTURAL MECHANICS

Vol.11 No.1 (2025)

auxetic buckling load building codes
compressive strength dynamic analysis
earthquake finite element method
girder bridge Jaya algorithm metaheuristic
algorithms modal analysis optimization
prestresing pushover analysis reinforced
concrete seismic design shallow foundations
smart concrete stability static analysis
steel structures structural dynamics
temperature effects thick plate wind

ISSN 2149-8024

TULPAR ACADEMIC PUBLISHING

Challenge Journal of Structural Mechanics

E-mail: *cjsmec@challengejournal.com*

Web page: *cjsmec.challengejournal.com*

Tulpar Academic Publishing
www.tulparpublishing.com

Challenge Journal of Structural Mechanics

CONTENTS

Research Articles

TULPAR ACADEMIC PUBLISHING

Challenge Journal of Structural Mechanics

Research Article

Combined effect of rice husk ash and animal bone powder on strength and permeability of concrete

Hasnain Mahmud [a,*], Towhid Ahmed [a], Md. Shafiqul Islam [a]

[a] *Department of Civil Engineering, Rajshahi University of Engineering & Technology, Kazla 6204, Rajshahi, Bangladesh*

ABSTRACT

Concrete is a key component of construction, and its demand is rising quickly along with infrastructural development. Although cement and aggregates are still essential components for making concrete, the production of cement greatly increases CO_2 emissions, necessitating the use of substitute materials to lessen the impact on the environment. As partial cement substitutes, rice husk ash (RHA) and animal bone powder (ABP) are viable alternatives. Animal bones, which are especially common in areas with high cattle populations, and rice husks, a byproduct of paddy production, are frequently discarded despite having useful qualities that can be used to improve concrete. With an emphasis on how they affect the material's permeability and strength, this thesis investigates the addition of RHA and ABP to concrete. Different RHA and ABP replacement amounts are examined through controlled experimentation to ascertain how they affect the properties of concrete following a predetermined curing period. The goal of this research is to determine the ideal combination that strikes a balance between environmental advantages and performance. In addition to improving the qualities of concrete, using RHA and ABP helps with waste management and pollution control. This strategy may help with sustainable building methods, reduce CO_2 emissions, and encourage efficient use of resources by lowering dependency on conventional cement.

ARTICLE INFO

Article history:
Received – August 22, 2024
Revision requested – November 6, 2024
Revision received – November 14, 2024
Accepted – November 22, 2024

Keywords:
Waste materials
Rice husk ash
Animal bone powder
Compressive strength
Permeability

Citation: Mahmud H, Ahmed T, Islam MS (2025). Combined effect of rice husk ash and animal bone powder on strength and permeability of concrete. *Challenge Journal of Structural Mechanics*, 11(1), 1–13.

1. Introduction

Of all the building materials used worldwide, concrete is the most widely used due to its distinct benefits over other materials (Swaminathen et al. 2021). An estimated 6 billion tonnes of ordinary concrete are manufactured annually worldwide (Mymrin et al. 2018). Unquestionably, cement plays a crucial role as the only binder in concrete, forming a solid substance that can support loads. It is vital to note that ordinary Portland cement has been a crucial component of concrete for over 200 years in the building industry (Ren et al. 2017). According to reports, the production of one tonne of Portland cement results in around one tonne of greenhouse gas emissions, and the cement manufacturing process accounts for 2% to 8% of the world's power usage (Zeyad et al. 2020). Cement is an essential component of concrete, and its production contributes approximately 5% to 8% of global carbon dioxide emissions (Alex et al. 2016). Waste materials such as rice husk ash, coconut shell, and fuel ash from palm oil are the most practical option for cement binders as they contain high pozzolanic property which supply reactive silica (Winnefeld et al. 2022). The goal is to reduce waste by using agricultural and industrial by-products as alternative binders, offering an environmentally friendly solution to waste management that avoids harmful and costly disposal methods like incineration and landfilling (AlBiajawi et al. 2022). The evolving lifestyle of modern society has resulted in the generation of various types of waste, which can impact the environ-

* *Corresponding author*. Tel.: +880-191-166-4427 ; E-mail address: 1800164@student.ruet.ac.bd (H. Mahmud)
ISSN: 2149-8024 / DOI: https://doi.org/10.20528/cjsmec.2025.01.001

ment at different scales if not managed properly (Derki and Akpınar 2023). In recent years, there has been a significant surge in research efforts focused on waste recycling, encompassing both investigative studies and practical implementations (Çelik et al. 2024; Şengel et al. 2022; Canbaz et al. 2021). Each tonne of rice typically yields 200 kilograms of rice husks, which when fully burned, create 40 kg of rice husk ash (RHA). Nearly 320,000 tonnes/year of RHA might be generated in the area, according to a hard estimate, hence suitable alternative disposals need to be prepared to prevent negative environmental effects (Zerbino et al. 2011). According to world rice production by country, about 36.4 million metric tonnes, third in the world (Table 1). Again 513.68 million tonnes of rice are produced in worldwide (Khanal 2021).

About 20% of rice's weight is made up of rice husk. Furthermore, every year, about 150 million tonnes of rice husk are produced (Kordi et al. 2024). Rice husk ash, rich in silica, can replace a portion of cement in concrete, improving its mechanical and durability properties by up to 30% (Zerbino et al. 2011). RHA is a highly reactive pozzolanic substance that is produced by burning nice at temperatures below 700 °C in a regulated marine environment. Its content of amorphous silica is high (Jaya et al. 2012). Animal bones, often discarded as waste from the meat industry, can be repurposed as partial replacements for fine or coarse aggregates in concrete. This approach not only helps reduce environmental pollution but also explores the potential for producing high-quality concrete structures using crushed animal bones, as researched by various scientists. (Petrounias et al. 2021). According to Department of Livestock Services of Bangladesh (2024) (Table 2), total cattle production in Bangladesh is about 24.856 million and total ruminant production in Bangladesh is about 57.143 million (Salim 2022).

Table 1. World rice production by country (10^3 tonnes) (World Population Review 2024).

Country	2021	2020	2019
China	212,843	211,860	209,614
India	195,425	186,500	174,717
Bangladesh	56,945	54,906	54,586
Indonesia	54,415	54,649	54,604
Vietnam	43,853	42,765	43,495
Thailand	33,582	30,231	28,618
Myanmar	24,910	25,983	26,270
Philippines	19,960	19,295	18,815
Pakistan	13,984	12,630	11,120
Brazil	11,661	11,091	10,369
Cambodia	11,410	11,248	10,886
Japan	10,525	10,469	10,527

Table 2. Livestock population of Bangladesh (in million) (Salim 2022).

Name of species	2013-14	2014-15	2015-16	2016-17	2017-18	2018-19	2019-20	2020-21	2021-22	2022-23
Cattle	23.488	23.636	23.785	23.935	24.086	24.238	24.391	24.545	24.700	24.856
Buffalo	1.457	1.464	1.471	1.478	1.479	1.486	1.493	1.500	1.508	1.516
Sheep	3.206	3.270	3.335	3.401	3.468	3.537	3.607	3.679	3.752	3.827
Goat	25.439	25.602	25.766	25.931	26.100	26.267	26.435	26.604	26.774	26.945
Total ruminant	53.590	53.972	54.357	54.745	55.133	55.528	55.926	56.328	56.734	57.143

In the year 2022, Bangladesh produced 209,016 thousand tonnes of meat from cattle and buffalo. From 1973 to 2022, Bangladesh's production of beef and buffalo meat increased at an average yearly rate of 1.04%, from 137,047 thousand tonnes to 209,016 thousand tonnes (Bangladesh Production of Beef and Buffalo Meat, 1961-2023 - knoema.com, 2024). One of the waste materials taken out of butchered animals (cows and oxen) is bone, which has a high calcium concentration. Conversely, calcium oxide makes up 60% to 67% of portland cement (Getahun and Bewket 2021). If deemed appropriate, using cow bones in place of fine aggregate will aid in environmental cleanup and the transformation of waste into wealth. When working with concrete, one might assume that the ratio of cement to water is inversely proportional to the concrete's strength, provided that full compaction is maintained at a specific age and standard temperature (Neville and Brooks 1987). A study on rice husk ash (RHA) as a Portland cement substitute found that 10-15% RHA optimizes mortar strength. Lower temperatures yield amorphous RHA, enhancing strength through calcium silicate hydrate (C-S-H) gel formation. Higher RHA levels above 10% reduce strength due to limited calcium hydroxide ($Ca(OH)_2$) and increased porosity. White RHA, burnt below 800 °C, showed the best performance, especially in seawater, due to more C-S-H gel but is constrained by $Ca(OH)_2$ availability for the reaction. The ideal RHA content for cement mortar is around 15% for balanced strength and binder properties (Zhao et al. 2022). The study used river sand and 20mm crushed rock as aggregates, borehole water, and Portland composite cement for testing. Animal bone ash, processed through drying and controlled burning, was mixed in proportions of 1:2:4 with a 0.6 water-to-cement ratio. Cast specimens measured 150mm cubed. Over 28 days, compressive strength peaked at 23.43 N/mm^2 with 5% bone ash, but dropped to 16.49 N/mm^2 at 20%. The findings suggest that up to 5% animal bone ash is viable for lightweight structures, as higher percentages weaken the material (Zhao et al. 2022). The study indicates that replacing cement with animal bone powder (ABP) in concrete reduces compressive, split tensile, and flexural

strengths as ABP content increases. For control samples (0% ABP), compressive strength increased with age, peaking at 33.63 MPa at 28 days. However, with 5%, 10%, 15%, and 20% ABP, compressive strength significantly declined. Similarly, split tensile and flexural strengths also decreased with higher ABP percentages. The study found that 5% ABP replacement yielded comparable strength to the control, and 10% ABP replacement achieved required strength standards, making up to 10% ABP viable without compromising concrete strength (Teshome et al. 2019). The study shows that replacing cement with animal bone powder (ABP) reduces concrete strength and workability as ABP dosage increases. An optimal 10% ABP replacement maintains acceptable strength and workability, making it the best balance for concrete mixes while ensuring desired performance characteristics (Makebo 2019). In this study, four concrete mix ratios were created, with one control mix (0% RHA) and three mixes containing 10%, 15%, and 20% rice husk ash (RHA) as partial cement substitutes. The water volume (225.5 kg/m^3), coarse aggregates (590 kg/m^3), fine aggregates (910 kg/m^3), superplasticizer concentration (1%), and water-to-binder ratio (0.41) remained constant. Each mix produced nine cubes (150x150x150 mm) and nine cylinders (300x150 mm) for compressive and tensile strength tests at 7, 28, and 56 days. Rapid chloride permeability tests at 28 days showed reduced ion penetration with higher RHA content, except at 20% RHA. The 10% RHA mix demonstrated exceptional chloride ion resistance (Chopra et al. 2015).

2. Research Significance

This study explores the replacement of cement with Rice Husk Ash (RHA) and Animal Bone Powder (ABP) to assess sustainable advantages in construction, focusing on resource conservation, waste management, environmental impact, energy efficiency, and cost reduction. By substituting cement with RHA and ABP, limestone consumption is reduced, supporting resource conservation and sustainability. RHA, typically used in landfills, decomposes slowly and offers limited ecological benefits, while ABP, rich in calcium oxide, can be managed more effectively as a binding agent, reducing solid waste issues. Environmentally, using RHA and ABP as partial cement replacements decreases carbon emissions from cement production, lessening greenhouse gases. Lower cement demand conserves energy, while the local availability and low cost of RHA and ABP help to minimize construction expenses. This research thus presents RHA and ABP as viable, sustainable alternatives to traditional cement in construction.

3. Materials and Method

3.1. Experimental materials

To get desired quality of silica from RHA it needs to burn at the temperature of 700 °C to 800 °C. Fresh rice husk cannot deliver silicious material required for developing proper chemical bond.

Animal Bone contains calcium which is required to transform as calcium oxide. So, it is required to apply heat about 300 °C to 400 °C. Applying heat also helps to remove biological organism.

3.1.1. Rice husk ash processing

RHA is frequently utilized as a supplemental cementitious material (SCM) in concrete applications to partially replace portland cement. RHA is rich in silica which acts as pozzolanic compound that can chemically react with calcium hydroxide ($Ca(OH)_2$) in the presence of water. Calcium hydroxide generated during cement hydration, resulting in the formation of more calcium silicate hydrate (C-S-H) gel. This procedure lowers the heat of hydration and the possibility of an alkali-silica reaction (ASR) while also increasing the concrete's strength, durability, and chemical resistance. Because RHA is a byproduct of the combustion and rice milling processes, it reduces waste and greenhouse gas emissions, making it an environmentally beneficial substance. The application of this material in building processes promotes environmentally friendly building practices and efficient use of resources.

After collection of raw rice husk, it was heated at 700 °C to 800 °C in gas furnace. Then it was sieved through #100 sieve to mix with cement for mix design. Silicon was the main element after oxygen in RHA. The chemical composition of the utilized rice husk ash is provided in Table 3.

Processed rice husk ash is shown in Fig. 1 and chemical analysis test result is presented in Fig. 2 which was conducted in JCM-6000PLUS machine.

Table 3. Chemical composition of the utilized RHA.

Element	Mass (%)	Atom (%)
O	70.99	81.27
Si	24.76	16.15
Na	0.13	0.10
Mg	1.98	1.49
S	0.18	0.10
Ca	0.17	0.08
Al	---	---
K	1.58	0.74
Fe	0.22	0.07

Fig. 1. Rice husk ash (RHA).

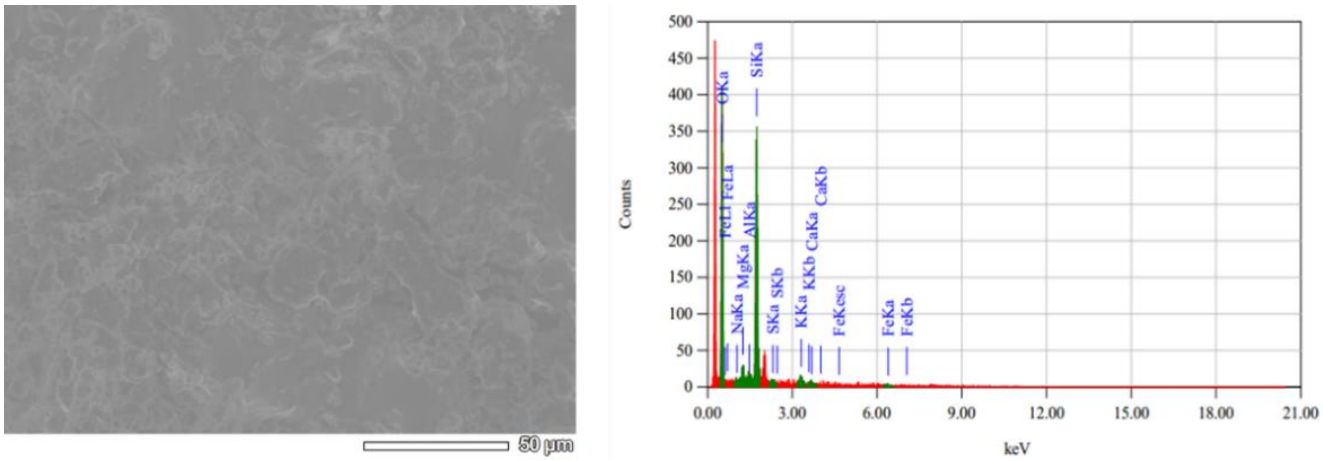

(a) EDS test result (b) EDS test graph

Fig. 2. Chemical analysis of rice husk ash (instrument: JCM-6000PLUS).

3.1.2. Animal bone powder processing

Animal bones are processed and pulverized into a fine powder, which is known as animal bone powder. Usually, to make it, animal bones are cleaned, dried, and burned to remove biological materials. Then, the bones are ground into a fine powder. Animal bone powder is a significant addition to a variety of industries, including agriculture, animal feed, and construction materials. It is rich in minerals including calcium and phosphorus. Animal bone powder has the potential to provide advantages including increased strength and durability when used in place of some of the cement in concrete mixes.

After collection of ABP, it was sun-dried for 2 to 3 days. Then it was grounded through grinding machine and made smaller pieces of size. It was further grounded and sieved into powdered consistency. Next it was heated 300 °C to 400 °C to remove biological organism and calcinated. Then it was sieved again to mix with cement for mix design. The chemical composition of the animal bone powder is provided in Table 4.

Table 4. Chemical composition of the ABP.

Element	Mass (%)	Atom (%)
O	68.43	83.60
Ca	27.93	13.62
Na	0.48	0.41
Mg	1.32	1.06
Al	0.75	0.54
Si	1.09	0.76
K	---	---
Fe	---	---

Processed animal bone powder is shown in Fig. 3 and chemical analysis test result is presented in Fig. 4 which was conducted in JCM-6000PLUS machine.

3.1.3. Cement

Cement, a hydraulic binder, or finely powdered inorganic components combined with water to create a paste that sets and hardens through hydration reactions and processes and maintains its strength and stability even in the presence of water (Atiş and Karahan 2009).

All 27 cement family products covered by EN 197-1 (2011) are further categorized into five primary cement types. For this study CEM-I/BM (Ordinary Portland Cement (OPC)) was used and collected from the concrete laboratory of Civil Engineering Department, RUET, Rajshahi.

3.1.4. Sand

The key component of concrete made of crushed stone or natural sand is fine aggregate. They were mostly utilized to close in spaces left by the coarse aggregate. Sand of FM (2.36) was utilized for this project's fine aggregate.

3.1.5. Coarse aggregate

As natural crushed stone that was passed through 19.0 mm sieve and retain on 12.7 mm sieve was employed in this project (as per ASTM C136 2005).

Fig. 3. Animal bone powder (ABP).

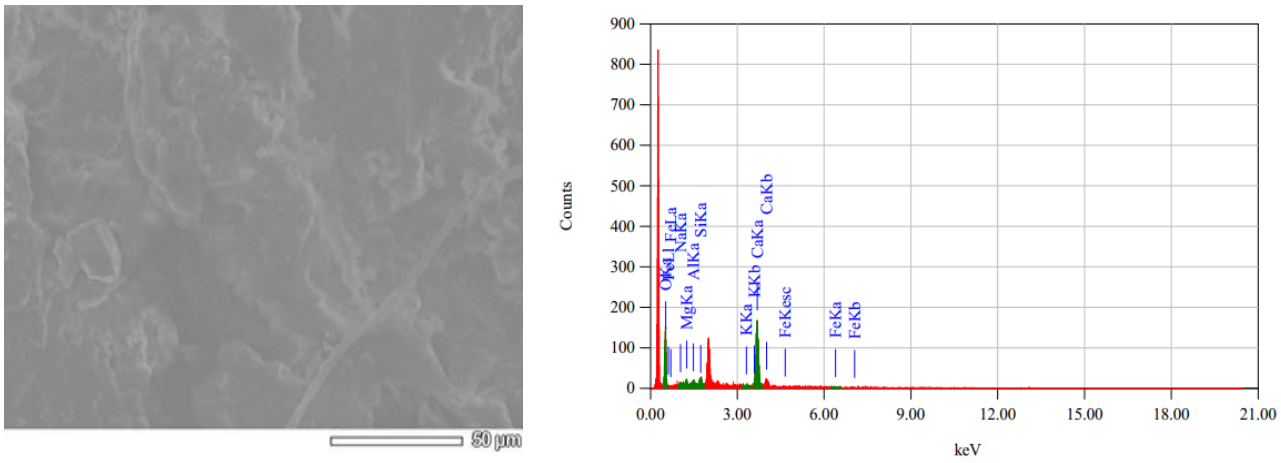

(a) EDS test result (b) EDS test graph

Fig. 4. Chemical analysis of animal bone powder (instrument: JCM-6000PLUS).

3.2. Sample preparations

3.2.1. Specimen size

A total of 9 types of composition were created using batched by weight method for conducting two tests, each of the compositions had different amounts of ABP and RHA by replacing fine aggregate. Before mixing, the various components of concrete are typically proportioned by weight or volume, a process known as batching. According to this study, the most often utilized technique for producing concrete in Bangladesh and the majority of developing countries is batching by weight.

The unit weight of each concrete specimen was measured after 28 days curing in SSD condition. Table 5 provides an overview of all experimental parameters and displays the entire experimental schedule.

Table 5. Experimental parameters for the test specimens.

Test name	Specimen size (cylindrical)	Curing ages
Compressive strength test	100 mm x 200 mm	28 days
Water permeability test	100 mm x 200 mm	28 days

3.2.2. Concrete mixing and casting

Cylinders (100mm diameter x 200mm height) for compressive strength and water permeability test. For every combination, 3 cylindrical samples were prepared for compression test as well as for water permeability test. For mixing from 12.7 mm to 19 mm size of NCA were used.

9 types of concrete mix were prepared replacing Cement (by weight) with different proportion of ABP and RHA. The mix proportions of different compositions of ABP and RHA with their water cement ratio are described in Table 6.

Before casting the NCA was soaked in water for 24 hours then dried in room temperature for SSD condition. All the specimens were casted according to ASTM C39 (2021). After the mixing the slump value of each mix was noted. Test specimens were completed with a steel trowel after casting. Every test specimen was kept in storage for 24 hours. Then the casing of each cylindrical sample was removed. The preparation of concrete cylinders and the slump value test are shown in Figs. 5 and 6.

Table 6. Different compositions of ABP and RHA.

Combination	ABP	RHA	Cement (OPC)	W/C ratio
1	0%	0%	100%	0.5
2	0%	5%	95%	0.5
3	0%	10%	90%	0.5
4	5%	0%	95%	0.5
5	5%	5%	90%	0.5
6	5%	10%	85%	0.5
7	10%	0%	90%	0.5
8	10%	5%	85%	0.5
9	10%	10%	80%	0.5

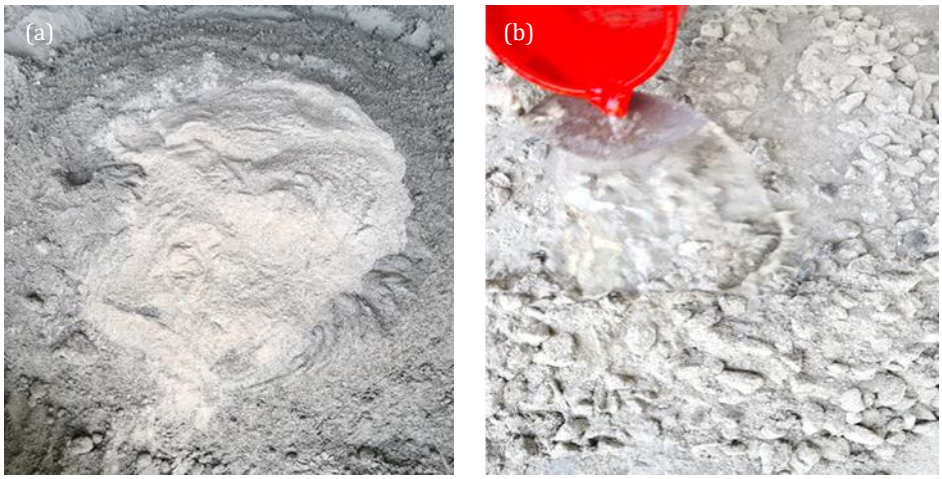

Fig. 5. Mixing of concrete for casting: (a) Mixing dry ingredient; (b) Adding water with mix.

Fig. 6. Measuring the slump value of the concrete mix.

3.2.3. Curing procedure

The pond method of curing was used in which the cylindrical sample were totally immersed in water throughout the curing period. After being cured in water for 28 days, the specimens were removed, and a cutting machine was used to smooth the cylinder's top and bottom surfaces. Cutting process and curing of concrete (after smoothing) is shown in Fig. 7.

3.3. Test methods

3.3.1. Standards for tests

In this investigation, batched by weight have been adopted as the most commonly used method in concrete production in Bangladesh and most developing nations (Table 7).

Fig. 7. (a) Cutting of specimen; (b) Ponding method for curing of specimen.

Table 7. Standards for tests.

Test name	Standards
Compressive strength test	ASTM C39 (2021)
Water permeability test	IS 516 (2018)

3.3.2. Unit weight of sample

After the curing process, the sample was removed from the water and allowed to dry at ambient temperature for half an hour in order to remove any remaining water from the cylinder. The sample was weighed in a balance and the weight was noted in order to assess the sample's unit weight or density. Load measurement was done in weight machine which is shown in Fig. 8.

The unit weight or density of the sample is carried by Eq. (1).

$$\rho = \frac{M}{V} \tag{1}$$

where M is the mass or weight, and V is the volume of the sample.

Fig. 8. The load-measuring method of the test specimen.

3.3.3. Compressive strength test

Compression strength is the ability of concrete to bear loads applied to it without breaking or deflecting. It is possible to evaluate compression strength while adhering to multiple codes, including IS 516 (2018), BS EN 12390-3 (2019), and ASTM C39 (2021). The compression test was carried out in this work, per ASTM C-39 (2021). The compressive strength of the cylindrical specimens was determined using a 2000kN compression machine. The samples were added one at a time. The specimen's composition was recorded before to applying load, and the highest load the specimen could withstand was subsequently noted. Eq. (2) determines the concrete cylinder's ultimate compressive strength after 28 days of curing.

$$f = \frac{F}{A} \tag{2}$$

where F is the recorded load, and A is the cross sectional area of the cylindrical specimen.

The ASTM C39 (2021) test technique involves placing concrete cylinders under a compressive axial load at a rate that stays within a specified range until failure happens. The specimen's compressive strength is determined by dividing the maximum load reached by the specimen's cross-sectional area. This shows the sample both during and after the compression test, as well as the testing apparatus used for the test. It also indicates the sample's failure pattern. Fig. 9 shows the breaking of mould during compressive strength test.

Fig. 9. Sample during compressive strength test.

3.3.4. Water permeability test

Before testing, the specimens were removed from the curing environment and allowed to equilibrate to room temperature. Surface irregularities or imperfections was carefully smoothed or corrected to ensure uniform contact with testing equipment. The water permeability test apparatus typically consists of a chamber or container capable of holding the specimen, along with a water supply system and pressure monitoring equipment. The cylindrical concrete specimen is securely placed in the testing apparatus, ensuring that there are no leaks or gaps

between the specimen and the apparatus walls. Water is then applied to one side of the concrete specimen under controlled pressure. This pressure simulates the hydraulic head or hydrostatic pressure that the concrete would experience in service conditions. The pressure is gradually increased until it reaches the desired level for testing. It was 5 kg/sq.mm for this test procedure. Then the specimens were brought out and sent to UTM for split testing. After splitting, the depth of water entered into the concrete specimen is measured in millimeter scale.

Fig. 10 presents the water permeability testing machine and Fig. 11 shows the procedure of different steps during conducting of the water permeability test.

4. Results and Discussion

All the data that are found from strength test and permeability test, workability test, unit weight test are organized here in different tables. Analyzing these data, the effectiveness of our experiment is discussed based on test results.

Fig. 10. Water permeability testing machine.

Fig. 11. Water permeability test procedure: (a) Specimen placing; (b) Splitting; (c) Marking; (d) Measuring.

4.1. Workability

Table 8 provides an overview of the specimen's slump value. Here the results for 5%B-5%R slump value is the best match for the purpose of the research.

From Table 8 and Fig. 12, workability is observed to increase as the percentage of animal bone powder in concrete rises, but it decreases when the percentage of rice husk ash in concrete increases. It is due to the rice husk ash is a siliceous material which can increase the bond strength in cement to make bond and harden faster. On the other hand, animal bone powder contains CaO that will tend to make strong chemical bond that shows higher slump value.

Therefore, presence of excess amount of ABP can increase workability but excess RHA decreases workability. RHA and ABP also worked as filler materials in concrete by filling voids between coarse and fine aggregates, leading to improved density and reduced porosity.

Table 8. Slump values of different concrete mixes.

Concrete mix	Slump value (mm)
0%B-0%R	76
5%B-0%R	79
0%B-5%R	73
5%B-5%R	74
0%B-10%R	69
10%B-0%R	82
10%B-5%R	81
5%B-10%R	83
10%B-10%R	86

B: Animal bone powder; R: Rice husk ash

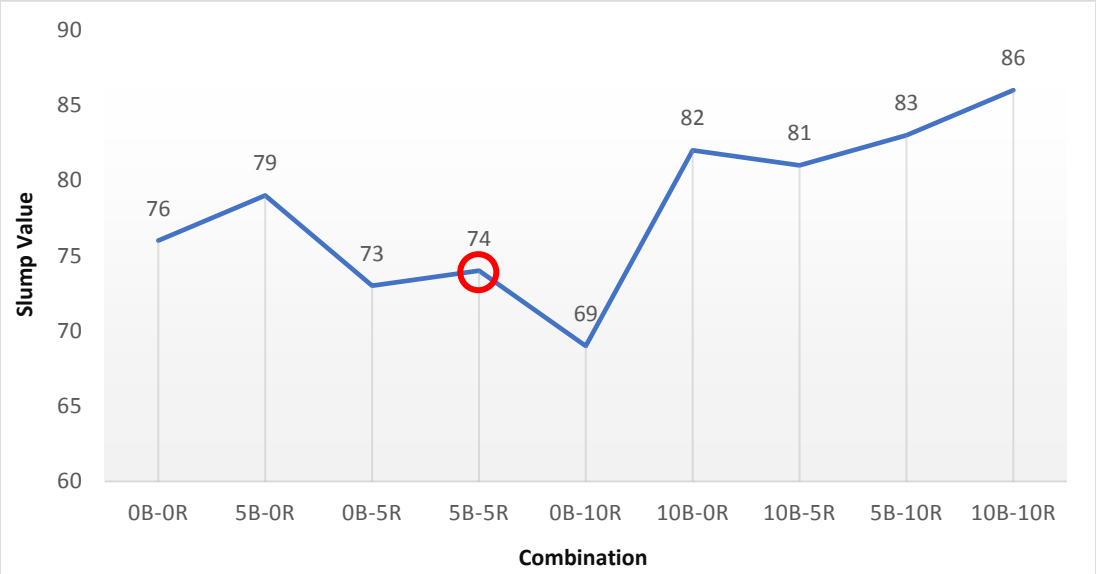

Fig. 12. Workability of concrete with the partial replacement of cement by ABP and RHA.

4.2. Unit weight

Table 9 provides the results that 5%B-5%R weight value is the best match for the purpose of the research.

From Table 9 and Fig. 13, it was observed that specific weight decreases with the increment of RHA and ABP. The unit weight decreases more when ABP is used as a partial replacement. We can come to a decision that unit weight of RHA is more than ABP and it reduces the weight of the structure.

4.3. Compressive strength

The test for compressive strength complies with the code that was previously covered in the above chapter. Table 10 provides the results that 5%B-5%R compressive strength value is the best match for the purpose of the research.

Table 9. Unit weight of cylindrical concrete specimens.

Concrete mix	Unit weight (g/cm^3)
0%B-0%R	2.409
5%B-0%R	2.318
0%B-5%R	2.367
5%B-5%R	2.373
0%B-10%R	2.369
10%B-0%R	2.271
10%B-5%R	2.245
5%B-10%R	2.241
10%B-10%R	2.255

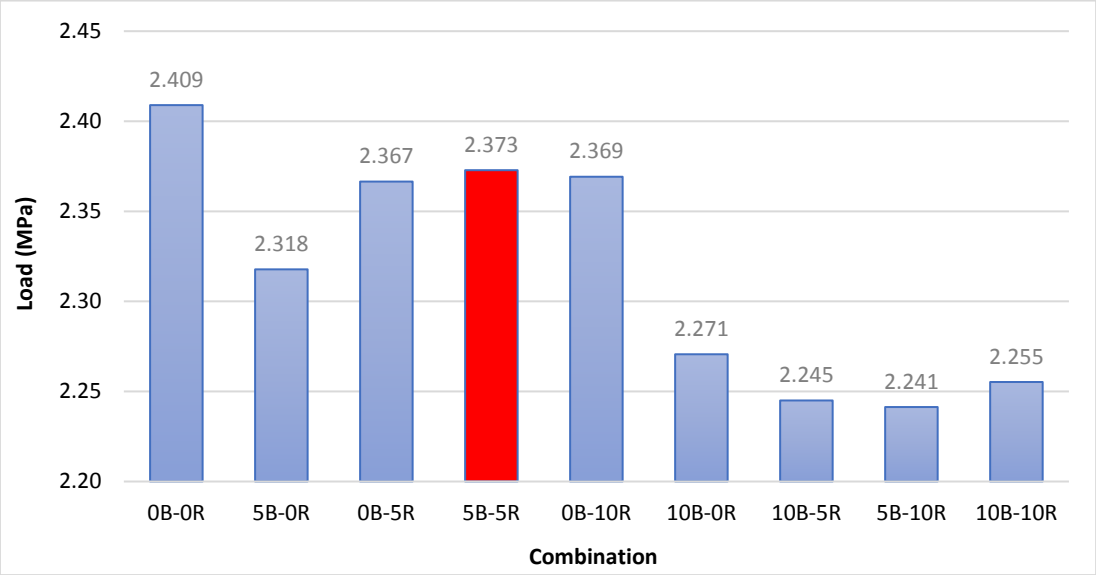

Fig. 13. Unit weight of different concrete mix with RHA and ABP (28 days of age).

Table 10 and Fig. 14 demonstrates that as the amount of RHA and ABP replacement for cement increases, the compressive strength of concrete after 28 days of curing increases for some combination and then decreases for other combination. This may be due to when RHA and ABP is sufficient amount to react and make C-S-H gel then strength increases and when it is much more then strength decreases.

Minimum concrete strength for structural application of reinforced concrete must be 20 N/mm^2. However, for structures up to 4 story, the minimum concrete strength may be decreased to 17 N/mm^2 (BNBC 2020).

According to this code, we can use the combination of 5%B-5%R and 0%b-5%R for the sufficient strength and 5%B-0%R AND 0%B-10%R for the low strength concrete. Other combination can be used for the light weight structure.

Table 10. Variation of compressive strength of concrete replacing cement with ABP and RHA.

Concrete mix	Avg. comp. strength (MPa)
0%B-0%R	21.73
5%B-0%R	19.47
0%B-5%R	22.25
5%B-5%R	22.87
0%B-10%R	17.66
10%B-0%R	14.31
10%B-5%R	15.22
5%B-10%R	15.76
10%B-10%R	13.51

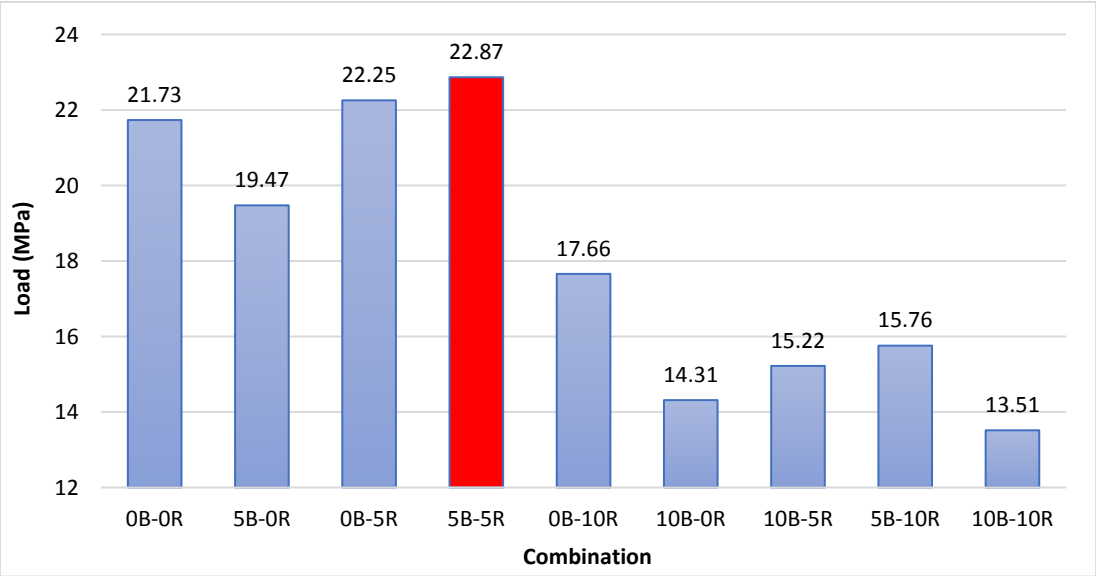

Fig. 14. Compressive strength of different concrete mix after 28 days curing.

4.4. Water permeability

The test for water permeability complies with the code that was previously covered in the above chapter. Table 11 provides the results that 5%B-5%R permeability value is the best match for the purpose of the research. RHA and ABP is sufficient amount to react and make C-S-H gel then permeability decreases and when it is much more then permeability decreases which is shown in Table 11 and Fig. 15.

4.5. Combined effect of permeability and strength

From Table 12 and Fig. 16, it can be seen that as the RHA and ABP both are used up to 5% the strength and permeability increases. When the amount goes beyond that then the compressive strength and the permeability usually decreases. For some specific and special cases, we can use the low permeable and low strength concrete. For the replacement of both 5%, we get the most impressive result.

Table 11. Variation of water permeability of concrete replacing cement with ABP and RHA.

Concrete mix	Avg. permeability (mm)
0%B-0%R	9.1
5%B-0%R	8.9
0%B-5%R	8.2
5%B-5%R	7.4
0%B-10%R	9.5
10%B-0%R	10.2
10%B-5%R	11.5
5%B-10%R	10.9
10%B-10%R	13.2

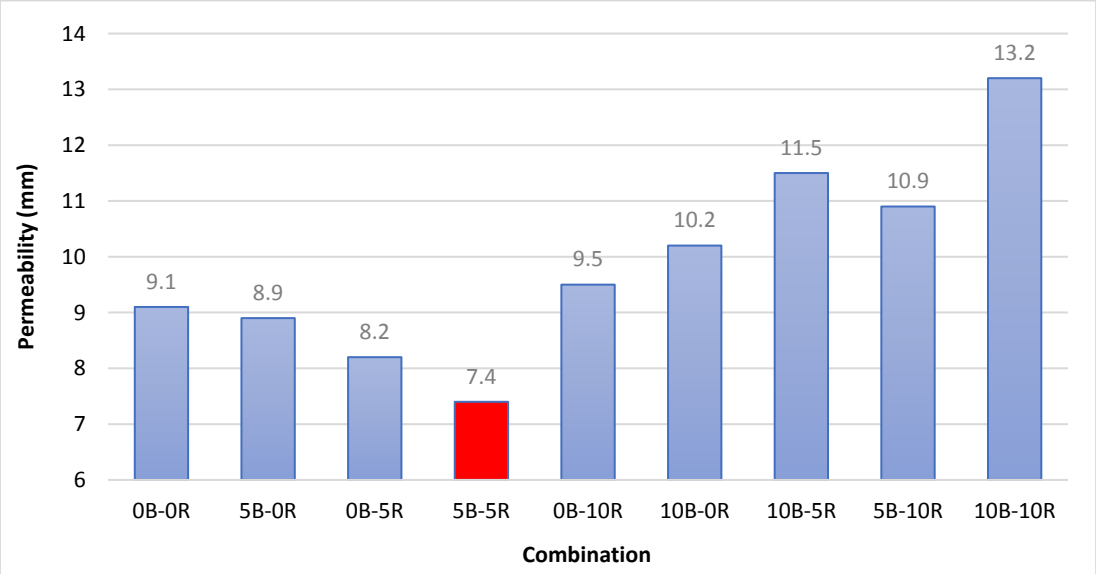

Fig. 15. Water permeability of different concrete mix after 28 days curing.

Table 12. Combined result of replacing cement with RHA and ABP.

Concrete mix	Avg. comp. strength (MPa)	Avg. permeability (mm)
0%B-0%R	21.73	9.1
5%B-0%R	19.47	8.9
0%B-5%R	22.25	8.2
5%B-5%R	22.87	7.4
0%B-10%R	17.66	9.5
10%B-0%R	14.31	10.2
10%B-5%R	15.22	11.5
5%B-10%R	15.76	10.9
10%B-10%R	13.51	13.2

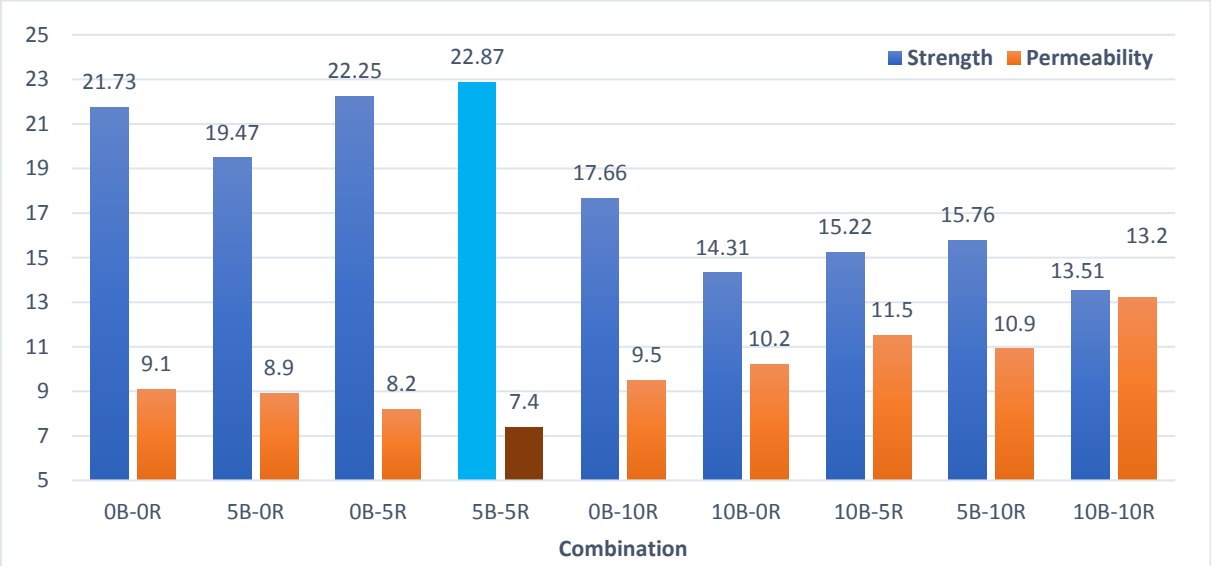

Fig. 16. Combined effect of ABP and RHA concrete mix after 28 days curing.

In consideration with the literature review, it can be seen that in these two different tests conducted for RHA and ABP separately the strength is higher up to 5%, sometimes up to 10% replacement of the materials. Permeability decreases for the increase of RHA but increase for the increment of ABP. However, in this experiment both the ingredient has been mixed and the result found for the 5% RHA and 5% ABP provides the best result in terms of strength and permeability.

5. Conclusions

The analysis focused on the compressive strength and water permeability of the replacement of ABP and RHA in some portion of cement, examining the result with varying percentage of ABP and RHA (0%, 5%, 10%). The samples exhibited the following characteristics:

- Compared to a concrete cylinder the compressive strength of concrete, 5% RHA and 5%ABP-5%RHA curing for 28 days, yielding values of 22.25 MPa, 22.87 MPa respectively. These recorded compressive strengths represent the average maximum strengths achieved in the study.
- Compared to a concrete cylinder permeability of concrete, with the incorporation of cement by at the combination RHA and ABP of preferred percentages of 5%ABP-0%RHA, 0%ABP-5%RHA, 5% ABP-5% RHA at 28 days, resulting in 8.9mm, 8.2mm, 7.4mm respectively. The recorded results show that increase in compressive strength decreases in permeability.
- Compared to unit weight, the unit weight gradually decreases as the combination of RHA and ABP increases. From the test result it is observed that unit weight of the concrete containing RHA relatively higher than concrete containing ABP. The workability decreases with the reduction of the amount of the cement.

By testing the cylindrical specimen containing RHA and ABP we can observe that the compressive strength of concrete containing 5% RHA and 5% ABP increases by more than 3% than that of contain cement. For the specimen that contain only 5% RHA increases the strength by more than 2.5%. If we consider about the water permeability of concrete then the concrete specimens contain only 5% RHA, only 5% ABP, 5% ABP-5% RHA improves its permeability approximately by 2.20%, 9.89% and 18.68%. This phenomenon occurs when the ABP and RHA construct C-S-H gel that is liable for the larger compressive strength. Larger C-S-H gel helps to restrict the water permeability. RHA also works as a finer filler particle. That also helps to minimize the porous structure of the concrete leads to less permeability. When the more partial material is added then the strength decreases due to insufficient amount of reactant is present for proper chemical reaction. That also leads to the make the structure more porous leads to more permeable to water.

Due to limitation of time the study was concluded only with the observation of workability, unit weight, compressive strength, permeability of concrete. Perhaps, the study can be further enriched with the following additional work:

- Investigation of strength behavior of concrete using ABP and RHA in replacement of cement above 10-30 percent by weight.
- Observation of the flexural behavior of concrete by split tensile test using ABP and RHA in replacement of cement up to a certain percentage.
- The test was performed for cylindrical specimen, but it can be also performed for cubical specimen.
- Further work should be done to cover rapid chloride penetration test, water absorption, freeze-thaw durability and abrasion etc.
- Inspection of mechanical strength properties of concrete using different properties such as silica fume, fly ash, ceramic particle, egg shale etc.
- Different water cement ratio can be used.
- Evaluation of concrete's durability and life cycle assessment with the addition of different combination of ABP and RHA seems they are environmentally friendly.

Acknowledgements

The authors would like to thank Md. Mahbubul Alam from Bengal Meat Processing Industries Ltd. because of invaluable assistance in providing some of raw materials for the research.

Funding

The authors received no financial support for the research, authorship, and/or publication of this manuscript.

Conflict of Interest

The authors declared no potential conflicts of interest with respect to the research, authorship, and/or publication of this manuscript.

Author Contributions

All of the authors made substantial contributions to conception and design, or acquisition of data, or analysis and interpretation of data; were involved in drafting the manuscript or revising it critically for important intellectual content; and gave final approval of the version to be published.

Data Availability

The datasets created and/or analyzed during the current study are not publicly available, but are available from the corresponding author upon reasonable request.

Ethics Approval and Consent to Participate

This study was approved by the ethics committee of Rajshahi University of Engineering and Technology. All methods were performed in accordance with relevant guidelines and regulations.

REFERENCES

AlBiajawi MI, Embong R, Muthusamy K (2021). An overview of the utilization and method for improving pozzolanic performance of agricultural and industrial wastes in concrete. *Materials Today Proceedings*, 48, 778–783.

Alex J, Dhanalakshmi J, Ambedkar B (2016). Experimental investigation on rice husk ash as cement replacement on concrete production. *Construction and Building Materials*, 127, 353–362.

ASTM C39 (2021). Standard test method for compressive strength of cylindrical concrete specimens. ASTM International, West Conshohocken, PA.

ASTM C136 (2005). Standard test method for sieve analysis of fine and coarse aggregates. ASTM International, West Conshohocken, PA.

Atiş CD, Karahan O (2008). Properties of steel fiber reinforced fly ash concrete. *Construction and Building Materials*, 23(1), 392–399.

BNBC (2020). Minimum concrete strength. Bangladesh National Building Code, Part VI, Chapter 5, 3428. Department of Housing and Public Works, Dhaka, Bangladesh.

BS EN 12390-3 (2019). Testing hardened concrete. Compressive strength of test specimens. British Standards Institution, London, UK.

Canbaz M, Kara İ, Topçu İ (2021). Effect of high temperature on the mechanical behavior of cement-bonded wood composite produced with wood waste. *Challenge Journal of Structural Mechanics*, 7(1), 42–48.

Çelik Z, Turan E, Oltulu M, Öner G. (2024). Reinforcement of concrete beams using waste carbon-nanoclay-fiberglass laminate pieces. *Challenge Journal of Concrete Research Letters,* 15(1), 1–6.

Derki A, Akpınar P (2023). An overview on the hazards and handling methods of construction and demolition wastes: Special focus on recycled concrete aggregates. *Challenge Journal of Concrete Research Letters,* 14(4), 118–127.

Chopra D, Siddique R, Kunal N (2015). Strength, permeability and microstructure of self-compacting concrete containing rice husk ash. *Biosystems Engineering*, 130, 72–80.

Department of Livestock Services (2024). Livestock Economy at a Glance. https://dls.portal.gov.bd/ [accessed 13-06-2024].

EN 197-1 (2011). Cement - Part 1: Composition, specifications and conformity criteria for common cements. European Committee for Standardization, Brussels, Belgium.

Getahun, S., & Bewket, B. (2021). A Study on Effect of Partial Replacement of Cement by Cattle Bone Ash in Concrete Property. *Jurnal Teknik Lingkungan : Electronic Journal of Civil and Environmental Engineering*, *11*(2), 1–6.

IS 516 (2018). Method of tests for strength of concrete. Bureau of Indian Standards, New Delhi, India.

Jaya RP, Nor MAAM, Ahmad ZA, Amin ZM (2012). Properties of Mortar containing rice husk ash at different temperature and exposed to aggressive environment. *Advanced Materials Research*, 620, 87–93.

Khanal S (2021). System of Rice Intensification in Nepal: Determinant Factors for Adoption, and Relevance to Climate Change. *M.Sc. thesis*, Norwegian University of Life Sciences, Ås, Norway.

Knoema (2022). Bangladesh - Production of Beef and Buffalo Meat. https://knoema.com/atlas/Bangladesh/topics/Agriculture/Live-Stock-Production-Production-Quantity/Production-of-beef-and-buffalo-meat [accessed 13-06-2024].

Kordi M, Farrokhi N, Pech-Canul MI, Ahmadikhah A (2023). Rice husk at a glance: from agro-industrial to modern applications. *Rice Science*, 31(1), 14–32.

Makebo GM (2019). Partial replacement of cement material in Ethiopia: a review. *International Research Journal of Engineering and Technology*, 6(10), 1002–1005.

Mymrin V, Pedroso DE, Pedroso C, Alekseev K, Avanci MA, Winter E, Cechin L, Rolim PH, Iarozinski A, Catai RE (2017). Environmentally clean composites with hazardous aluminum anodizing sludge, concrete waste, and lime production waste. *Journal of Cleaner Production*, 174, 380–388.

Neville AM, Brooks JJ (1987). Concrete Technology. Longman Scientific and Technical, Harlow, United Kingdom.

Petrounias P, Rogkala A, Giannakopoulou PP, Lampropoulou P, Xanthopoulou V, Koutsovitis P, Koukouzas N, Lagogiannis I, Lykokanellos G, Golfinopoulos A (2021). An innovative experimental petrographic study of concrete produced by animal bones and human hair fibers. *Sustainability*, 13(14), 8107.

Ren D, Yan C, Duan P, Zhang Z, Li L, Yan Z (2016). Durability performances of wollastonite, tremolite and basalt fiber-reinforced metakaolin geopolymer composites under sulfate and chloride attack. *Construction and Building Materials*, 134, 56–66.

Scrivener KL, John VM, Gartner EM (2018). Eco-efficient cements: Potential economically viable solutions for a low-CO_2 cement-based materials industry. *Cement and Concrete Research*, 114, 2–26.

Şengel H, Kınık K, Erol H, Canbaz M (2022). Effect of waste steel tire wired concrete on the mechanical behavior under impact loading. *Challenge Journal of Structural Mechanics*, 8(4), 150–158.

Swaminathen AN, Kumar CV, Ravi SR, Debnath S (2021). Evaluation of strength and durability assessment for the impact of rice husk ash and metakaolin at high performance concrete mixes. *Materials Today Proceedings*, 47, 4584–4591.

Teshome BB (2019). Investigating mechanical properties of animal bone powder partially replaced cement in concrete production. *International Journal of Scientific Research and Engineering Development*, 2(6), 447–490.

Ulusu H, Aruntas HY, Gencel O (2016). Investigation on characteristics of blended cements containing pumice. *Construction and Building Materials*, 118, 11–19.

World Population Review (2024). World Population by Country 2024. https://worldpopulationreview.com [accessed 13-06-2024].

Zerbino R, Giaccio G, Isaia G (2010). Concrete incorporating rice-husk ash without processing. *Construction and Building Materials*, 25(1), 371–378.

Zhao Y, Sun Y, Bu C, Cao X, Jiang Q, Zhu D (2022). Review on Application of rice husk ash based concrete composite and preparation conditions of rice husk ash. *Academic Journal of Architecture and Geotechnical Engineering*, 4(2), 7–11.

Challenge Journal of Structural Mechanics

Research Article

Investigation of the effects of re-curing on mechanical properties of basalt-polypropylene hybrid fiber concretes after exposure to high temperature

Yunus Urtekin [a], Zinnur Çelik [b,*]

[a] *Department of Civil Engineering, Atatürk University, 25240 Erzurum, Türkiye*

[b] *Department of Construction Technology, Pasinler Vocational School, Atatürk University, 25300 Erzurum, Türkiye*

ABSTRACT

Fiber reinforced concretes have attracted significant attention in recent decades due to their superior flexural and toughness properties compared to traditional concrete in civil engineering structures. In addition, cementitious materials can undergo significant mechanical deterioration under high temperature. Therefore, the investigation of the properties of FRC for fire-resistant design has become an important research topic in recent years. On the other hand, there is very little research on the repair of FRCs damaged by fire. In this study, high temperature resistance of mixtures prepared using basalt and polypropylene fibers was investigated. In addition, the ability of FRCs exposed to high temperatures to regain their properties by applying water re-curing process was investigated. In this context, ultrasonic pulse velocity (UPV), compressive and flexural strength of FRC series after different stages were investigated. In the use of water curing single basalt fiber, 18.56% and 13.82% increase in relative compressive strength was obtained after 600 °C and 800 °C, respectively. These increase rates were determined as 22.25% and 22.81% in relative flexural strength. Recovery was more significant in the hybrid mixture formed with 0.2% polypropylene fiber. 29.22% and 15.93% recovery was reported in relative compressive strength after 600 °C and 800 °C, respectively. It was determined that re-curing significantly increased the mechanical properties of FRC mixtures.

ARTICLE INFO

Article history:

Received – October 6, 2024
Revision requested – November 6, 2024
Revision received – November 21, 2024
Accepted – December 2, 2024

Keywords:

Basalt fiber
Polypropylene fiber
Mechanical properties
Water re-curing
High temperature

Citation: Urtekin Y, Çelik Z (2025). Investigation of the effects of re-curing on mechanical properties of basalt-polypropylene hybrid fiber concretes after exposure to high temperature. *Challenge Journal of Structural Mechanics*, 11(1), 14–23.

1. Introduction

Normal concrete provides low tensile and flexural strength, fracture energy and ductility (Kızılkanat et al. 2015; Wang et al. 2019). However, significant improvements occur especially in terms of tensile strength, toughness and durability as a result of reinforcing concrete with fibers. The purpose of incorporating fibers is to enhance the tensile strength of concrete by improving its load-bearing capacity through crack bridging (Şengel et al. 2022). Concrete reinforced with a single type of fiber can only benefit from the improvement of its properties in a limited direction (Ahmed and Maalej 2009). In recent decades, the strengthening and repair of structures using fiber-reinforced polymer composite materials, produced with various fiber types, has gained significant importance (Çelik et al. 2024). However, with the hybrid use of two or more fibers that can show different performances, different properties of each fiber can be utilized (Ahmed and Maalej 2009; Banthia et al. 2014; Qian and Stroeven 2000). In addition, fiber-reinforced concretes (FRC) exhibit more positive behavior in terms of the safety requirements of civil engineering structures exposed to fire compared to normal concrete (Hou et al.

* *Corresponding author*. Tel.: +90-442-661-3982 ; E-mail address: zinnur.celik@atauni.edu.tr (Z. Çelik)
ISSN: 2149-8024 / DOI: https://doi.org/10.20528/cjsmec.2025.01.002

2019; Chinthapalli et al. 2020; Yao et al. 2022). Significant changes in temperature during fire are reported to cause deterioration and spalling of components in the concrete matrix structure, resulting in significant strength reductions (Li et al. 2020).

Polymer fibers are preferred to fill the cement paste and voids in the concrete and to improve strength and durability (Alaskar et al. 2021). Basalt fiber (BF) is a new type of environmentally friendly fiber that has been widely used in recent decades, produced by melting basalt rock (Jiang et al. 2014; Branston et al. 2016). Basalt fibers are manufactured with lower energy consumption compared to commonly used fiber types, such as steel, glass, and carbon (Gultekin 2023). Basalt fiber can improve the physico-mechanical properties of concrete with its high tensile strength and elasticity modulus. In addition to these properties, it is a type of fiber with high melting temperature and chemical corrosion (Yao et al. 2022; Deng et al. 2020; Niaki et al. 2018). Literature studies report that the temperature range of basalt fiber is between −200 °C to 800 °C (Fiore et al. 2015; Guo et al. 2018). On the other hand, polypropylene fiber (PPF) has a restrictive effect on the plastic shrinkage of concrete at an early age (Deng et al. 2021). Additionally, adding polypropylene fiber can strengthen the matrix fiber bond and strengthen crack resistance (Yao et al. 2022).

Fire poses a significant threat to all constructional components, often resulting in the loss of life and property (Koşatepe and Yazici 2023). The residual properties of FRC exposed to elevated temperatures are significantly affected by the materials and fibres (Han et al. 2005; Serrano et al. 2016; Wu et al. 2020). Previous studies have found that the residual properties of FRC exposed to heating will be significantly affected by the type of fibres added to the concrete (Sideris et al. 2009; Choumanidis et al. 2016). Fiber types can be broadly divided into two groups in terms of improving the high temperature resistance of concrete. A group of materials with significant thermal stability during heating, such as steel, basalt and carbon fiber, can limit the formation of microcracks during and after fire by fiber bridging effect (Wu et al. 2020). Fibers such as PPF and PVA, on the other hand, show melting properties at low temperatures in cement composite structures, reducing internal vapor pressure and preventing microstructure deterioration represents the other group that provides pathways for water to evaporate (Wu et al. 2020). Yao et al. (2022) reported that the hybrid use of BF and PPF was significant in improving the mechanical performance of mortar specimens at target temperatures. In the study of Fu et al. (2021), BF compared to PPF reported that the effect on strength was more positive. It was also found that the improvement effect on ductility was more effective in the use of hybrid BF/PPF compared to those using only PPF or BF.

Studies conducted in recent decades have reported that concrete that has deteriorated after high temperatures can regain its strength and durability properties by re-curing with water or exposing it to a humid environment (He et al. 2022; Bouhafs et al. 2024; Poon et al. 2001; Li 2021). Crook and Murray (1970) first reported the post-fire re-curing process in 1970. In this study, they found that re-curing had a significant effect on the recovery of the compressive strength of concrete. After the high temperature curing process, the chemical deteriorations that occur during heating are reversed and the dehydrated matrix is rehydrated by re-curing with water (Wu et al. 2020; Shui et al. 2008). In this context, past studies have focused on the effect of substitute materials on re-curing (Poon et al. 2001; Poon and Azhar 2003; Li 2021; Kharrazi et al. 2023). However, studies on the re-curing of FRC with water are limited and mostly focused on steel fiber. Bouhafs et al. (2024) investigated the effect of water re-curing on concrete mixtures containing steel fibers exposed to high temperatures. He et al. (2023) reported significant improvements in compressive strength of hybrid fiber concrete containing steel and PPF after water re-curing after heating.

As a result of the examination of literature studies, it was observed that there is limited study on the high temperature resistance of concretes reinforced with BF and PPF. In addition, in recent years, the performance research of FRC, especially exposed to fire, after water re-curing has gained importance. However, there is no study in the literature discussing the effect of water re-curing on concretes containing BF and PPF after heating. In this context, both the high temperature resistance of concretes with BF and PPF added, used individually or as hybrids, and their performance after water re-curing process were investigated in this study. Three different temperatures (400 °C, 600 °C and 800 °C) were targeted in the study and subjected to re-curing after heating. After the specified stages UPV, compressive and flexural strengths were determined.

2. Materials and Method

2.1. Materials

CEM I 42.5 R ordinary Portland cement (OPC) was used to prepare the mixture specimens. Chemical compositions and physical characteristics of OPC are presented in Table 1. In the study, 0-5 mm river sand was used as fine aggregate. Crushed stone aggregate in the size range of 5-15 mm was used as coarse aggregate. The specific gravity of fine and coarse aggregate was determined as 2.64 and 2.60, and the water absorption values were determined as 1.10 and 0.92, respectively.

To improve the workability of concrete mixtures, the third-generation polycarboxylic ether-based, highly water-reducing BASF Master Glenium 123 superplasticizer with a density of 1.13 g/cm^3 and a pH of 5.5 ± 1 was used. In addition, two types of fibers produced from different geometries and materials were used in the study. The properties and images of the fibers are presented in Table 2 and Fig. 1.

2.2. Mix design, curing and experimental program

In order to investigate the effect of two different fibers on the performance of FRC before and after heating and after re-curing with water, 3 different mixtures were designed in the study. In all mixtures, the cement amount

was fixed as 450 kg/m^3 and the water/cement ratio was fixed as 0.42. In the first mixture (M1), 0.40% basalt fiber was used alone. In the second (M2) and third mixtures (M3), basalt fiber was replaced with 0.10% and 0.20% polypropylene fiber and designed as a hybrid. Basalt fiber was preferred in the study because it has a high melting point and is cheaper than steel fiber and has better chemical resistance compared to glass fiber. In addition, it was adopted to investigate the effect of PPF on re-curing due to its low melting temperature. The material ratios of these three mixtures are given in Table 3. As a result of experiments, a slump diameter of 110–125 mm was reached. This slump range belonged to class S3 according to EN 206 (2016).

Table 1. Chemical compositions and physical properties of cement.

Chemical compositions	SiO_2	Al_2O_3	Fe_2O_3	CaO	MgO	K_2O	SO_3	LOI (%)
	17.73	4.56	3.07	62.80	2.07	0.62	2.90	2.05

Physical properties	Specific gravity	Insoluble residue (%)	Fineness (cm^2/g)
	3.15	0.66	3450

Table 2. Properties of fiber.

Type	Length (mm)	Diameter (μm)	Density (g/cm^3)	Tensile strength (MPa)	Modulus of elasticity (GPa)
Basalt	24	9–23	2.60–2.80	4840	89
Polypropylene	12	18–20	0.91	350	3.50

Fig. 1. View of fibers: (a) Basalt fibers; (b) Polypropylene fibers.

Table 3. Mixture proportions and slump values.

Mixture code	Cement (kg/m^3)	W/C	Fine agg. (kg/m^3)	Coarse agg. (kg/m^3)	Super plasticizer (kg/m^3)	BF (%)	PPF (%)	Slump (mm)
BF0.40 (M1)	450	0.42	934	754	10.50	0.40	–	125
BF0.30PPF0.10 (M2)	450	0.42	934	754	10.50	0.30	0.10	120
BF0.20PPF0.20 (M3)	450	0.42	934	754	10.50	0.20	0.20	110

The cured specimens were kept in the oven at 40 °C until the mass values stabilized. Specimens removed from the oven were exposed to the target temperature of 400, 600 and 800 °C with a constant heating rate of 5 °C/min. At each target temperature, the oven was fixed for 1 hour and then allowed to cool. After cooling, half of the specimens were tested, while the other half was placed in water for re-curing for 30 days.

All concrete series were subjected to non-destructive testing (UPV) according to ASTM C597-02 (2016). UPV test was performed on cube specimens with dimensions of 100x100x100 mm^3 using the Pundit Lab device with a nominal frequency of 54 kHz. The compressive strength of the specimens subjected to different conditions was determined according to the EN 12390-3 (2009) standard on cube specimens of 100x100x100 mm^3 dimensions.

70x70x280 mm^3 prism specimens prepared from each series were subjected to flexural tests according to EN 12390-5 (2009). For UPV, compressive, and flexural tests, the average of 3 specimens was taken for each different stage.

3. Results and Discussion

3.1. Ultrasonic pulse velocity results of FRC

The ultrasonic pulse velocity (UPV) test results of all FRC mixture series are given in Table 4. Before exposure to high temperature, the UPV values of the specimens were measured as 4.48 to 4.55 km/s. The highest UPV value was obtained from the BF0.40 series. Decreases in UPV values were observed with the addition of PPF to the mixtures. A slightly decrease of 1.54% was detected in the UPV value as a result of replacing 0.20% PPF with BF. This situation can be attributed to the fact that the addition of PPF to the mixtures reduces the workability and consequently increases the voids. Nik and Omran (2013) reported that steel and glass fiber had no effect on the UPV value, but the use of PPF reduced the UPV value. Özkan and Çoban (2021) reported the UPV results of mixtures using PPF and BF fibers in their research. They reported that there was an approximately 2% improvement in the UPV value by replacing the PPF fiber with BF at a rate of 25%.

Table 4. Ultrasonic pulse velocity (UPV) test results of FRC.

Mixtures	20 °C	400 °C	600 °C	800 °C
BF0.40 (M1)	4.55	4.02	2.72	1.13
BF0.40-R (M1-R)		4.17	3.88	2.42
BF0.30PPF0.10 (M2)	4.53	3.92	2.67	1.12
BF0.30PPF0.10-R (M2-R)		4.12	3.93	2.46
BF0.20PPF0.20 (M3)	4.48	3.78	2.54	1.08
BF0.20PPF0.20-R (M3-R)		4.13	3.99	2.48

The effect of high temperature and subsequent water re-curing on the relative residual UPV values of the specimens is given in Fig. 2. As the high temperature value to which FRC mixtures were exposed increased, their UPV decreased. The UPV value of the specimens exposed to 400 °C was measured between 4.02 and 3.78 km/s. The lowest UPV value at 400 °C occurred in the mixture using 0.20% PPF (M3). The relative UPV value of the M3 series at 400 °C is 84.38%. This situation can be attributed to the increased pores and cracks in the concrete due to the melting of PPF fibers at high temperatures (Boğa et al. 2022). As the temperature increased to 600 °C, the relative UPV values of FRCs were in the range of 56.70% to 59.78%. Significant decreases were detected in UPV results as the temperature increased to 800 °C. A decrease of 75.16% to 75.89% was obtained in the UPV value of all FRC series.

Relative UPV values of the mixture series were remarkably improved after water re-curing. This can be attributed to the fact that the new products formed as a result of water re-curing repair cracks and refine pores in thermally damaged concrete, which will also improve the mechanical properties (Bouhafs et al. 2024). The relative ultrasonic pulse rate of M1 series increased from 88.35% to 91.65% at 400 °C, showing a recovery rate of approximately 3.30%. The recovery rate of M2 mixture using 0.10% PPF was determined as 4.42%. The maximum recovery rate was % It was obtained from the M3 series, which increased from 84.38 to 92.19%, providing 7.81% improvement. This can be attributed to the filling of cracks and voids caused by the melting and evaporation of PPFs with rehydrated products (He et al. 2023).

It was determined that at 600 °C and beyond, water re-curing showed more significant recovery than 400 °C. Re-curing after 600 °C increased the relative UPV of M1 series from 59.78% to 85.27%. The recovery rate of M1 series was % It was determined as 25.49. This ratio was calculated as 27.81% and 32.36% in M2 and M3 mixtures, respectively. At 800 °C, the relative UPV values of the mixtures approached each other. The recovery rates in M1, M2 and M3 mixtures were 28.35%, 30.64% and 31.25%, respectively. It was observed that re-curing had more significant effects at temperatures above 400 °C. This can be attributed to the presence of more dewatered products in the concrete with increasing temperature and the rehydration and carbonation products of these products formed with the absorbed water (Bouhafs et al. 2024).

Table 5. Compressive strength test results of FRC.

Mixtures	20 °C	400 °C	600 °C	800 °C
BF0.40	52.05	43.55	23.82	10.89
BF0.40-R		44.37	33.48	18.08
BF0.30PPF0.10	51.36	40.06	21.82	9.32
BF0.30PPF0.10-R		44.42	33.62	16.58
BF0.20PPF0.20	49.28	37.82	20.42	9.17
BF0.20PPF0.20-R		44.51	34.82	17.02

3.2. Compressive strength

Compressive strength results obtained at different stages of FRC mixtures are given in Table 5. The highest compressive strength value at room temperature was obtained from M1 (BF0.40) series with 52.05 MPa. In M2 series with 0.10% PPF added, 51.36 MPa strength was obtained, and in the mixture with 0.20% PPF, 49.28 MPa strength was obtained. This situation can be attributed to the fact that PPF has a larger diameter compared to BF and increases pores due to its air-entraining effect. As a result, it indicates that BF has a higher bond with the matrix than PPF, albeit slightly (Wang et al. 2019).

Fig. 3 shows the relative strength results of the series after high temperature and water re-curing. Decreases in compressive strength were observed with the increase in temperature. At 400 °C, a 16.33% decrease in the compressive strength of the M1 series was detected. This rate decreased more in the M2 and M3 mixtures, being

22% and 23.25%, respectively. The decreases in strength became more significant as the temperature increased to 600 °C and above. The compressive strength of the series subjected to 600 °C was between 20.42 and 23.82 MPa. These values were between 41.44% and 45.76% of the strength values at ambient temperature. In the M1 series, the compressive strength decreased by approximately 79%, reaching 10.89 MPa at 800 °C. These data obtained after high temperature were a case of internal vapor pressure and thermal effect causing the formation and expansion of cracks in the Interface Transition Zone (ITZ) and matrix (He et al. 2023, Chen and Liu 2004). After high temperature, the strength values of hybrid mixtures with BF and PPF additions were lower compared to the series using only BF. This result can be attributed that PPFs start to melt at about 170 °C and lose their bridging effect by forming pores (Boğa et al. 2022). On the contrary, BF is more resistant to higher temperatures.

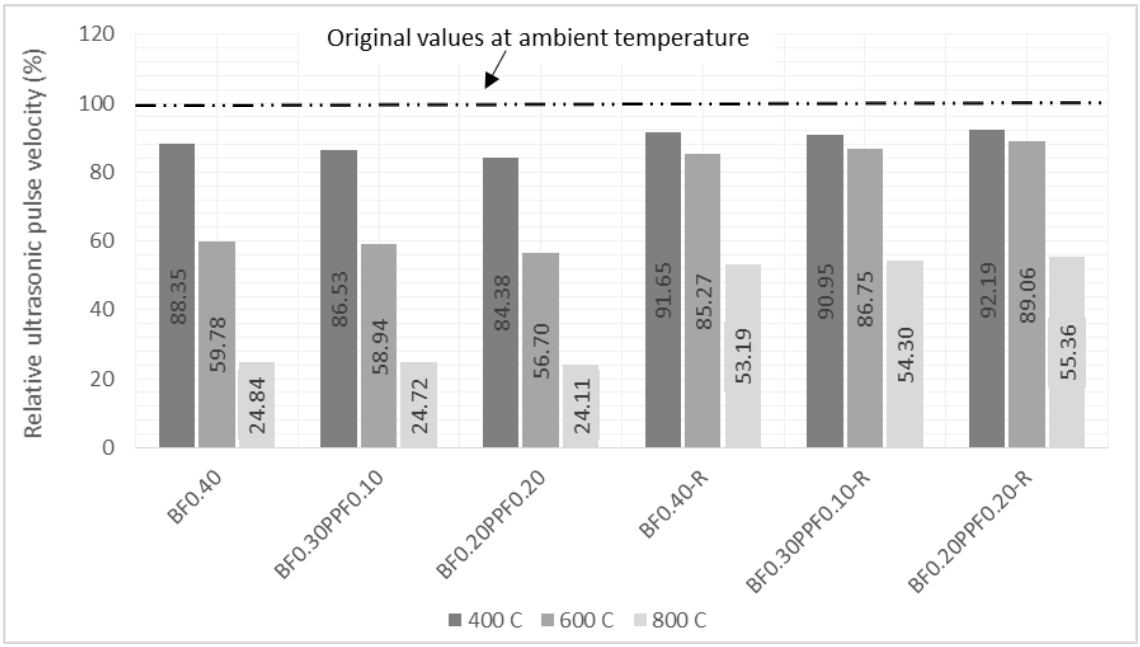

Fig. 2. Relative residual UPV values after high temperature and re-curing.

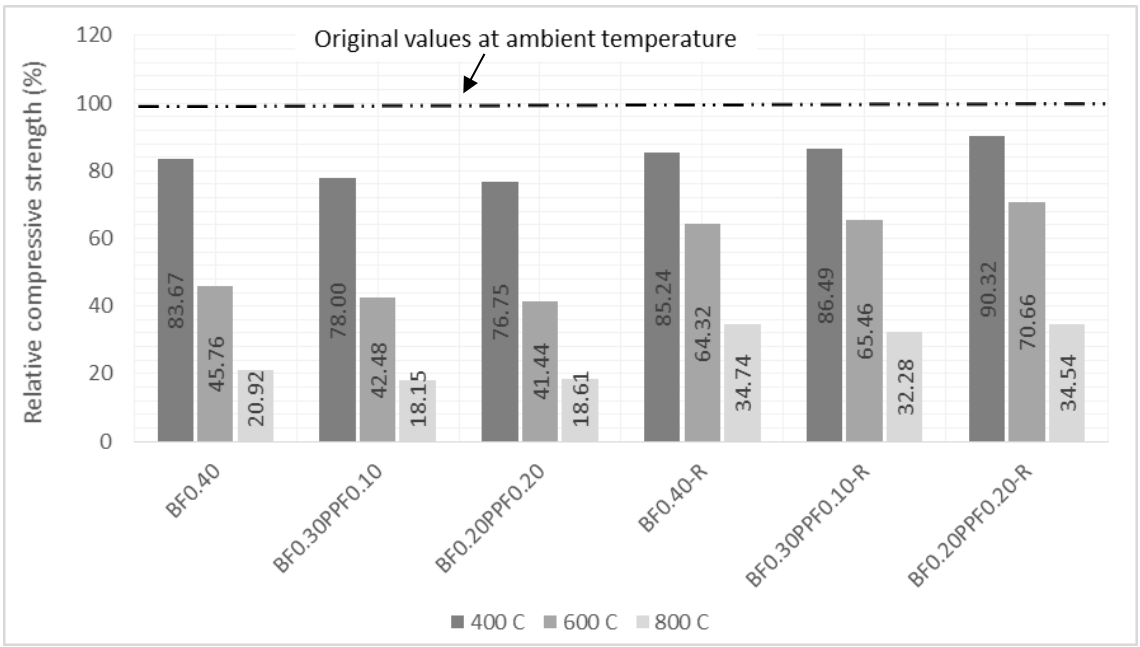

Fig. 3. Relative residual compressive strength values.

Remarkably recovery gain was obtained in compressive strength of thermally damaged basalt-polypropylene hybrid fiber reinforced specimens after water re-curing. M1 (BF0. for series 40), the relative compressive strength at 400 °C increased from 83.67% to 85.27% after water re-curing. This shows that the bonding between the basalt fiber and the matrix was not significantly damaged. With the increase of the temperature to

600 °C, the recovery is seen in series M1. The recovery rate was determined as 18.56%. The recovery rate of the M1 mixture at 800 °C was determined as 13.82%. The increase in recovery rates at 600 °C and above can be attributed to the narrowing of cracks formed by more intensive rehydration products (He et al. 2023). In addition, the increase in strength of FRCs after re-curing with water can be attributed to the improvement of the bond strength between the fiber and matrix together with the newly formed rehydration products.

With the addition of PPF to the blend series, a remarkably increase in the strength recovery rate occurred. The strength recovery rate of the M2 (BF0.30PPF0.10) series at 400 °C and 600 °C was determined as 8.49% and 22.98%, respectively. The recovery rate continued to increase with PPF content. In the M3 series, where BF was replaced by 0.20% PPF, the recovery rate at 400 °C was 13.57%. This rate continued to increase with increasing temperature, calculated as 29.22% and 15.93% at 600 and 800 °C, respectively. The higher recovery rate in mixtures using PPF is due to the filling of the gaps formed by the evaporation of PPF fibers with rehydrated products. He et al. (2023) investigated the effect of re-curing after high temperature on concrete specimens produced using single steel fiber and steel-polypropylene hybrid fiber. They reported that PPF was more effective than steel fiber in terms of recovery rate after re-curing.

The relationship between temperature and relative compressive strength was obtained in the range of 400 °C to 800 °C as shown in Fig. 4.

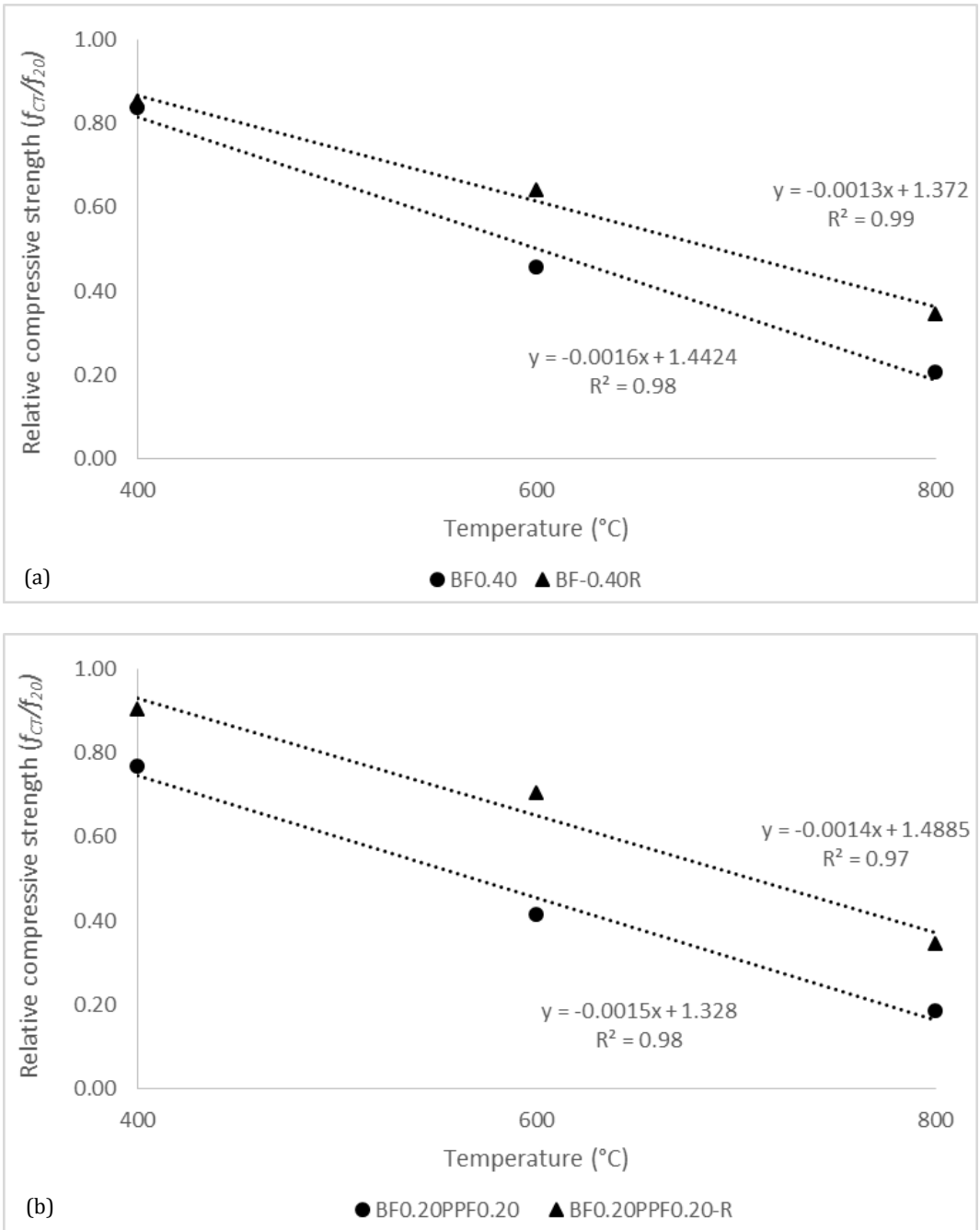

Fig. 4. Relationship between temperature and relative compressive strength: (a) BF0.40; (b) BF0.20PPF0.20.

The fitting functions between the temperature and the relative compressive strength experimental results obtained at different stages are given in Eqs. (1)–(4).

- Mix. BF0.40

After heating:

$$\frac{f_{CT}}{f_{20}} = \left|1.442 - 1.60\left(\frac{T}{1000}\right)\right| \quad 400 \le T \le 800 \quad R^2 = 0.98 \quad (1)$$

After re-curing:

$$\frac{f_{CT}}{f_{20}} = \left|1.372 - 1.30\left(\frac{T}{1000}\right)\right| \quad 400 \le T \le 800 \quad R^2 = 0.99 \quad (2)$$

- Mix. BF0.20PPF0.20

After heating:

$$\frac{f_{CT}}{f_{20}} = \left|1.328 - 1.50\left(\frac{T}{1000}\right)\right| \quad 400 \le T \le 800 \quad R^2 = 0.98 \quad (3)$$

After re-curing:

$$\frac{f_{CT}}{f_{20}} = \left|1.488 - 1.40\left(\frac{T}{1000}\right)\right| \quad 400 \le T \le 800 \quad R^2 = 0.97 \quad (4)$$

3.3. Flexural strength

The flexural strength results of the FRC specimens before and after heating and after water re-curing are given in Table 6. The flexural strength at ambient temperature is between 7.12 and 7.25 MPa. The highest flexural strength at room temperature was obtained in the M2 mixture with 0.10% PPF. Wang et al. (2019) reported that with the addition of PPF to 0.20% BF content, the flexural strength decreased compared to the single BF.

The relative flexural strengths of FRC specimens after high temperature and re-curing are given in Fig. 5. Significant decreases in flexural strength were observed with the increase in temperature. After heating to 400 °C, the relative flexural strength of the M1 mixture was determined as 62.31%, while this ratio was determined as 58.48% in the M2 mixture. The decrease in relative strength continued with the increase in PPF content and was reported as 54.21%. This decrease can be attributed to the melting and evaporation of PPFs at approximately 170 °C. As the heating temperature increased to 600 °C, the flexural strength of M1 series decreased by approximately 62%. This decrease was calculated as approximately 66% and 68% in M2 and M3 series, respectively. The relative flexural strengths of the mixtures after 800 °C were between 18.54% and 21.97%. The high relative strength of the mixture using single BF at all temperatures is an indication that BFs still effectively restrict cracks due to their high melting temperature.

Table 6. Flexural strength test results of FRC.

Mixtures	20 °C	400 °C	600 °C	800 °C
BF0.40	7.19	4.48	2.72	1.58
BF0.40-R		5.06	4.32	3.22
BF0.30PPF0.10	7.25	4.24	2.49	1.42
BF0.30PPF0.10-R		4.88	4.42	3.12
BF0.20PPF0.20	7.12	3.86	2.32	1.32
BF0.20PPF0.20-R		4.62	4.1	2.98

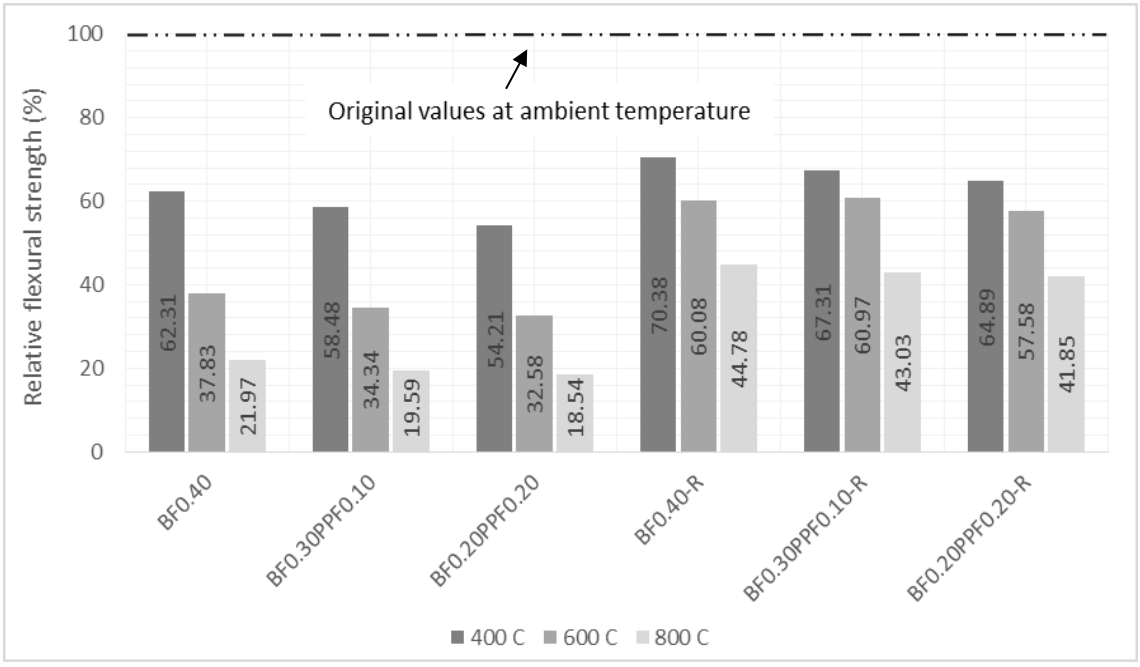

Fig. 5. Relative residual flexural strength values.

After heating, re-curing with water had a significant effect on the flexural strength. Re-curing after 400 °C increased the relative strength of M1 mixture from 62.31% to 70.38%. The flexural strength improvement rate was reported as 8.83% and 10.68% in M2 and M3 mixtures, respectively. The recovery rate after 600 °C was determined as 22.25% in the BF sample. This strength recovery rate was higher in the mixtures with PPF added. The recovery rate was reported as 26.63% in the mixture with 0.10% PPF and 25% in the mixture with 0.20%. As the temperature increased to 800 °C, the recovery rates approached each other. The relative flexural strength rates of the M1, M2 and M3 mixtures increased from 21.97 to 44.78, from 19.59 to 43.03 and from 18.54 to 41.85, respectively.

The relationship between temperature and relative flexural strength was obtained in the range of 400 °C to 800 °C as shown in Fig. 6.

The fitting functions between the temperature and the relative flexural strength experimental results obtained at different stages are given in Eqs. (5)–(8).

- Mix. BF0.40

After heating:

$$\frac{f_{FT}}{f_{20}} = \left|1.012 - \left(\frac{T}{1000}\right)\right| \quad 400 \leq T \leq 800 \quad R^2 = 0.98 \qquad (5)$$

After re-curing:

$$\frac{f_{CT}}{f_{20}} = \left|0.968 - 0.60\left(\frac{T}{1000}\right)\right| \quad 400 \leq T \leq 800 \quad R^2 = 0.98 \qquad (6)$$

- Mix. BF0.20PPF0.20

After heating:

$$\frac{f_{CT}}{f_{20}} = \left|0.886 - 0.90\left(\frac{T}{1000}\right)\right| \quad 400 \leq T \leq 800 \quad R^2 = 0.98 \qquad (7)$$

After re-curing:

$$\frac{f_{CT}}{f_{20}} = \left|0.893 - 0.60\left(\frac{T}{1000}\right)\right| \quad 400 \leq T \leq 800 \quad R^2 = 0.95 \qquad (8)$$

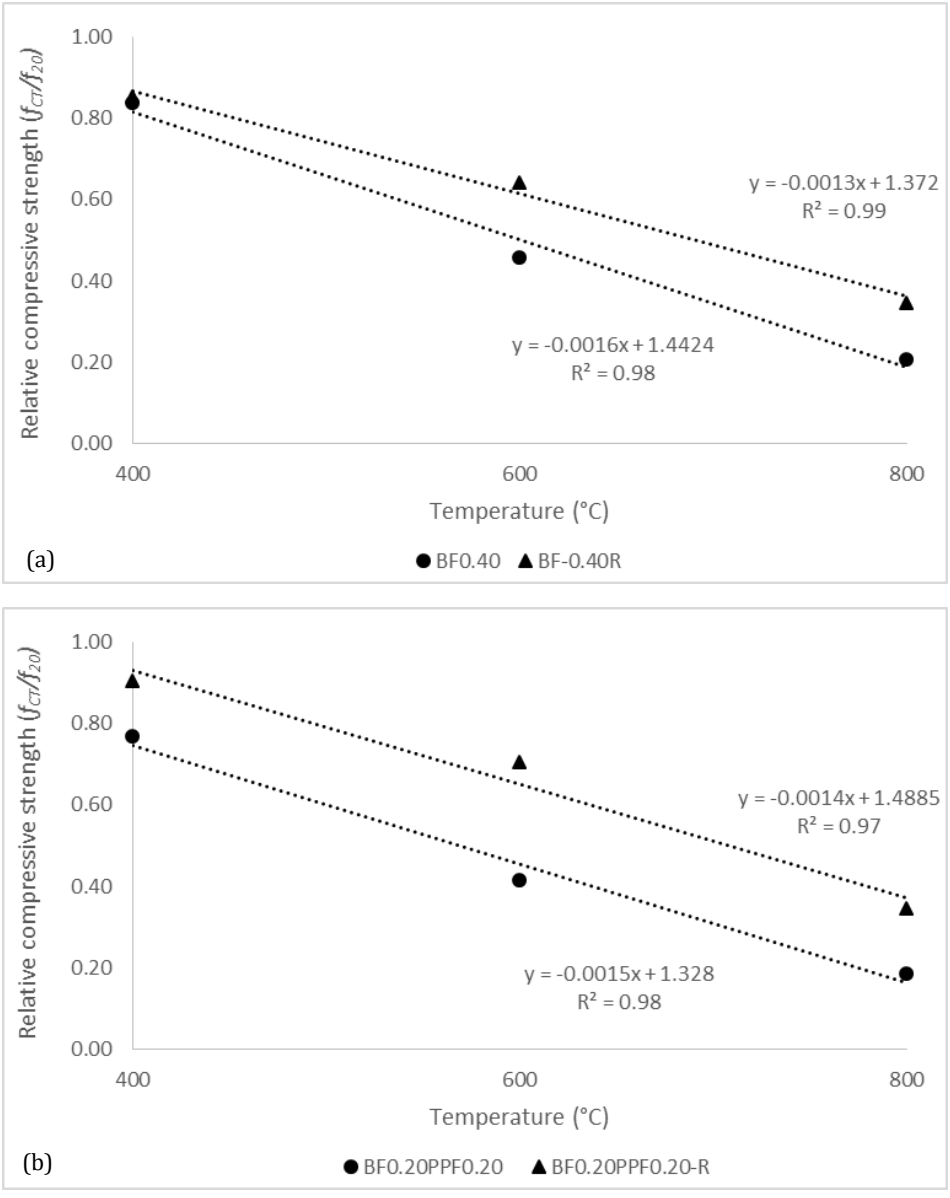

Fig. 6. Relationship between temperature and relative flexural strength: (a) BF0.40; (b) BF0.20PPF0.20.

4. Conclusions

- The UPV values of the specimens not exposed to heating were measured as 4.48 to 4.55 km/s. A slight decrease of 1.54% was detected in the UPV value as a result of replacing 0.20% PPF with BF. Significant decreases were observed in the UPV values of the specimens with the increase in temperature.
- The compressive strength of the series before heating was determined as 49.28 and 52.05 MPa. The decrease in strength was detected with exposure to high temperatures. The compressive strength of the series subjected to 600 °C was between 20.42 and 23.82 MPa. These values were between 41.44% and 45.76% of the strength values at ambient temperature.
- It was found that water re-curing had a significant effect on mechanical properties. This situation was more evident especially in mixtures containing polypropylene fibers. In the series where BF was replaced by 0.20% PPF, the relative compressive strength recovery rate at 400 °C was 13.57%. This rate continued to increase with increasing temperature, calculated as 29.22% and 15.93% at 600 and 800 °C, respectively.
- Similar to the improvements in compressive strength, significant recoveries occurred in flexural strength. The relative recovery rate in flexural strength was reported as 26.63% in the mixture with 0.10% PPF and 25% in the mixture with 0.20% PPF.
- Post-fire water re-curing is a useful method for partial recovery of the mechanical and durability properties of thermally damaged concrete. Especially civil engineering structures damaged by fire can be maintained by this method rather than demolished and become usable.
- In future studies, it is recommended to use different fibers and ratios and to work at intermediate temperature values. In addition, the bond strength between the matrix and fiber is important along with the effect of rehydration in the concrete after re-curing and this issue should be examined in detail. It is also thought that using fibers and substituting different pozzolanic materials instead of cement may have different effects.

Acknowledgements

None declared.

Funding

This research was supported by Scientific Research Projects Program (BAP), Atatürk University under grant number FYL-2024-13225.

Conflict of Interest

The authors declared no potential conflicts of interest with respect to the research, authorship, and/or publication of this manuscript.

Author Contributions

All of the authors made substantial contributions to conception and design, or acquisition of data, or analysis and interpretation of data; were involved in drafting the manuscript or revising it critically for important intellectual content; and gave final approval of the version to be published.

Data Availability

The datasets created and/or analyzed during the current study are not publicly available, but are available from the corresponding author upon reasonable request.

REFERENCES

Ahmed SFU, Maalej M (2009). Tensile strain hardening behaviour of hybrid steel-polyethylene fibre reinforced cementitious composites. *Construction and Building Materials*, 23(1), 96-106.

Alaskar A, Albidah A, Alqarni AS, Alyousef R, Mohammadhosseini H (2021). Performance evaluation of high-strength concrete reinforced with basalt fibers exposed to elevated temperatures. *Journal of Building Engineering*, 35, 102108

ASTM C597 (2016). Standard test method for pulse velocity through concrete. ASTM International, West Conshohocken, PA.

Banthia N, Majdzadeh F, Wu J, Bindiganavile V (2014). Fiber synergy in hybrid fiber reinforced concrete (HyFRC) in flexure and direct shear. *Cement and Concrete Composites*, 48, 91-97.

Boğa AR, Karakurt C, Şenol AF (2022). The effect of elevated temperature on the properties of SCC's produced with different types of fibers. *Construction and Building Materials*, 340, 127803.

Bouhafs F, Ezziane M, Ayed K, Leklou N, Mouli M (2024). Effect of water re-curing on the physico-mechanical and microstructural properties of self-compacting concrete reinforced with steel fibers after exposure to high temperatures. *Construction and Building Materials*, 413, 134805.

Branston J, Das S, Kenno SY, Taylor C (2016). Mechanical behaviour of basalt fibre reinforced concrete. *Construction and Building Materials*, 124, 878-886.

Chen B, Liu J (2004). Residual strength of hybrid-fiber-reinforced high-strength concrete after exposure to high temperatures. *Cement and Concrete Research*, 34(6), 1065-1069.

Chinthapalli HK, Chellapandian M, Agarwal A, Prakash SS (2020). Effectiveness of hybrid fibre-reinforced polymer retrofitting on behaviour of fire damaged RC columns under axial compression. *Engineering Structures*, 211, 110458.

Choumanidis D, Badogiannis E, Nomikos P, Sofianos A (2016). The effect of different fibres on the flexural behaviour of concrete exposed to normal and elevated temperatures. *Construction and Building Materials*, 129, 266-277.

Crook DN, Murray MJ (1970). Regain of strength after firing of concrete. *Magazine of Concrete Research*, 22(72), 149-154.

Çelik Z, Turan E, Oltulu M, Öner G (2024). Reinforcement of concrete beams using waste carbon-nanoclay-fiberglass laminate pieces. *Challenge Journal of Concrete Research Letters*, 15(1), 1-6.

Deng F, Xu L, Chi Y, Wu F, Chen Q (2020). Effect of steel-polypropylene hybrid fiber and coarse aggregate inclusion on the stress–strain behavior of ultra-high performance concrete under uniaxial compression. *Composite Structures*, 252, 112685.

Deng Z, Liu X, Yang X, Liang N, Yan R, Chen P, Xu Y (2021). A study of tensile and compressive properties of hybrid basalt-polypropylene fiber-reinforced concrete under uniaxial loads. *Structural Concrete*, 22(1), 396-409.

EN 206 (2016). Cement - Part 1: Concrete. Specification, performance, production and conformity. European Committee for Standardization, Brussels, Belgium.

EN 12390-3. (2009). C Testing hardened concrete—Part 3: Compressive strength of test specimens. European Committee for Standardization, Brussels, Belgium.

EN 12390–5: (2009) Testing hardened concrete — Part 5: Flexural strength of test specimens. European Committee for Standardization, Brussels, Belgium.

Fiore V, Scalici T, Di Bella G, Valenza A (2015). A review on basalt fibre and its composites. *Composites Part B: Engineering*, 74, 74-94.

Fu Q, Bu M, Su L, Liu L, Chen L, Li N, Niu D (2021). Triaxial mechanical behaviour of hybrid basalt–polypropylene fibre-reinforced concrete: the effect of micro-fibres at multi scale levels. *Materials and Structures*, 54(3), 126.

Gultekin A (2023). Effect of hemp and basalt fiber on fracture energy of cement-based composites: a comparative study. *Challenge Journal of Concrete Research Letters*, 14(4), 107-117.

Guo Z, Wan C, Xu M, Chen J (2018). Review of basalt fiber-reinforced concrete in China: Alkali resistance of fibers and static mechanical properties of composites. *Advances in Materials Science and Engineering*, 2018(1), 9198656.

Han CG, Hwang YS, Yang SH, Gowripalan N (2005). Performance of spalling resistance of high performance concrete with polypropylene fiber contents and lateral confinement. *Cement and Concrete Research*, 35(9), 1747-1753.

He F, Biolzi L, Carvelli V (2022). Effects of elevated temperature and water re-curing on fracture process of hybrid fiber reinforced concretes. *Engineering Fracture Mechanics*, 276, 108885.

He F, Biolzi L, Carvelli V (2023). Effects of elevated temperature and water re-curing on the compression behavior of hybrid fiber reinforced concrete. *Journal of Building Engineering*, 67, 106034.

Hou X, Ren P, Rong Q, Zheng W, Zhan Y (2019). Effect of fire insulation on fire resistance of hybrid-fiber reinforced reactive powder concrete beams. *Composite Structures*, 209, 219-232.

Jiang C, Fan K, Wu F, Chen D (2014). Experimental study on the mechanical properties and microstructure of chopped basalt fibre reinforced concrete. *Materials & Design*, 58, 187-193.

Kharrazi H, Ahmadi B, Shekarchi M, Farhoudi N (2023). A comprehensive study of the effects of re-curing on macro- and microstructure of zeolite incorporating concretes after exposure to high temperature. *Materials and Structures*, 56(3), 50.

Kızılkanat AB, Kabay N, Akyüncü V, Chowdhury S, Akça AH (2015). Mechanical properties and fracture behavior of basalt and glass fiber reinforced concrete: An experimental study. *Construction and Building Materials*, 100, 218-224.

Koşatepe A, Yazici C (2023). Investigation of mechanical properties of steel reinforcements in reinforced concrete structures as a result of exposure to fire. *Challenge Journal of Structural Mechanics*, 9(2), 68-76.

Li D, Niu D, Fu Q, Luo D (2020). Fractal characteristics of pore structure of hybrid Basalt–Polypropylene fibre-reinforced concrete. *Cement and Concrete Composites*, 109, 103555.

Li Y (2021). Effect of post-fire curing and silica fume on permeability of ultra-high performance concrete. *Construction and Building Materials*, 290, 123175.

Niaki MH, Fereidoon A, Ahangari MG (2018). Experimental study on the mechanical and thermal properties of basalt fiber and nanoclay reinforced polymer concrete. *Composite Structures*, 191, 231-238.

Nik AS, Omran OL (2013). Estimation of compressive strength of self-compacted concrete with fibers consisting nano-SiO_2 using ultrasonic pulse velocity. *Construction and Building Materials*, 44, 654-662.

Özkan Ş, Çoban Ö (2021). The hybrid effects of basalt and PVA fiber on properties of a cementitious composite: Physical properties and non-destructive tests. *Construction and Building Materials*, 312, 125292.

Poon CS, Azhar S, Anson M, Wong YL (2001). Strength and durability recovery of fire-damaged concrete after post-fire-curing. *Cement and Concrete Research*, 31(9), 1307-1318.

Poon CS, Azhar S (2003). Deterioration and recovery of metakaolin blended concrete subjected to high temperature. *Fire Technology*, 39, 35-45.

Qian CX, Stroeven P (2000). Development of hybrid polypropylene-steel fibre-reinforced concrete. *Cement and Concrete Research*, 30(1), 63-69.

Serrano R, Cobo A, Prieto MI, de las Nieves González M (2016). Analysis of fire resistance of concrete with polypropylene or steel fibers. *Construction and Building Materials*, 122, 302-309.

Shui Z, Xuan D, Wan H, Cao B (2008). Rehydration reactivity of recycled mortar from concrete waste experienced to thermal treatment. *Construction and Building Materials*, 22(8), 1723-1729.

Sideris KK, Manita P, Chaniotakis E (2009). Performance of thermally damaged fibre reinforced concretes. *Construction and Building Materials*, 23(3), 1232-1239.

Şengel H, Kınık K, Erol H, Canbaz M (2022). Effect of waste steel tire wired concrete on the mechanical behavior under impact loading. *Challenge Journal of Structural Mechanics*, 8(4), 150-158.

Wang D, Ju Y, Shen H, Xu L (2019). Mechanical properties of high performance concrete reinforced with basalt fiber and polypropylene fiber. *Construction and Building Materials*, 197, 464-473.

Wu H, Lin X, Zhou A (2020). A review of mechanical properties of fibre reinforced concrete at elevated temperatures. *Cement and Concrete Research*, 135, 106117.

Yao Y, Wang B, Zhuge Y, Huang Z (2022). Properties of hybrid basalt-polypropylene fiber reinforced mortar at different temperatures. *Construction and Building Materials*, 346, 128433.

Challenge Journal of Structural Mechanics

Research Article

Predicting shear strength in reinforced concrete deep beams through finite element modeling of diverse concrete materials

Erkan Polat [a,*], Gökhan Karaman [a]

[a] *Department of Civil Engineering, Munzur University, 62000 Tunceli, Türkiye*

ABSTRACT

This study investigates the prediction of the strength of reinforced concrete deep beams, critical components in urban infrastructure, by evaluating their load-carrying capacities through finite element modeling and nonlinear inelastic analyses using LS-DYNA software. Four widely used concrete material models were examined: Mat084/085, Mat159, Mat072R3, and Mat016. Analyses were conducted on two single-span and four double-span beams with varying reinforcement configurations and an aspect ratio of 1.0, based on well-documented experimental setups. Comparative analyses of force-displacement behavior and stress distributions revealed significant differences in shear strength predictions across the models, with Mat159 providing the most accurate results. These findings establish a reliable and cost-effective approach for predicting the capacities of deep beams, reducing reliance on extensive experimental testing. The study contributes valuable insights for improving strength predictions in critical infrastructure applications such as bridges and foundations.

ARTICLE INFO

Article history:
Received – October 12, 2024
Revision requested – November 19, 2024
Revision received – December 5, 2024
Accepted – December 16, 2024

Keywords:
Deep beams
Shear strength
Finite element modeling
LS-DYNA
Concrete material models

Citation: Polat E, Karaman G (2025). Predicting shear strength in reinforced concrete deep beams through finite element modeling of diverse concrete materials. *Challenge Journal of Structural Mechanics*, 11(1), 24–41.

1. Introduction

In an era of rapidly urbanizing cities, resilient structural elements like deep beams play an essential role in safeguarding critical infrastructure. Deep beams, with their unique load transfer mechanisms predominantly via shear, are vital components in the construction of resilient foundations, bridges, and high-rise buildings. Their ability to withstand significant stresses and distribute loads efficiently makes them indispensable in designing infrastructure capable of withstanding urban challenges, including seismic events, extreme weather, and increasing building loads driven by urban densification. Understanding the behavior and capacity of deep beams under various stress conditions is crucial to improving their design for urban resilience.

Deep beam design and analysis can be complex due to non-linear stress distributions and the potential for large shear forces, requiring specialized approaches like the strut-and-tie method for accurate assessment. Guidelines for various models and theories (e.g., truss model approaches, compression field theories, strut-and-tie models, etc.) for designing reinforced concrete deep beams to resist shear forces are included in ACI 318-19 (2019) and ASCE-ACI Committee 445 on Shear and Torsion (1998).

According to ACI 318-19 (2019), deep beams are defined as elements loaded on one face and supported on the opposite face, where compression and similar compressive elements may develop between loads and supports. Deep beams must be designed considering the nonlinear distribution of longitudinal strain over the

* *Corresponding author*. Tel.: +90-428-213-1794 ; E-mail address: erkanpolat@munzur.edu.tr (E. Polat)
ISSN: 2149-8024 / DOI: https://doi.org/10.20528/cjsmec.2025.01.003

depth of the beam. The net span-to-depth ratio ($2a/h$) of deep beams should not exceed 4, or in the case of a concentrated load, the ratio of the load's distance from the support (a) to the depth (h) should be less than or equal to 2. For the shear reinforcement, A_v should be greater than or equal to, $0.0025b_w s$ (where b_w represents the web width of the beam, and s denotes the spacing of the distributed transverse reinforcement). For the longitudinal reinforcement, A_{vh} should be greater than or equal to $0.0025b_w s_2$ (where s_2 is the spacing of the distributed longitudinal reinforcement). According to the CSA A23.3 (2004), beams with a net span-to-depth ratio of less than 2 are defined as deep beams. Deep beams are designed considering nonlinear stress distributions, lateral torsional buckling, and increasing stresses at the nodes of reinforcements. The use of the Strut-and-Tie Model (STM) method is indicated as necessary for the design of deep beams.

In the literature, there are many analytical and numerical studies aimed at predicting the load-carrying capacities of deep beams. Due to the discontinuity in the stress distribution in deep beams, complex finite element methods (FEM) are often used for modeling and analyzing their behavior. LS-DYNA is one of the most frequently used programs for analysis in civil and structural engineering applications. It has proven to be an essential tool for structural analysis, particularly in predicting dynamic responses and failure mechanisms in complex structures (Markovich et al. 2011; Imani et al. 2015; Jiang and Zhao 2015; Youssf et al. 2015; Polat and Bruneau 2017, 2018; Grassl et al. 2018; Polat 2020a, 2020b, 2022a, 2022b; Polat et al. 2021; Zhao et al. 2021; Polat and Polat 2024; Tang et al. 2024). The program library contains many concrete materials, which can be used with complex parameter inputs, but are generally utilized by users through the default parameter generation option. In this study, the predictability of the capacities of experimentally tested deep beams using the default concrete parameter creation option in concrete materials, often preferred in structural engineering applications, is investigated using the LS-DYNA program.

In this numerical study, four different concrete material models in LS-DYNA – Mat084/085 (Winfrith), Mat159 (CSCM), Mat072R3 (KCC), and Mat016 (Pseudo-TENSOR) – are utilized to analyze the load-carrying capacities of reference deep beams. The study aims to identify the most accurate model for predicting these capacities, analyze stress formations and distributions within the concrete, and assess axial force demands in beam reinforcements for each material model. By doing so, the research seeks to establish a reliable method for estimating the capacity of deep beams, which are typically costly to test experimentally, while enabling the exploration of various beam parameters, such as aspect ratios and reinforcement configurations, without requiring extensive experimental studies.

The reference models are based on the experimentally tested deep beams documented by Rogowsky et al. (1986), where their behavior was thoroughly analyzed. The significance of Rogowsky et al.'s work is well-established and validated by its inclusion in the Commentary R9.9.1.1 of ACI 318-19 (2019) which highlights this study, along with others (Marti 1985; Schlaich et al. 1987), as foundational for understanding deep beam behavior. The continued relevance of this work underscores its impact on contemporary engineering practices, particularly in the design and evaluation of deep beams and their load-carrying capacities.

Additionally, the study contributes novelty by comparatively evaluating these concrete material models to determine the most effective approach for finite element simulations of deep beams. This focus addresses a significant gap in the literature and provides insights into model performance, enhancing reliability in predictions for critical infrastructure applications. By bridging experimental results with advanced numerical modeling, this research offers a practical, cost-effective solution for designing and analyzing deep beams in structural engineering.

Moreover, the study provides a novel contribution by comparatively evaluating these concrete material models to determine the most effective approach for finite element simulations of deep beams. This research highlights the application of four widely used concrete material models in LS-DYNA, a powerful tool for advanced numerical simulations. By focusing on the comparative performance of these models in predicting the behavior of deep beams, the study offers an understanding of their suitability for finite element analysis of similar engineering structures. While prior studies have explored deep beam behavior experimentally, limited work has systematically evaluated these specific material models in the context of deep beam shear strength predictions. This research, therefore, offers practical insights into the use of advanced material models and simulation tools for structural analysis, establishing a reliable and cost-effective approach for analyzing deep beams in critical infrastructure applications.

2. Literature Review

The literature includes a wide range of experimental, analytical, and numerical studies that have employed various methods to predict the strength of deep beams. These diverse approaches are designed to enhance the accuracy and reliability of predictions related to the performance and safety of deep beams in construction and engineering. In this section, key research studies are summarized to highlight the advancements in this field.

Rogowsky et al. (1986) conducted experimental analysis of the shear behavior of reinforced concrete deep beams. The study examined 24 beams, including 7 simply supported and 17 two-span continuous deep beams, with different shear span-to-depth ratios and web reinforcement patterns. The experiments observed a range of behaviors from brittle to ductile, depending on the presence and amount of vertical web reinforcement. The results indicated that horizontal web reinforcement had no significant impact on capacity. The ACI Building Code's predictions for continuous deep beams and those with horizontal shear reinforcement were found to overestimate strength. This study is crucial for understanding the impact of reinforcement patterns on the strength

and behavior of deep beams. Arabzadeh (2020) studied on the impact of different boundary conditions on the behavior of RC deep beams. The study used experimental and theoretical analysis of 43 deep beams with various reinforcement arrangements and boundary conditions. The study concluded that boundary conditions significantly affect ultimate loads, failure modes, and deflections. The study also proposed a method for analyzing deep beams, which shows good agreement with experimental data. Collins et al. (2008) examined the research on shear behavior in beams tested in the past and assessed 1849 tests and evaluated the safety of shear provisions in North America. It was argued that current ACI shear provisions may be unconservative for members with larger effective depths or higher stresses in longitudinal reinforcement. Chen et al. (2019) presented a comprehensive study on the shear strength of reinforced concrete deep beams. The research focused on both simple and continuous deep beams, analyzing their structural behavior, particularly in terms of shear strength. The study employed a combination of experimental observations, nonlinear finite element analyses, and a review of existing test databases. Chen et al. (2020) presented a comprehensive study on shear-transfer mechanisms and strength modeling of reinforced concrete (RC) continuous deep beams. The study involves detailed experimental observations, numerical analysis using finite element methods, and theoretical considerations of various shear-transfer mechanisms. Zargarian and Rahai (2022) conducted a study on continuous RC deep beams strengthened with carbon fiber reinforced polymer (CFRP) strips. The study included experimental and numerical analyses, focusing on the effect of different shear span-to-overall depth ratios and CFRP strip arrangements. Finite element analyses of the tested specimens were developed to simulate experimental specimen behavior. Gedik et al. (2012) investigated the impact of stirrups on deep beam shear failure mechanisms using an analytical tool 3-D Rigid-Body-Spring Model (RBSM). The study examined stress distribution, deformations, crack patterns, and stirrup strain, providing insights into deep beam shear failure mechanisms influenced by stirrups. Ma et al. (2023) explored a data-driven model to predict the shear strength of reinforced concrete (RC) deep beams. They utilized machine learning (ML) algorithms and interpretable models, to compare the performance of different ML models in predicting shear strength. Li et al. (2023) introduced a new shear strength determination method for reinforced concrete (RC) deep beams using a statistical approach. The study employed the Bayesian-Markov Chain Monte Carlo (MCMC) method to establish a new shear prediction model and improve existing deterministic models.

3. Description of the Reference Deep Beam Models

Within the scope of this study, experimental study of Rogowsky et al. (1986) carried on two single-span and four double-span reinforced concrete deep beams with an aspect ratio of 1.0 were considered. In the experimental study, various combinations of vertical and horizontal reinforcement on the behavior of these beams were examined, failure modes and the influence of different reinforcement configurations and quantities on the structural performance of the beams were investigated.

Fig. 1(a-f) shows the reinforcement layout in the reference beams considered in this study. As reported by Rogowsky et al. (1986) the reinforcements were designed in accordance with the ACI Code Sections 11.8.8 and 11.8.9 (ACI 318-83 1983), adhering to both the minimal and maximal vertical and horizontal reinforcement limits: the quantity of shear reinforcement varied from the minimum requirement of 0.0015, as specified by the code, to a value four times greater than this minimum, and the primary flexural reinforcements were carefully chosen to ensure that shear was the predominant mode of failure.

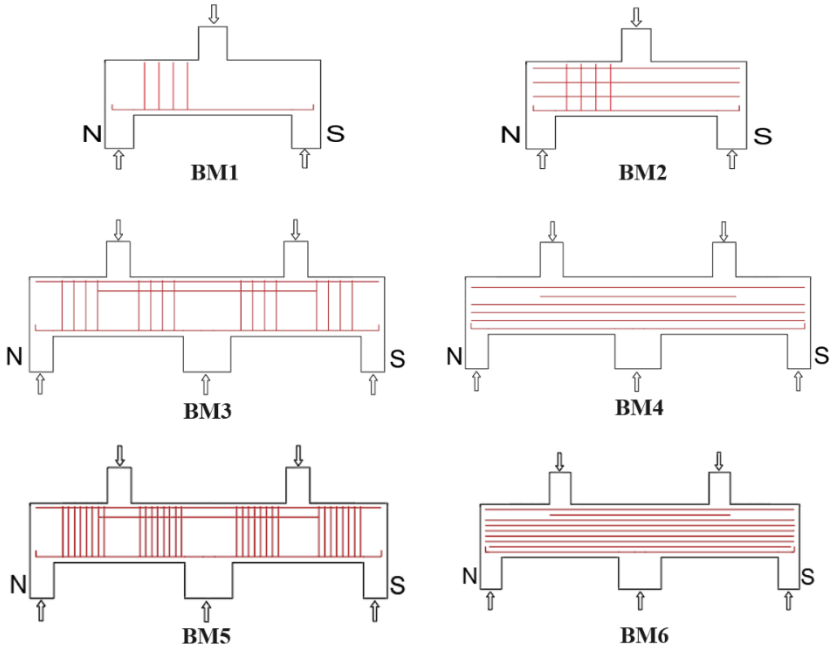

Fig. 1. Reinforcement layout of the reference beams: (a) BM1; (b) BM2; (c) BM3; (d) BM4; (e) BM5; (f) BM6.

The original nomenclature for the beams is maintained in the study. In Fig. 1 'N' and 'S' represent the north and south sides of the beams. As shown in the figure BM1 has stirrups only on the left shear span and no stirrups on the right; BM2 has horizontal body reinforcement at both spans and shear reinforcement only at the left span; BM3 is a continuous beam and has shear reinforcement at all the four span; BM4 is a continuous beam with body reinforcement passing through all spans but does not have shear reinforcement; BM5 is a continuous beam and has heavy shear reinforcement across the four shear spans; BM6 is a continuous beam with a high amount of body reinforcement, but it does not have shear reinforcement.

Table 1 details the properties of concrete and reinforcement used in the test beams. The reinforcement included two types: stirrups with a diameter of 6 mm, and 20M (19.5 mm diameter) bars for the bottom reinforcements. The properties of the reinforcement are given in Table 2. The beams had concrete strengths between 26.1 and 36.9 MPa. The maximum aggregate size used was 10 mm. Fig. 2 presents the typical dimensions of the tested deep beams, both single-span and double-span. The dimensions specified are A = 750 mm, B = 300 mm, C = 450 mm, and D = 1000 mm.

Table 1. Concrete and reinforcement properties of the tested beams (Rogowsky et al. 1986).

Beam models	f_c' MPa	Top reinforcement			Bottom reinforcement			Web reinforcement	
		Number-diameter	$A_s f_y$ (kN)	d (mm)	Number-diameter	$A_s f_y$ (kN)	d (mm)	Number of stirrups	Number of horizontal bars
1	26.1	-	-	-	6-20M	114	950	4	-
2	26.8	2-6 mm	16.2	980	6-20M	114	950	4	4
3	28.9	4-20M	114	950	3-20M	114	975	4	-
4	28.5	4-20M	114	950	3-20M	114	975	-	4
5	36.9	4-20M	121	950	3-20M	121	975	16	-
6	35.8	4-20M	121	950	3-20M	121	975	-	12

Table 2. Properties of steel reinforcement used in tested beams (Rogowsky et al. 1986).

Bar diamater (mm)	$A_s f_y$ (kN)	Yield strain	A_s (mm²)	E (MPa)	f_y (MPa)
20	114	0.00185	302	205400	377-380
6	16.2	0.00210	37.8	273000	428-573

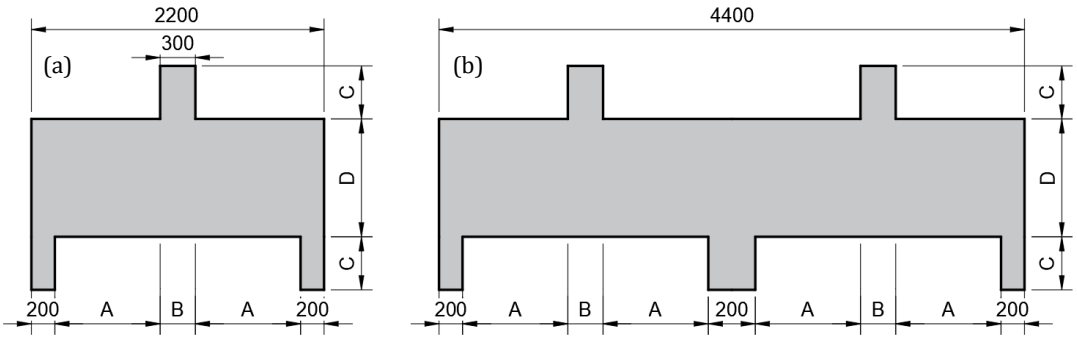

Fig. 2. Typical dimensions of the reference beams: (a) Single-span; and, (b) Double-span.

4. Summary of Experimental Observations

The study of beams BM1 to BM6 showed different failure patterns. BM1 had significant early cracks and a brittle failure due to strong concrete struts. BM2 failed from concrete crushing at strut ends, with early strut formation. BM3, moderately ductile, failed due to concrete strut failure, with major cracks appearing under significant load. BM4 exhibited clear strut formations and failed due to crushing at the strut's top. BM5 had major cracks and less pronounced struts, failing in shear compression at the strut's upper end. BM6, similar in cracking, also failed due to shear compression at the struts' upper ends, with some handling damage noted.

Experimental observations (Rogowsky et al. 1986) identified two main behavior patterns in deep beams. Beams without or with minimal web transverse reinforcement (stirrups) exhibited tied-arch action at failure, independent of the amount of horizontal body reinforcement. These beams, structured with minimal reinforcements, typically failed in a brittle manner following a tied-arch pattern. Conversely, beams with substantial amounts of transverse reinforcement demonstrated more ductile behaviors. This distinction highlights the significant impact of reinforcement type and amount on the failure characteristics of deep beams.

Although designing beams without stirrups is not permissible in practical applications, the referenced experi-

mental study, which forms the basis of this research, aimed to investigate the influence of reinforcement on beam behavior and strength rather than develop design strategies. Shear reinforcement was intentionally removed or omitted on one side of the beams to isolate and examine its impact on shear strength and structural behavior. Similarly, this study focuses on replicating those experimentally tested configurations using finite element models to validate the numerical approach against established experimental results and ensure its reliability in simulating such scenarios.

5. Description of Finite Element Modeling

5.1. Element and material models

In the modeling of the reference deep beams, LS-DYNA was used. In the modeling, the concrete part of the beam was represented by "Solid 1," an eight-node constant-stress solid element (standard solid element model in the software). The beam's transverse and longitudinal reinforcements, which in reality undergo deformations due to axial load, shear force, and bending moments, were modeled using two-node beam elements, known as "Beam 1." (default beam element model in the program).

In the modeling, the concrete elements (solid nodes) and reinforcement elements (beam nodes) were meshed similarly and coupled directly. This approach assumes a perfect bond between concrete and reinforcement, with no slip occurring at the interface. Such an assumption simplifies the modeling process and is a commonly used methodology for representing rebar in concrete structures in numerical simulations.

Additionally, there are constraint-based contact models available in LS-DYNA, such as the CONSTRAINED_LAGRANGE_IN_SOLID (CLIS) keyword, which can achieve similar coupling between concrete and rebar without requiring identical meshing. This method ties the displacement of reinforcement nodes to surrounding concrete nodes, effectively simulating perfect bond behavior. According to Tay et al. (2016), this approach is widely employed in reinforced concrete modeling and has been validated for both static and dynamic applications.

In this study, while a direct mesh coupling was used, CLIS could also have been an effective alternative. Both methods inherently rely on the assumption of perfect bond behavior, which aligns with the configurations and objectives of our research

In the numerical study, a single steel material model was employed for the reinforcements, and four distinct concrete models were utilized. These models include: Mat084/085 (Winfrith), Mat159 (CSCM), Mat072R3 (KCC), and Mat016 (Pseudo-TENSOR). Wu et al. (2012) examined these models' performance in capturing key concrete behaviors through single-element simulations and structural analyses under various load conditions and compared numerical responses with test data to assess each model's effectiveness in predicting actual structural responses. These materials were also used and compared in the analysis of composite plate shear walls (Polat and Bruneau 2018; Polat 2022a).

Mat003 plastic kinematic material model was used for the material modeling of the beam reinforcements. This model demonstrates a bilinear behavior, characterized by a unit strain-stress curve as illustrated in Fig. 3. The required parameters are the yield strength, the elastic modulus (E), the tangent modulus (E_t), and the hardening parameter (β).

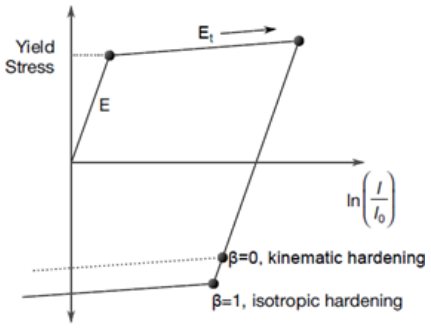

Fig. 3. Illustration of typical stress-strain curve of plastic kinematic material model.

The Mat003 plastic kinematic material model was chosen due to its simplicity and efficiency. This model requires minimal input parameters and is computationally efficient, reducing convergence issues. Given the lack of detailed steel component test history in the reference study and the focus of this research on predicting ultimate strength rather than the complete load-deformation behavior, Mat003 was deemed appropriate for the numerical modeling of beam reinforcements.

The Winfrith Concrete material in the software program is represented by two separate material models, Mat084 and Mat084/085. The Mat084 model includes a specific formulation designed for structural reinforcement. In contrast, the Mat084/085 lacks a formulation tailored for structural reinforcement (LSTC 2017). For Mat084/085 the amount of reinforcement must be specified in the analysis model using different elements through direct, one-to-one modeling. This approach allows for a more detailed and accurate representation of the reinforcement within the structural analysis. The formulation of this material is based on the research of Broadhouse and Neilson (1987) and Broadhouse (1995). This model is commonly employed in the structural modeling of concrete under diverse loading conditions. Its popularity stems from the minimal input requirements, which align closely with the properties of concrete typically used in engineering applications. A notable feature of this material model is its capability to accommodate crack planes in three directions per element (Wittmann et al. 1988). This feature enables the visual simulation of crack formation in analysis results. The essential material parameters required for this model are tangent modulus, poisson's ratio, uniaxial compressive strength, uniaxial tensile strength, crack width, aggregate size.

The Mat159 model, also known as Continuous Surface Cap Model (CSCM), is one of the most commonly used concrete models in LS-DYNA. Users have the option to input their own material properties for normal strength

concrete or request default material properties (LSTC 2017). This model is noted for its efficiency in simulating key concrete properties with minimal user input. The parameters required for the default material properties are uniaxial compressive strength, and aggregate size. Evaluation of this material model has been studied by many researchers (Murray et al. 2007; Winkelbauer 2015; Novozhilov et al. 2022)

Mat072R3 material model is also known as the Karagozian & Case Concrete (KCC) Model and utilizes three shear failure surfaces (LSTC 2017). The foundations of this concrete material model are based on the Pseudo-TENSOR Model (Material Type 16). The latest version, referred to as Rel3 or Version III, generates the required concrete material parameters used in this study based on simple concrete properties. The model is based on partially associative plasticity theory and has the ability to replicate a wide range of concrete behaviors, including hardening, softening, rate effects, confinement, shear dilatancy, and fracture. The model's effectiveness under various loading conditions has been demonstrated by researchers (Wu and Crawford 2015).

The Mat16 model, being a pseudo-tensor model, is particularly suited for materials that exhibit complex mechanical responses, including non-linear behavior, anisotropy, and rate dependency. The material has been used to analyze embedded steel-reinforced concrete structures subjected to impulsive loads. This model is highly suitable for the application of standard geological models such as the Mohr-Coulomb yield surface with the Tresca limit (LSTC 2017).

5.2. Definition of finite element analysis

Fig. 4 shows the finite element models developed for the BM1 and BM3 beams, illustrating the concrete and reinforcement components separately. The analyses were conducted using displacement-controlled loading. Fig. 5 presents the displacement curve established for the analysis, where the horizontal axis (abscissa) represents time, and the vertical axis (ordinate) indicates displacement in millimeters. A displacement of 10 mm is characterized as a linear increment over a 1-second time interval. In the numerical model, this displacement was uniformly applied to the top surface nodes of the column at the mid-span of the beam. Nonlinear analysis was executed using the implicit solution algorithm in the software. In this solution approach, the predefined displacement curve is applied in loading steps (*dt*) of 0.001 seconds.

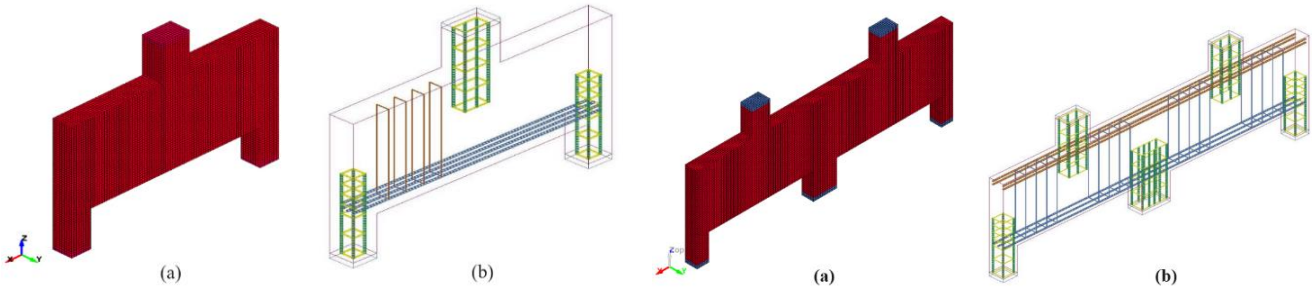

Fig. 4. Finite element models for BM1 and BM3: (a) Concrete part; (b) Reinforcement layout.

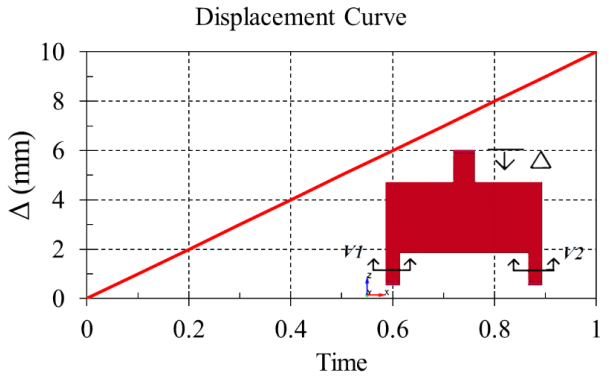

Fig. 5. Time-displacement curve used in analyses.

The tolerances used in the nonlinear analyses were set to the default values provided by LS-DYNA for implicit simulations to ensure consistent and reliable convergence. Specifically, the convergence tolerance for residual forces (TOL) was set to 1.0×10^{-9}. The minimum allowable time step size (Δt_{min}) was 1.0×10^{-8}, while the maximum allowable step size increment (Δt_{max}) was 0.004.

The shear strengths of the analysis models were obtained by adding up the shear forces generated in each span (left and right) of the beam. For instance, in the numerical model, the shear force demand for the left span of the beam model was determined by measuring the axial force demand (in the *z* direction) at a cross-section located at the beam's left support. Likewise, the shear force demand for the right span was ascertained by measuring the axial force demand at a cross-section at the right support. The overall shear carrying capacity of the numerical model was calculated as the sum of these two support reactions (i.e., V1 + V2).

It should be noted that a convergence study was conducted to establish the appropriate element sizes for the numerical beam model. Considering the distribution of transverse and longitudinal reinforcements and their spacings within the concrete of the beam, two element sizes were evaluated: 50 mm and 25 mm. These sizes were selected to enable as accurate as possible modeling of the reinforcements, resembling the actual tested specimen. The nodes of the beam elements used for reinforcements were aligned with the nodes of the solid elements, allowing the reinforcement to be coupled in dis-

placements with the concrete. This was achieved by merging the mutual nodes, ensuring that the reinforcement elements and the concrete elements moved in a dependent manner. To facilitate this integration, the dimensions of the reinforcement beam elements were made identical to those of the solid elements, that is, 50 mm or 25 mm in length.

Note that the element sizes used in this study (50 mm and 25 mm) were chosen considering the geometrical dimensions of the beam, the layout of the main and shear reinforcement, and the spacing between the rebars. Using finer meshes would result in excessively short beam elements for the reinforcement, given the 20mm diameter of the rebar. This could introduce numerical inaccuracies and undesired effects in the modeling of reinforcement behavior. Additionally, finer mesh resolutions would significantly increase computational cost. While intermediate sizes between 50mm and 25mm could improve robustness, the current configurations were deemed sufficient for accurately predicting ultimate strength within the scope of this study.

The model was set up as a simply supported beam with fixed boundary conditions at one end and roller support at the other, restricting vertical and transverse displacements while allowing longitudinal translation. Prescribed displacements were applied at the load application points. For the mesh sizes used, the total number of degrees of freedom (DOF) was approximately 78,000 for the 50mm mesh and 264,000 for the 25mm mesh. The beam reinforcements were modeled using beam elements coupled to the concrete solid elements through a constraint-based coupling method to simulate a perfect bond. The concrete was represented with the Mat084 material model, and the reinforcement with the Mat003 plastic kinematic material model. Hourglass control was applied to maintain numerical stability.

Fig. 6 displays the shear force-deflection curves derived from the nonlinear inelastic analysis results of the numerical beam models with two distinct mesh sizes. Additionally, the figure includes the experimentally determined maximum shear force capacity of the reference beam for comparison purposes. The findings from these outcomes reveal that the analysis result obtained with the model featuring a 50mm mesh size exhibited a strength that surpasses the actual beam strength upon comparison. Conversely, the analysis results from the model with a 25 mm mesh size exhibited a strength lower than the former and its results closely aligned with the actual beam's maximum shear strength.

It should be noted that the observed jumps in Fig. 6 are a result of the behavior of the numerical model during the nonlinear analysis, particularly in relation to the concrete material model (Mat084) used in the convergence study. The Mat084 concrete model has the ability to simulate concrete cracking, which results in the formation of sudden shear cracks in the beam. This leads to abrupt changes in the structural response, causing the sudden drops in the observed beam strength displayed in Fig. 6.

However, it is important to note that the finite element (FE) simulation used in this study does not explicitly model concrete failure or element erosion. As a result, the model does not capture the softening behavior of the concrete or the subsequent beam failure after reaching the maximum strength. This limitation contributes to the sharp transitions observed in the load-deflection curves.

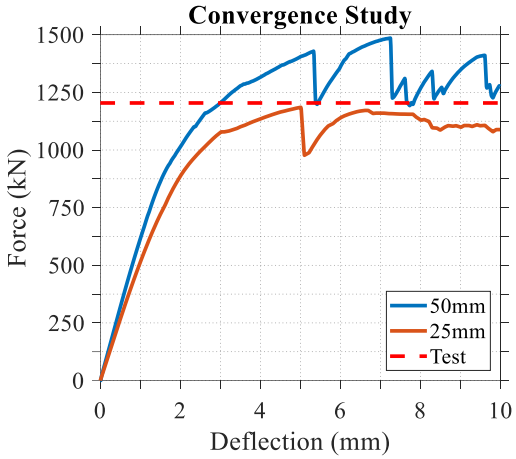

Fig. 6. Comparison of the numerical model results for the convergence study.

6. Finite Element Analysis Results

In this section, comparisons are made of the global load-displacement curves of beams subjected to nonlinear inelastic analyzes using different concrete materials, taking into account the experimentally measured beam strengths. Additionally, the axial force demands on the reinforcements for each model are examined. This approach allows for a comprehensive assessment of how different concrete materials affect the overall structural response of the beams, as well as the specific demands placed on the reinforcements under different material models.

It should be noted that comparing the overall beam behavior, such as force-displacement analysis, requires explicit modeling of not only the specimen but also the test setup itself. This is because the stiffness of the tested specimen can be influenced by various factors, such as deformation in the loading equipment, stiffeners, or slippage at the beam supports. Properly replicating these conditions in the FE model is a demanding task and requires careful calibration, including considerations such as friction between components, the modulus of elasticity of the concrete, and other parameters. Due to these complexities, no attempt was made to calibrate the stiffness of the numerical models or to replicate the entire nonlinear behavior of the specimens. Instead, the focus of the study was on predicting the ultimate strength of the beams, which is independent of these factors. The decision to prioritize ultimate strength stems from its inherent stability against variations in external testing conditions, ensuring a more robust comparison of material models.

The analysis results indicate that the beams exhibit a truss-like behavior within the concrete, characterized by the formation of diagonal compression struts. Fig. 7 presents the minimum principal stress contours for BM1 across the different concrete material models. These

contours highlight the development of diagonal compression struts, which are crucial for understanding the distribution of internal stress and overall structural performance of the beams. The stress contours for the Mat084 and Mat159 models are significantly more pronounced than those for the Mat072R3 and Mat016 models, reflecting the varying responses of the beams under the specified deflection. This distinction in stress contour prominence corresponds to the differing strengths retained by the beams under load. Specifically, the beams analyzed with the Mat084 and Mat159 models maintain a greater degree of strength, while those analyzed with Mat072R3 and Mat016 exhibit moderate to significant strength losses, respectively. In the case of the Mat072R3 model, there is a notable localized loss of minimum principal stress, which is attributed to the significant yielding of the shear reinforcements at the given deflection. This yielding alters the stress distribution within the concrete, affecting the formation and integrity of the diagonal compression struts. These phenomena, particularly the reinforcement behavior and its impact on stress distribution, are explored in greater detail in the force-displacement curves discussed in the subsequent sections.

Fig. 8 illustrates the minimum principal stress contours for BM3 across the different concrete material models analyzed in this study. The results reveal that the formation of compression struts is notably pronounced in the interior shear spans of the beam compared to the exterior spans. This indicates that the force distribution is more concentrated in the interior spans of these double-span beams, making them more critical in terms of load transfer. Consequently, the reinforcement in the interior shear spans is expected to experience more significant yielding than that in the exterior spans. This observation aligns with the force-flow mechanisms typical of such structural systems and is further explored in detail in the following sections of the study, where the impact of reinforcement and material behavior on the overall structural performance is thoroughly analyzed.

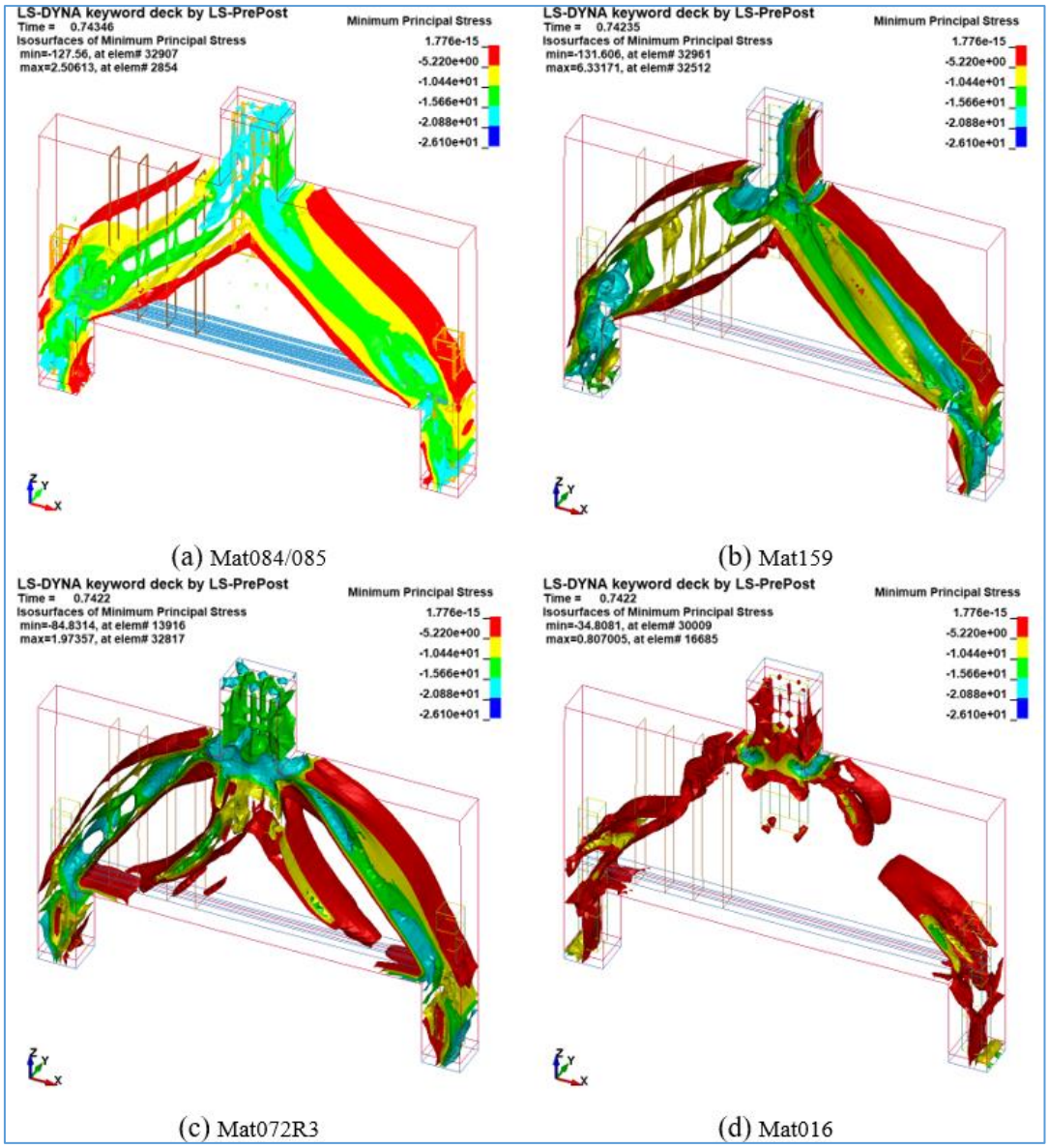

Fig. 7. Minimum principal stress distributions of BM1 at deflection of 7.5mm: (a) Mat084/085; (b) Mat159; (c) Mat072R3; (d) Mat016.

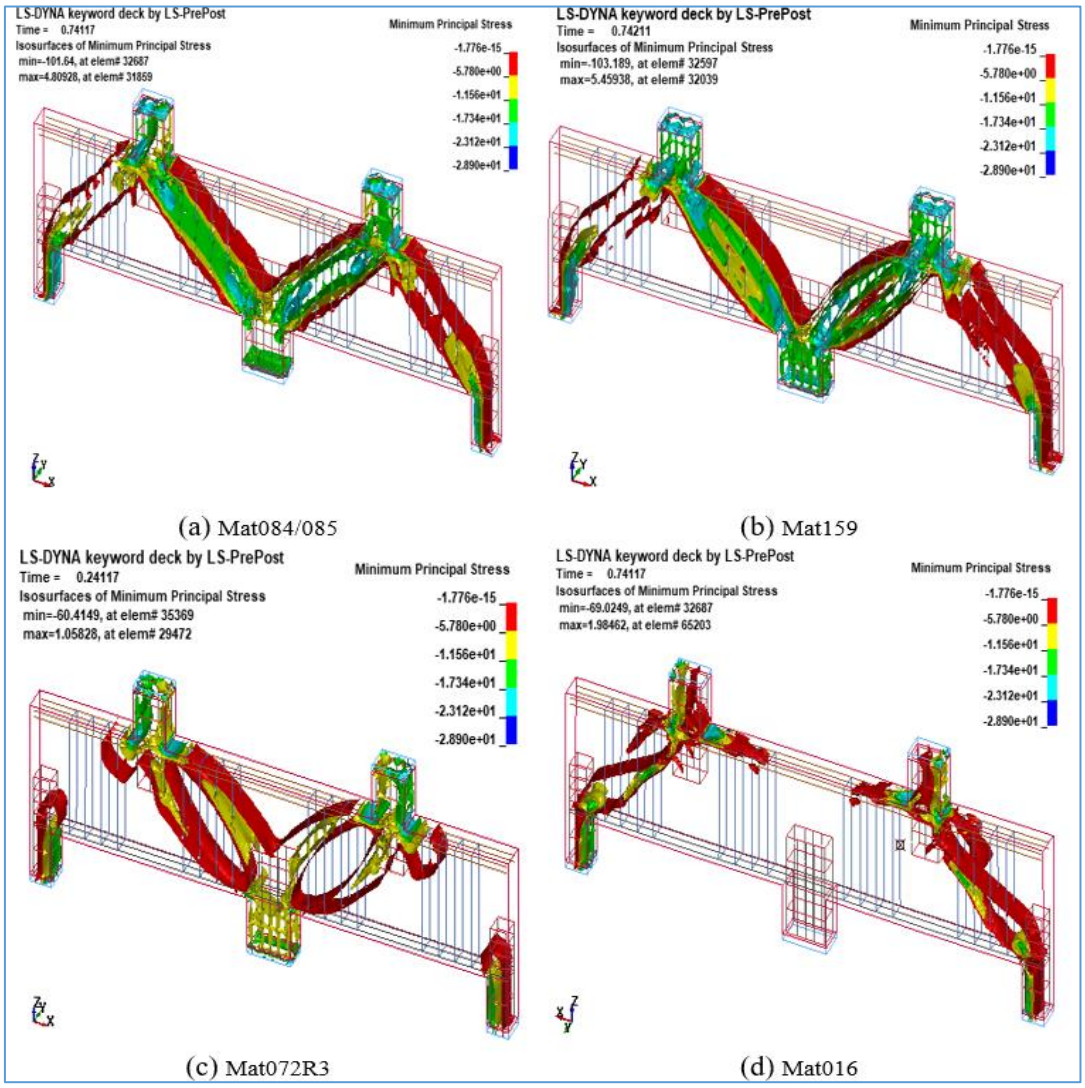

Fig. 8. Minimum principal stress distributions of BM3 at deflections of 7.5mm: (a) Mat084/085; (b) Mat159; (c) Mat072R3; (d) Mat016.

6.1. Global load-displacement response

Fig. 9 shows the shear-deflection response of the numerical simulations for six reference beams (BM1, BM2, BM3, BM4, BM5, and BM6) derived from nonlinear inelastic FE analysis. The behavior of each beam model was assessed using four different concrete material models (specifically, Mat84/85, Mat159, Mat071R3, and Mat16) alongside a single steel material model (Mat003 Plastic Kinematic). Fig. 9 also includes experimentally measured maximum shear strengths of the beams for comparison with the numerical outcomes.

For BM1, the experimentally measured maximum strength was 1204 kN, achieved at a deflection of approximately 5.5 mm. The numerical predictions for maximum shear strength using different material models yielded the following results: Mat084/085 approximated 1190 kN at 5.5 mm deflection, Mat159 predicted 1282 kN at 5 mm, Mat072R3 estimated 1079 kN at 4.7 mm, and Mat016 calculated 1085 kN at 2.5 mm. The discrepancies between these numerically obtained values and the experimental measurement were 1.2%, 6.4%, 10.0%, and 9.8%, respectively.

For BM2, the experimentally measured maximum beam strength was 1500 kN, achieved at a deflection of approximately 6.2 mm. It is important to note that BM2, in contrast to BM1, featured distributed body reinforcement. Regarding the numerical models, using Mat084/085, Mat159, Mat072R3, and Mat016, the predicted maximum shear strengths were approximately 1202 kN at 2.27 mm deflection, 1361 kN at 6.3 mm, 1119 kN at 4.4 mm, and 1110 kN at 5.7 mm, respectively. The discrepancies between these numerically obtained results and the experimentally measured value were about 19.86%, 9.26%, 25.3%, and 25.9%. When comparing the actual strengths of BM1 and BM2, it is observed that the inclusion of body reinforcement in BM2 increased the beam strength from 1204 kN to 1500 kN, indicating a substantial increase of 24.58%. However, this enhancement in strength was not reflected in the numerical results.

For BM3, the experimentally determined maximum strength of the beam was 2170 kN, achieved at a deflection of approximately 6.1 mm. It's noteworthy that BM3 is a continuous beam with shear reinforcement across all four spans. In the numerical models using Mat084/085, Mat159, Mat072R3, and Mat016, the predicted maxi-

mum shear strengths were approximately 1950 kN at 2.27 mm deflection, 2263 kN at 6.3 mm, 1830 kN at 4.4 mm, and 1740 kN at 5.7 mm, respectively. The differences between these numerically obtained results and the experimentally measured value were about 10.13%, 3.83%, 15.66%, and 19.81%, respectively.

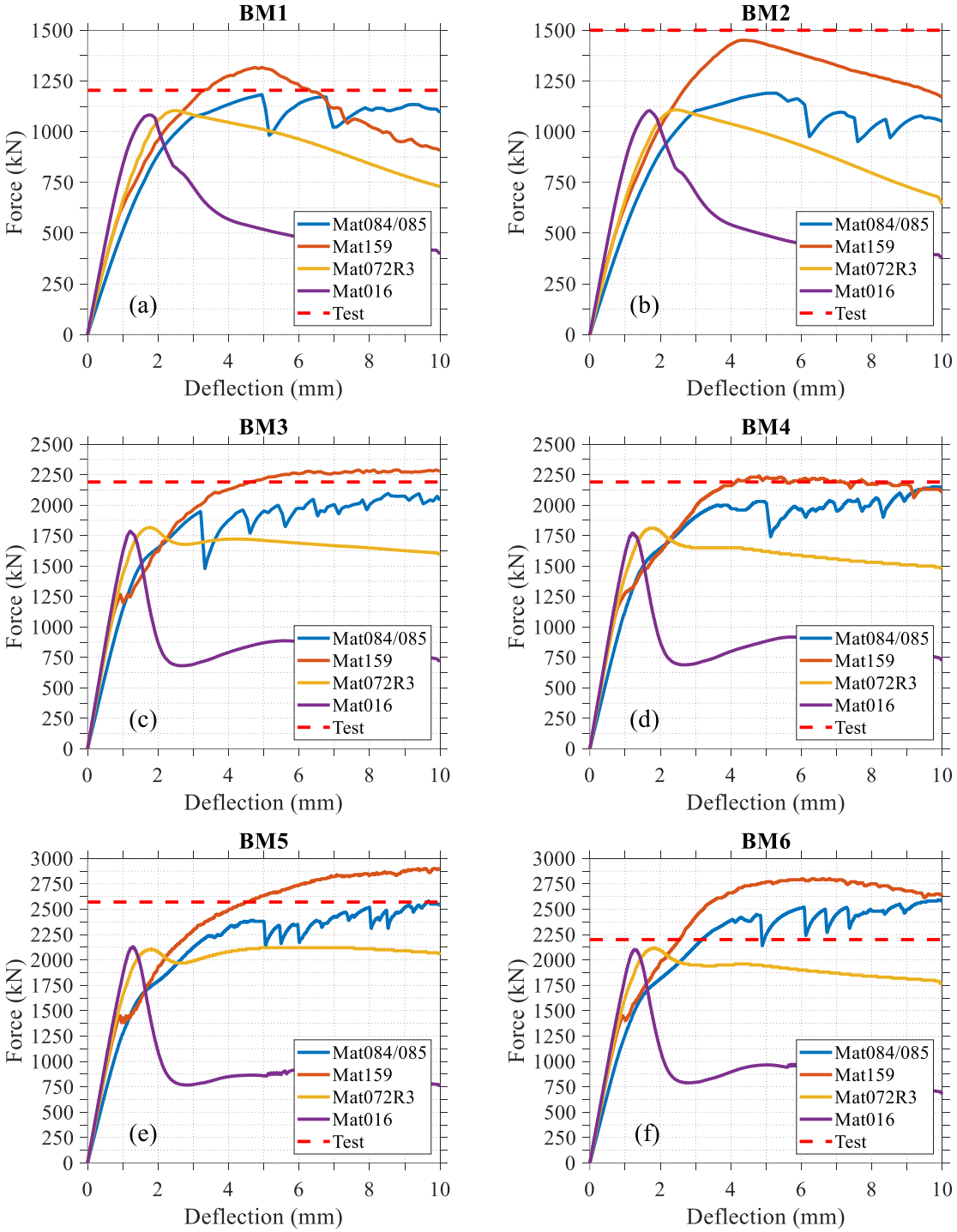

Fig. 9. Shear-deflection curves: (a) BM1;(b) BM2; (c) BM3; (d) BM4; (e) BM5; (f) BM6.

For BM4, the experimentally measured maximum strength of the beam was 2176 kN, achieved at a beam deflection of approximately 7.0 mm. Notably, BM4 is a continuous beam with body reinforcement extending through all spans, but it lacks shear reinforcement. In the numerical models using Mat084/085, Mat159, Mat072R3, and Mat016, the predicted maximum shear strengths were approximately 2035 kN at 5.0 mm deflection, 2240 kN at 6.2 mm, 1810 kN at 2.2 mm, and 1770 kN at 1.7 mm, respectively. The discrepancies between these numerically obtained results and the experimentally measured value were about 6.5%, 2.9%, 16.8%, and 18.7%. Upon comparing the actual strengths of BM3 and BM4, and considering that BM3 used stirrup reinforcement while BM4 used web reinforcement without stirrups, it was observed that stirrups contribute to a greater increase in beam strength than body reinforcement.

For BM5, the experimentally measured maximum strength of the beam was 2571 kN, achieved at a beam deflection of approximately 8.5 mm. It's important to note that, similar to BM4, BM5 is a continuous beam with body reinforcement throughout all spans but lacks shear reinforcement. In the numerical models using Mat084/085, Mat159, Mat072R3, and Mat016, the predicted maximum shear strengths were approximately 2385 kN at 5.0 mm deflection, 2840 kN at 6.1 mm, 2120 kN at 2.1 mm, and 2100 kN at 1.7 mm, respectively. The differences between these numerically obtained results and the experimentally measured value were about 7.2%, 10.5%, 17.5%, and 18.3%. When compared to beams with lighter shear reinforcements, it was observed that the use of heavy stirrups in BM5 significantly enhanced the beam strength.

For BM6, the experimentally measured maximum strength of the beam was 2198 kN, reached at a deflection of approximately 5.5 mm. Notably, BM6 is a continuous beam with heavy horizontal body reinforcement spanning all spans but lacks shear reinforcement. It's also important to acknowledge that the specimen suffered some damage during handling, which might impact the realism of the comparison. Nonetheless, similar numerical model comparisons were conducted for this beam as well. Using the numerical models with Mat084/085, Mat159, Mat072R3, and Mat016, the predicted maximum shear strengths were approximately 2430 kN at 6.0 mm deflection, 2780 kN at 6.1 mm, 2120 kN at 1.8 mm, and 2100 kN at 1.2 mm, respectively. The discrepancies between these numerically obtained results and the experimentally measured value were about 10.6%, 26.5%, 3.5%, and 4.5%.

The observed differences in the results between the material models are due to the inherent mathematical formulations and assumptions underlying each model. These models differ in how they represent concrete behavior under varying loading conditions, including stress-strain relationships, failure criteria, and damage mechanisms.

MAT072R3 (K&C Model) utilizes three failure surfaces to capture yield, maximum, and residual strength. However, it often overestimates the degradation of compressive strength and does not account for stiffness reduction under loading, leading to discrepancies in strength and deformation predictions. MAT084/085 (Winfrith Model), based on a smeared crack approach, assumes elastic-perfectly plastic behavior in compression with bilinear strain softening in tension. While effective in some applications, it may not capture strength degradation under highly nonlinear scenarios. MAT159 (CSCM Model) uses a continuous surface cap model that combines shear failure and hardening compaction surfaces, allowing simulation across a wide range of stress states. Although versatile, it can overestimate parameters like tensile fracture energy. MAT016 (Pseudo-Tensor Model) is a simpler model with lower computational requirements but limited accuracy in capturing complex stress states and nonlinear behavior.

The differences arise primarily due to how each model addresses key aspects of concrete behavior. Advanced models like MAT159 incorporate explicit damage mechanics, whereas others, like MAT084, use smeared approaches. Stress-strain relationships differ in how they handle tension softening, compression hardening, and strain rate effects. Additionally, variations in yield surfaces and failure envelopes significantly influence strength and deformation predictions.

6.2. Axial force demands of stirrups

In this section, axial force demands in the beam stirrups under a range of beam deformations (i.e., Δ=1, 2.5, 3.0, 3.5, 6.0, 10 mm) are examined considering different concrete models. Due to page limitations, the results are discussed using only two beam models: BM1, representing a single-span beam, and BM3, representing a continuous beam. For BM1, the analysis covers the four shear reinforcements located in the left shear span, positioned at distances of 350 mm, 500 mm, 650 mm, and 800 mm from the beam's left end. In the case of BM3, the results pertain to eight shear reinforcements. These are located in both an interior and an exterior shear span of the beam's half symmetric span. Specifically, the shear reinforcements in the exterior shear span are placed at distances of 350 mm, 500 mm, 650 mm, and 800 mm from the left end of the beam. Those in the interior shear span are situated at 1400 mm, 1550 mm, 1750 mm, and 1850 mm from the left end.

For BM1, the axial force distribution for each stirrup is detailed in Fig. 10 to 12, corresponding to the material models Mat084/085, Mat159, and Mat072R3. Notably, results pertaining to Mat016 are excluded, as they were deemed unreasonable. When analyzing the distribution of axial forces in the four shear reinforcements located in the left span of the BM1 model, a notable observation is that the axial forces concentrate in a specific region along the length of the reinforcement. This concentration of axial forces correlates with the diagonal compression strut shape illustrated in Fig. 7. Essentially, the length of the shear reinforcement experiencing the most significant axial force concentration corresponds to the region where the minimum principal stresses occur in the concrete. This indicates a direct relationship between the stress patterns in the concrete and the distribution of axial forces within the shear reinforcements.

When analyzing the axial force demands on the shear reinforcement for different concrete models, it was found that yielding in the reinforcements was most pronounced in the Mat072R3 model, followed by the Mat084/85 model, and least in the Mat59 material. For the Mat159 model, yielding was observed only in the second shear reinforcement (located at X=500mm) at the maximum deformation of 10mm. The other shear reinforcements in this model generally remained within the elastic range. In contrast, for both the Mat84/85 and Mat72 models, the onset of yielding in the shear reinforcement began at approximately 6 mm deformation. In these two material models, yielding was observed in almost all of the four shear reinforcements within the shear span, indicating a more widespread distribution of yielding across the reinforcements in response to beam deformation.

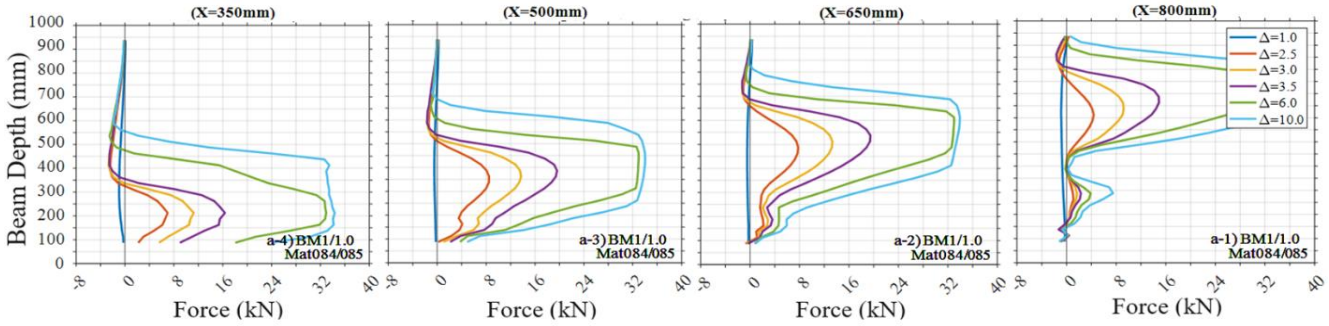

Fig. 10. Axial force demands of stirrups of BM1 using Mat084/085.

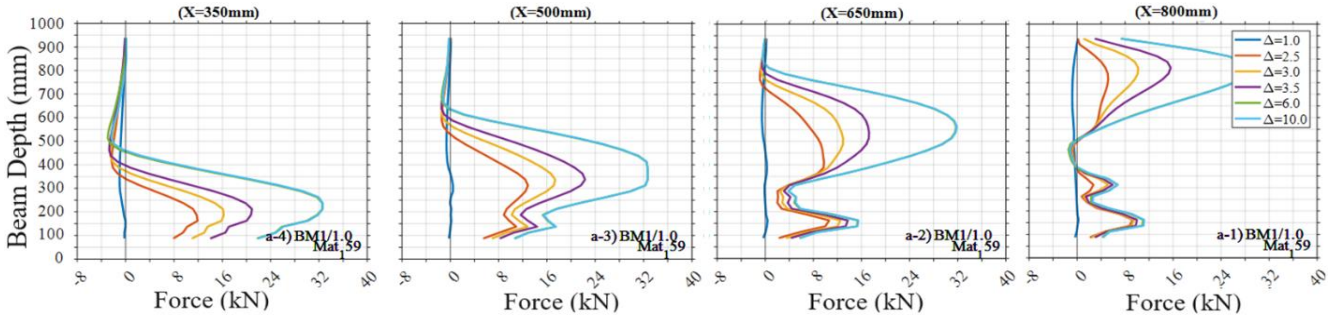

Fig. 11. Axial force demands of stirrups of BM1 using Mat159.

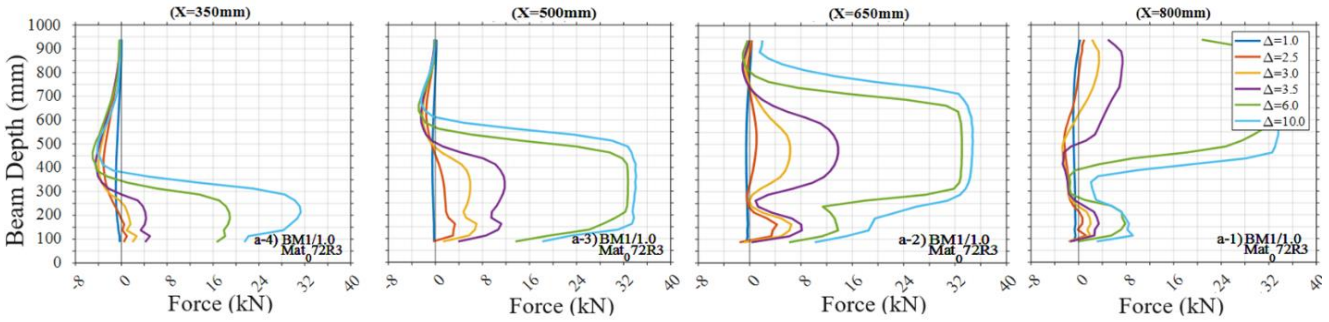

Fig. 12. Axial force demands of stirrups of BM1 using Mat072R3.

For BM1, the axial force distribution for each stirrup is detailed in Fig. 13 to 15 corresponding to the material models Mat084/085, Mat159, and Mat072R3. In the examination of the axial force distribution on the eight shear reinforcements in the first span of the continuous beam BM3 model, a pattern similar to that observed in the BM1 model is evident. The axial forces on the shear reinforcements in BM3 are found to concentrate in specific regions along the lengths of the reinforcements. These areas of concentration align with the pattern of the diagonal compression struts, as depicted in Fig. 8. This observation indicates that, just as in the BM1 model, the regions on the shear reinforcements where axial forces are most intense correspond to the areas where the diagonal compression struts are formed in the concrete.

In the analysis of the axial force demands on the shear reinforcements in the continuous beam BM3 model, a notable distinction is observed between the exterior and interior shear spans. The first four shear reinforcements, located in the exterior span, experience significantly lower axial force demands compared to the subsequent four reinforcements in the interior span. Specifically, for the Mat72 model, the axial force demands on the reinforcements in the exterior span are almost negligible. Regarding the yield ratios in the shear reinforcements: In the exterior span, the highest yielding is seen in the Mat084/85 model, followed by the Mat159 model, and the least in the Mat072R3 model. In the interior span, the highest yielding is observed in the Mat072R3 model, then the Mat84/85 model, and finally, the Mat159 model.

For the shear reinforcements in the interior span across all material models, the yield ratios are predominantly higher in the middle regions of the shear span. Moreover, all reinforcements yield at the maximum beam deformation. In the Mat84/85 and Mat72R3 models, the first yielding in the reinforcements occurs at a beam deformation of 3.5 mm, while in the Mat159 model, it starts at a deformation of 6 mm. In terms of the extent of yielding: In the Mat84/85 and Mat72R3 models, yielding occurs along more than 50% of the reinforcement length. For the Mat159 model, this yielding ratio is around 20%. This analysis highlights the differences in the axial force demands of shear reinforcements in different spans and under various material models, especially in terms of yielding patterns and axial force demands.

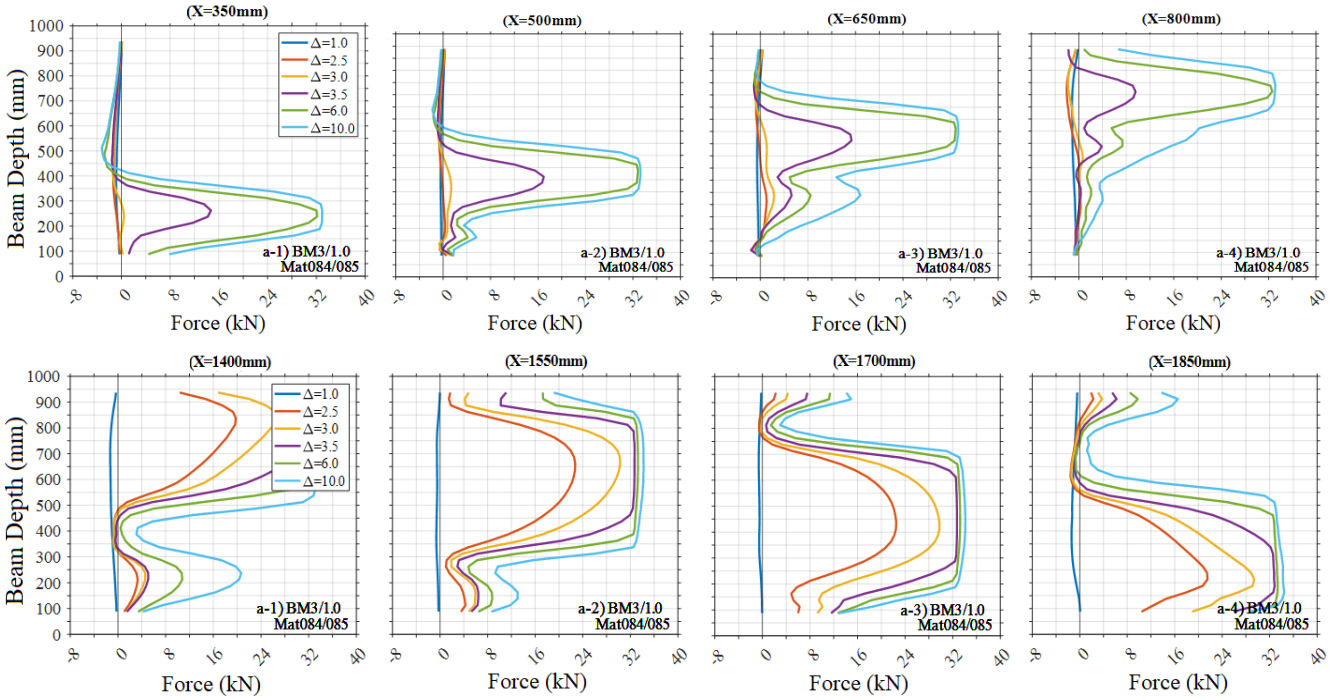

Fig. 13. Axial force demands of stirrups of BM3 using Mat084/085.

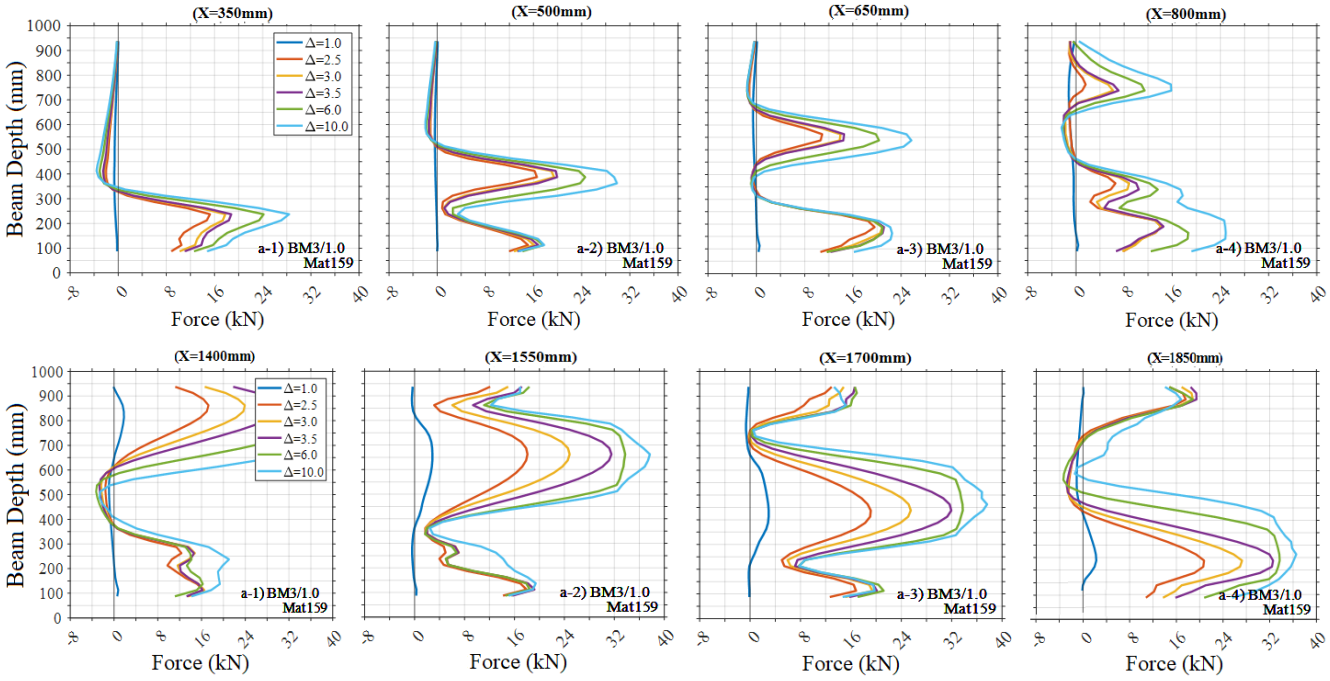

Fig. 14. Axial force demands of stirrups of BM3 using Mat159.

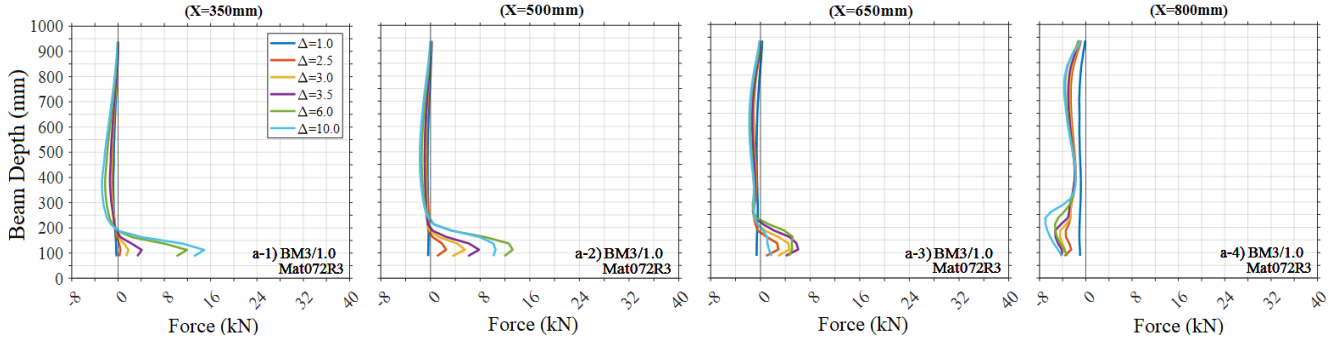

Fig. 15. (continued)

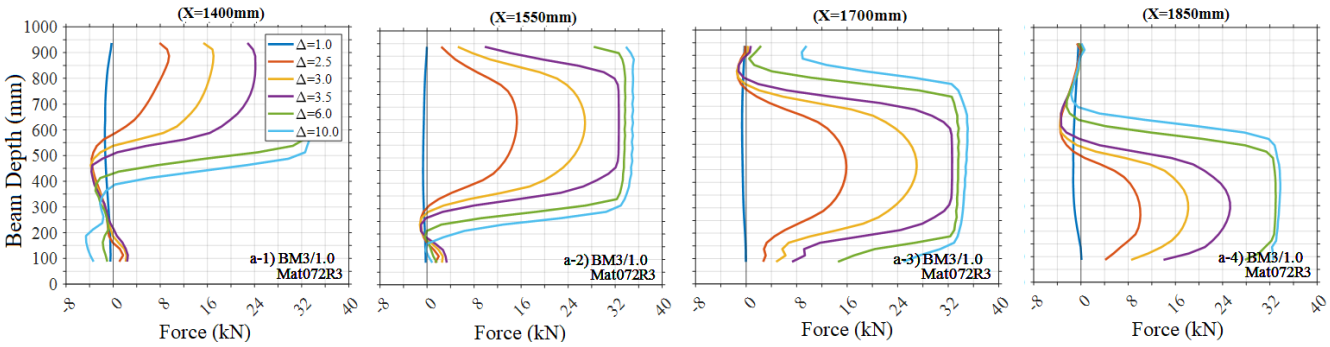

Fig. 15. Axial force demands of stirrups of BM3 using Mat072R3.

The reported findings for the tested beams reveal different patterns of yielding and failure mechanisms: For BM1: Yielding was observed in both the shear and the bottom longitudinal reinforcements before the collapse of the beam. The distribution of tensile force in the longitudinal reinforcement at failure was almost constant, suggesting a uniform stress state along its length. This indicates that both shear and flexural capacities were critical in the failure process; For BM2: Both the shear and longitudinal reinforcements yielded before the beam collapsed. This suggests a combined influence of shear and flexural stresses leading to the failure, similar to BM1; For BM3: Yielding occurred in the main (longitudinal) reinforcement, indicating a flexural failure mechanism. The beam was described as moderately ductile, which implies it underwent significant deformation, typically associated with flexural yielding, before collapsing; For BM4: Yielding in the lower steel reinforcement was noted significantly before the collapse, pointing towards a flexural failure mechanism. This early yielding suggests that the beam's failure was primarily governed by flexural stresses; For BM5: All shear reinforcements yielded, leading to the separation of the struts, indicative of a shear failure. Additionally, the longitudinal reinforcements were under tensile stresses along the entire length of the internal shear spans. However, there was a more pronounced decrease in stress towards the ends of the span compared to the BM3 model, suggesting different stress distributions and possibly different failure mechanisms between the two beams.

6.3. Axial force demands of main reinforcements

In this section, the axial force demands of the longitudinal reinforcement bars located in the bottom regions of the beams were examined for varying beam deformations. The analysis and comparisons are based on the BM1 model, representing a single-span beam, and the BM3 model, representing a continuous beam. To recall the key aspects of the reinforcements in these models: For BM1 (and BM2) there are two rows of bottom reinforcements. Each row consists of 3ϕ20 bars. For BM3 (and BM4, BM5, and BM6) there is only single row of bottom reinforcements, with each row also containing 3ϕ20 bars. The positioning of the reinforcements is such that the center of the first-row reinforcements is located 25 mm above the concrete's outer surface, while the second-row reinforcements are positioned 50 mm above the surface. For BM1, the results are presented as the sum axial force acting on the three bars in a single row. It's noted that the axial force demands on the second-row reinforcements are nearly the same. The average axial force demands of the three bars in a single row are given at beam deflections of Δ=1.0, 2.0, 3.0, 3.5, 6.0, and 10 mm. Note that, the measured tensile strength of the reinforcement materials are 114 kN for models between BM1 to BM4, and 121 kN for models BM5 and BM6. This analysis aims to understand how the axial forces in the longitudinal reinforcements vary under different levels of beam deformation and how these forces are influenced by the reinforcement arrangement and material characteristics in various beam models.

For BM1, the axial force demands on the longitudinal reinforcements under increasing beam deformations are presented in Fig. 16, considering four different concrete materials. The key observations for this model are as follows: For Mat084/85 and Mat159 Models yielding of the reinforcements is observed. The reinforcements remained elastic up to a beam deflection of 6 mm, with yielding commencing after this point. In the Mat084/85 model, about 65% of the longitudinal reinforcements yielded, while in the Mat159 model, 50% yielded. Yielding started from the midspan and spread towards the supports. Near the supports, a decrease in axial force demands was noted, suggesting that the reinforcements remained elastic in these areas. For the Mat072R3 model, the reinforcements stayed elastic throughout the entire beam length. However, the axial force demands decreased from the midspan towards the supports. The axial forces reached about 70% of the yield strength of the reinforcements. For the Mat016 model, after a beam deflection of 2 mm, the axial force demands on the longitudinal reinforcements remained constant along the entire length of the beam. These forces corresponded to approximately 30% of the yield strength of the reinforcements. These findings indicate a significant variation in the behavior of the longitudinal reinforcements under different concrete models and beam deformations.

For BM3, the axial force demands on the longitudinal reinforcements under increasing beam deformations are presented in Fig. 17, considering four different concrete materials. The single bar yield strength for this beam is 114 kN, resulting in a total yield force of 342 kN for the bottom row of beam reinforcement. Yielding occurred in all models that used the four different concrete materials.

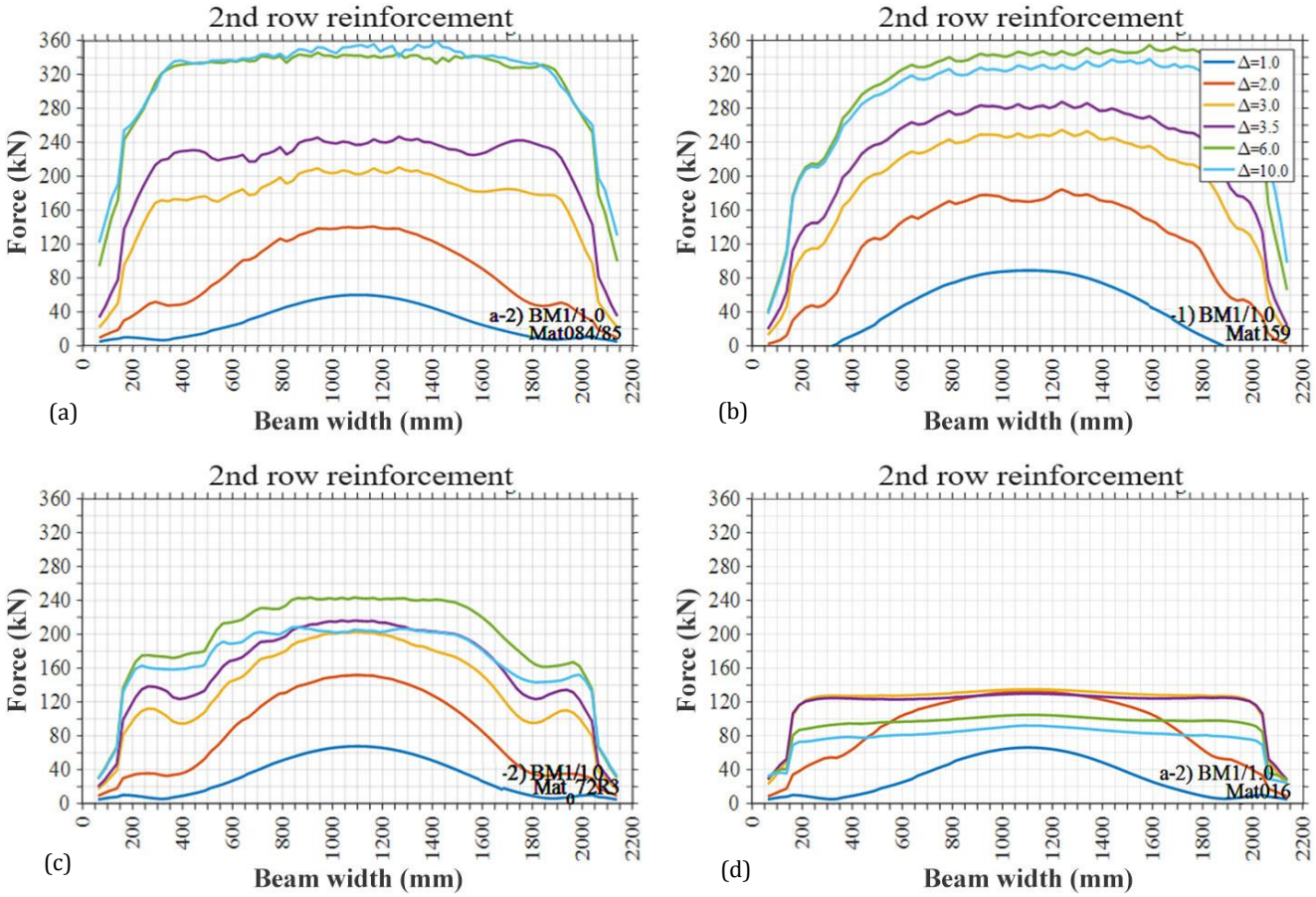

Fig. 16. Axial force demands of longitudinal reinforcement of BM1:
(a) Mat084/085; (b) Mat159; (c) Mat072R3; (d) Mat016.

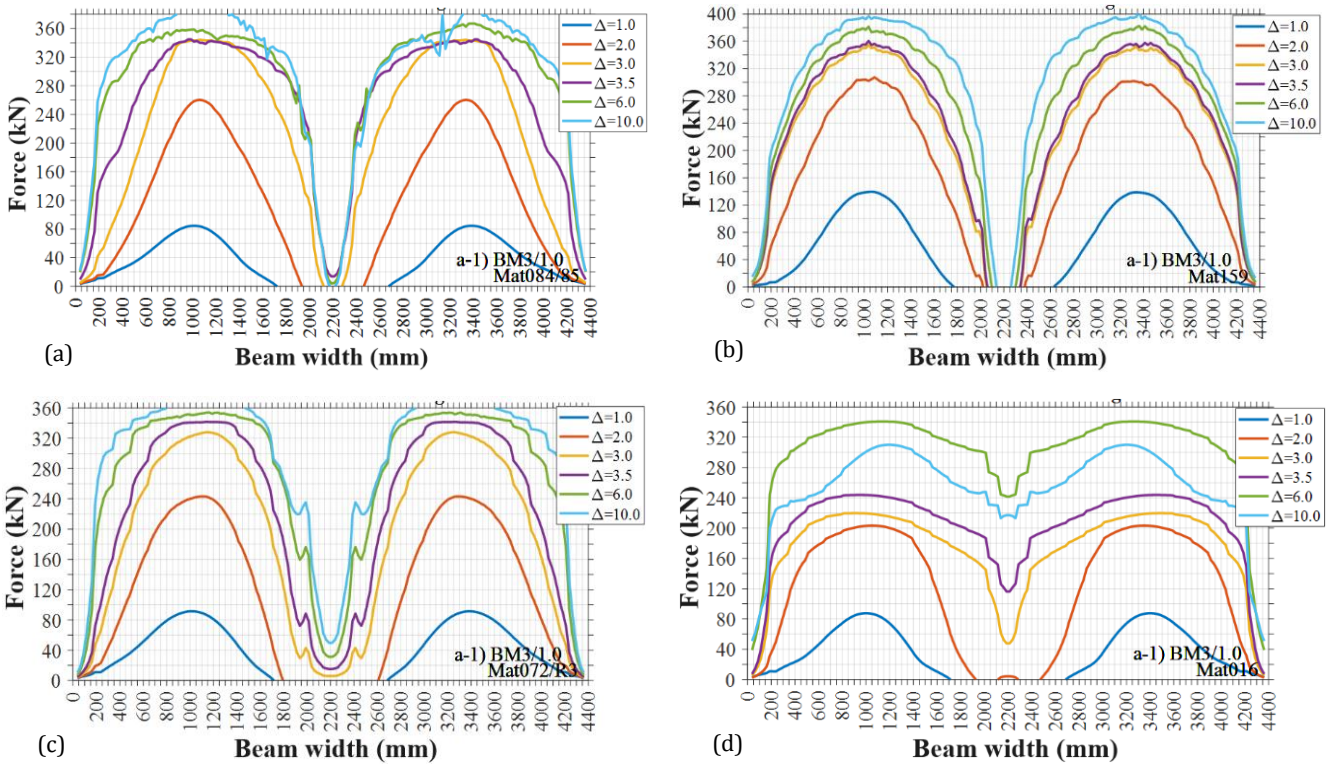

Fig. 17. Axial force demands of longitudinal reinforcement of BM3:
(a) Mat084/085; (b) Mat159; (c) Mat072R3; (d) Mat016.

In the Mat084/85, Mat159, and Mat072R3 models, yielding in the reinforcements started at approximately 3.5 mm beam deformation. The axial force demands in the reinforcements of these three models showed similar behavior along the beam length, with axial force distributions being generally symmetric across both spans. In these models, the axial force demand in the reinforcements reached its peak in the midspan of the beam spans, then decreased and approached zero towards the mid-span and end supports. In contrast, the Mat016 model displayed a different behavior, with reinforcement yielding observed only under high beam deflection, specifically at 10 mm. The distribution of axial force demands in the reinforcements along the beam length in this model was different from the other three models. While the other three concrete models had almost zero axial force demand in the central support region, the reinforcements in this region in the Mat016 model experienced some level of force demand.

These observations indicate a range of behaviors in the longitudinal reinforcements under varying concrete models and beam deformations. The yielding patterns, axial force demands, and their distribution along the beam length vary significantly, reflecting the influence of concrete material properties and the structural response to loading.

7. Conclusions

This study presents an efficient and cost-effective method for evaluating the shear capacity of reinforced concrete deep beams using LS-DYNA, offering a reliable alternative to extensive experimental testing. The analysis of four different concrete models provided insights into the most accurate approaches for predicting beam capacities. These findings can be important for enhancing the resilience of critical urban infrastructure, such as bridges and foundations. By optimizing deep beam designs, engineers can create more durable, disaster-resistant structures, contributing to the long-term sustainability and safety of rapidly growing cities. The study has the following outcomes:

- Significant differences in strength predictions and the distribution of reinforcement forces among different material models were observed. Among the various materials used, the Mat159 model provided the most accurate estimate of the experimentally measured beam shear strength. While the beam strengths obtained with this material are on the conservative side, the percentage differences between the computational results and the values measured in experimental studies were found to be 6.4%, 9.3%, 3.8%, 2.9%, and 10.5% for BM1, BM2, BM3, BM4, BM5, respectively. For BM6, the difference was notably higher at 26.5%. It is important to note that the BM6 model experienced damage during the test setup. Moderate prediction was achieved using the Mat084/85 model. The analysis results obtained using the Mat072R3 and Mat016 models underestimated the measured beam carrying capacity values. The analysis results obtained using the Mat016 model exhibited very poor performance in predicting the measured beam carrying capacity, as well as the principal stress distributions within the beam and the axial force demands on the beam reinforcements.
- Similar to the findings in experimental studies, an analysis of the minimum principal stress distributions in the beams showed that a truss mechanism, made up of struts, was formed regardless of the amount and configuration of reinforcement. However, it was observed that the struts in double-span beams were more prominently developed in the interior spans as compared to the exterior spans. This finding suggests that in two-span deep beams, the inner spans are more critical than the outer spans and should be reinforced with more shear reinforcement.
- The minimum principal stresses in the diagonal compression struts along the shear span did not exceed the concrete's compressive strength, yet stress concentrations are found near the strut ends at the top and bottom surfaces of the beam, aligns with experimental findings. This highlights the importance of these areas, as crushing in concrete is typically observed in these regions of the struts.
- The numerical analyses results showed that the longitudinal reinforcement in the beams does not contribute to the beam strength, while an increase in the amount of shear reinforcement does enhance beam strength. This outcome of the numerical models is consistent with experimental findings.
- When examining the axial force demands on the shear reinforcement for different concrete models, yielding in the reinforcements is observed most prominently in the Mat072R3 model, followed by the Mat084/85 model, and finally, the Mat159 material. It has been observed that the yielding of shear reinforcements occurred within the dimensions of the diagonal compression struts observed in the principal stresses of concrete. Outside these dimensions, the shear reinforcements remained elastic. This finding is important as it indicates the localized nature of yielding in shear reinforcements and highlights the significance of the diagonal compression struts in the structural behavior of reinforced concrete beams.
- When analyzing the axial force demands on the bottom longitudinal reinforcements of beams for different concrete models, it was found that these demands are consistent with experimental observations. Upon examining the axial force demands on the bottom longitudinal reinforcements of single-span beams for various concrete models, it was noted that the reinforcement yielded in the models using Mat159 and Mat072R3. In contrast, the reinforcement remained elastic in the models utilizing Mat084/085 and Mat016. In the case of double-span beams, however, reinforcement yielding was observed in all the material models used.
- The study's primary objective—predicting the strength values of reinforced concrete deep beams—was comprehensively addressed through detailed analyses and validations. The comparison of numerical results with experimental data demonstrates the effectiveness of the proposed methodology in accu-

rately estimating shear strength values. Mat159 emerged as the most reliable concrete model for strength prediction, achieving close alignment with experimental measurements across all beam types. This accuracy highlights the method's potential as a robust tool for predicting beam capacities.

- The methodology employed in this study can be readily adapted for beams with different geometries, materials, or loading conditions by recalibrating material models and boundary conditions. This flexibility enhances the applicability of the findings, saving time for researchers and practitioners alike. Furthermore, disseminating these results to the broader research community enables critical evaluation and comparison, fostering the refinement of existing methods.

By employing LS-DYNA's default concrete parameter options, this study established a cost-effective, reliable method for deep beam capacity estimation, reducing the need for extensive experimental testing. This approach facilitates the exploration of deep beams with various configurations without significant experimental investments.

Acknowledgements

The research presented in this article is an expansion of the work originally conducted in the M.Sc. thesis of Gökhan Karaman.

Funding

The authors received no financial support for the research, authorship, and/or publication of this manuscript.

Conflict of Interest

The authors declared no potential conflicts of interest with respect to the research, authorship, and/or publication of this manuscript.

Author Contributions

All of the authors made substantial contributions to conception and design, or acquisition of data, or analysis and interpretation of data; were involved in drafting the manuscript or revising it critically for important intellectual content; and gave final approval of the version to be published.

Data Availability

The datasets created and/or analyzed during the current study are not publicly available, but are available from the corresponding author upon reasonable request.

REFERENCES

ACI 318-19 (2019). Building code requirements for structural concrete. American Concrete Institute, Farmington Hills, MI.

ACI 318-83 (1983). Building code requirements for reinforced concrete. American Concrete Institute, Detroit, MI.

Arabzadeh A (2020). Analysis of boundary condition effects on RC deep beams. *Structures*, 23, 821-830.

ASCE-ACI Committee 445 on Shear and Torsion (1998). Recent approaches to shear design of structural concrete. *Journal of Structural Engineering*, 124(12), 1375-1417.

Broadhouse B (1995). The Winfrith concrete model in LS-DYNA3D. *Report: SPD/D (95)*, 363.

Broadhouse B, Neilson A (1987). Modelling reinforced concrete structures in DYNA3D. Safety and Engineering Science Division, UKAEA Atomic Energy Establishment, Winfrith, UK.

CSA A23.3 (2004). Design of concrete structures. Canadian Standard Association, Mississauga, ON.

Chen H, Yi W-J, Ma ZJ (2020). Shear-transfer mechanisms and strength modeling of RC continuous deep beams. *Journal of Structural Engineering*, 146(11), 04020240.

Chen H, Yi W-J, Ma ZJ, Hwang H-J (2019). Shear Strength of Reinforced Concrete Simple and Continuous Deep Beams. *ACI Structural Journal*, 116(6), 31-40.

Collins MP, Bentz EC, Sherwood EG (2008). Where is shear reinforcement required? Review of research results and design procedures. *Structural Journal*, 105(5), 590-600.

Gedik YH, Nakamura H, Yamamoto Y, Ueda N, Kunieda M (2012). Effect of stirrups on the shear failure mechanism of deep beams. *Journal of Advanced Concrete Technology*, 10(1), 14-30.

Grassl P, Johansson M, Leppänen J (2018). On the numerical modelling of bond for the failure analysis of reinforced concrete. *Engineering Fracture Mechanics*, 189, 13-26.

Imani R, Mosqueda G, Bruneau M (2015). Experimental study on post-earthquake fire resistance of ductile concrete-filled double-skin tube columns. *Journal of Structural Engineering*, 141(8), 04014192.

Jiang H, Zhao J (2015). Calibration of the continuous surface cap model for concrete. *Finite Elements in Analysis and Design*, 97, 1-19.

Li Z, Liu X, Kou D, Hu Y, Zhang Q, Yuan Q (2023). Probabilistic models for the shear strength of RC deep beams. *Applied Sciences*, 13(8), 4853.

LS-DYNA version R10.0 (2017). Livermore Software Technology Corporation, Livermore, CA.

LSTC (2017). LS-DYNA Keyword User's Manual, Volume II, Material Models. Livermore Software Technology Corporation, Livermore, CA.

Ma C, Wang S, Zhao J, Xiao X, Xie C, Feng X (2023). Prediction of shear strength of RC deep beams based on interpretable machine learning. *Construction and Building Materials*, 387, 131640.

Markovich N, Kochavi E, Ben-Dor G (2011). An improved calibration of the concrete damage model. *Finite Elements in Analysis and Design*, 47(11), 1280-1290.

Marti P (1985). Basic tools of reinforced concrete beam design. *Journal Proceedings*, 82(1), 46-56.

Murray YD, Abu-Odeh AY, Bligh RP (2007). Evaluation of LS-DYNA concrete material model 159. Office of Research, Development, and Technology, Federal Highway Administration, United States.

Novozhilov YV, Dmitriev AN, Mikhaluk DS (2022). Precise calibration of the continuous surface cap model for concrete simulation. *Buildings*, 12(5), 636.

Polat E (2020a). Investigation of concrete filled composite plate shear walls using finite element methods. *Uludağ University Journal of the Faculty of Engineering*, 25(1), 139-152.

Polat E (2020b). Investigation of influence of concrete material models on cyclic inelastic response of a concrete filled composite plate shear wall. *Challenge Journal of Structural Mechanics*, 6(2), 91-98.

Polat E (2022a). Theoretical Models for Tie Bar Maximum Axial Force Demand in Composite Plate Shear Walls–Concrete Filled. *International Journal of Steel Structures*, 22(4), 1108-1125.

Polat E (2022b). Boundary plate influence on tie bars axial force demands in composite plate shear walls–concrete filled. *Challenge Journal of Structural Mechanics*, 8(4), 166-172.

Polat E, Bruneau M (2017). Modeling cyclic inelastic in-plane flexural behavior of concrete filled sandwich steel panel walls. *Engineering Structures*, 148, 63-80.

Polat E, Bruneau M (2018). Cyclic inelastic in-plane flexural behavior of concrete filled sandwich steel panel walls with different cross-section properties. *Engineering Journal, American Institute of Steel Construction*, 55, 45-76.

Polat E, Kenarangi H, Bruneau M (2021). Investigation of tie bars axial force demands in composite plate shear walls—concrete filled. *International Journal of Steel Structures*, 21, 901-921.

Polat E, Polat EG (2024). Predicting and optimizing maximum flexural strength of planar composite plate shear walls – concrete filled with the application of LR and RSM. *Structures*, 69, 107353.

Rogowsky D, McGregor J, Ong S (1986). Tests of reinforced concrete deep beams. *Journal of the American Concrete Institute*, 83(4), 614-623.

Schlaich J, Schäfer K, Jennewein M (1987). Toward a consistent design of structural concrete. *PCI Journal*, 32(3), 74-150.

Tang R-Y, Sun Y-L, Wang Y-G, Ding R, Fan J-S, Nie J-G (2024). Finite element analysis of single steel-plate concrete composite containment of nuclear power plant under commercial aircraft impact. *Engineering Structures*, 321, 118998.

Tay SK, Poon JK, Chan R (2016). Modeling rebar in reinforced concrete for ALE simulations. *14th International LS-DYNA Users Conference,* Detroit, MI, 1-14.

Winkelbauer BJ (2015). Phase I Evaluation of Selected Concrete Material Models in LS-DYNA. *M.Sc. thesis*, University of Nebraska-Lincoln, Lincoln, NE.

Wittmann F, Rokugo K, Brühwiler E, Mihashi H, Simonin P (1988). Fracture energy and strain softening of concrete as determined by means of compact tension specimens. *Materials and Structures*, 21(1), 21-32.

Wu Y, Crawford JE, Magallanes JM (2012). Performance of LS-DYNA concrete constitutive models. *12th International LS-DYNA Users Conference,* Dearborn, MI, 3-5.

Wu Y, Crawford JE (2015). Numerical modeling of concrete using a partially associative plasticity model. *Journal of Engineering Mechanics*, 141(12), 04015051.

Youssf O, ElGawady MA, Mills JE (2015). Displacement and plastic hinge length of FRP-confined circular reinforced concrete columns. *Engineering Structures*, 101, 465-476.

Zargarian M, Rahai A (2022). An experimental and numerical study on continuous RC deep beams strengthened with CFRP strips. *International Journal of Civil Engineering*, 20(6), 619-637.

Zhao M-Z, Lehman DE, Roeder CW (2021). Modeling recommendations for RC and CFST sections in LS-DYNA including bond slip. *Engineering Structures*, 229, 111612.

Challenge Journal of Structural Mechanics

Research Article

Investigating the effects of glass fiber in enhancing concrete pavement performance

Fatih İrfan Baş [a,*]

[a] *Department of Civil Engineering, Erzincan Binali Yıldırım University, 24002 Erzincan, Türkiye*

ABSTRACT

Flexible pavements are considered more sustainable than concrete pavements primarily due to the higher long-term maintenance and rehabilitation costs associated with concrete pavements. Concrete pavements possess a higher modulus of elasticity, which allows them to distribute vehicle loads over a larger area, thereby enhancing the strength of the pavement. However, despite this advantage, their flexural strength is relatively low. As a result, there has been a growing focus on research to improve the flexural strength of concrete pavements to increase their overall performance and sustainability. This study aimed to reveal the effects of enhanced mechanical properties of concrete reinforced with glass fiber on concrete pavements, specifically under heavy vehicle loading as in real-world conditions. The impact of glass fiber on the thickness of both the concrete and base layers, as well as the quality of the base layer material and transverse joint spacing, was assessed. For this purpose, 3D finite element models were developed using ANSYS software, considering concrete thicknesses of 100, 150, and 200 mm, glass fiber ratios of 0%, 0.5%, and 1%, base layer elastic moduli of 100, 200, and 300 MPa, and transverse joint spacings of 300, 450, and 600 mm. It was determined that the concrete thickness and the base layer modulus of elasticity were the most influential factors in minimizing flexural stress, total deformation, and equivalent total strain. The glass fiber addition had a more notable impact on maximum principal stress, especially at the 1% ratio, but had a minimal effect on total deformation and strain. Transverse joint spacing had the least effect, although shorter spacings are still recommended to reduce the risk of transverse cracking in stiffer base layers.

ARTICLE INFO

Article history:
Received – November 18, 2024
Revision requested – December 16, 2024
Revision received – December 23, 2024
Accepted – January 4, 2025

Keywords:
glass fiber
concrete pavement
cast iron model
Taguchi method
finite element model

Citation: Baş Fİ (2025). Investigating the effects of glass fiber in enhancing concrete pavement performance. *Challenge Journal of Structural Mechanics*, 11(1), 42–54.

1. Introduction

Flexible pavements have a lower initial cost; however, when long-term maintenance costs are considered, they are more expensive than concrete pavements (Nazki et al. 2020; Araz et al. 2023). In Türkiye, 92% of the 2024 transportation maintenance budget is allocated primarily for flexible pavements (KGM 2024). Therefore, expanding the use of concrete pavement applications in both Türkiye and globally is essential at the earliest opportunity. Concrete pavements have a higher elasticity modulus and stiffness than flexible pavements, enabling them to spread traffic loads over a wider area on the ground, which enhances their strength. They function similarly to beams resting on an elastic foundation (Ağar et al. 1998). Plain concrete, however, is a brittle material, and its flexural strength decreases as its strength class increases (Zain et al. 2002). Flexural strength measures a material's resistance to bending stresses, indicating the stress level at which it fails in bending (Ntimugura et al. 2020). For concrete, flexural strength typically ranges from 10% to 20% of its compressive strength (Kosmatka et al. 2003).

* *Corresponding author*. Tel.: +90-446-224-0088 ; E-mail address: fibas@erzincan.edu.tr (F. İ. Baş)
ISSN: 2149-8024 / DOI: https://doi.org/10.20528/cjsmec.2025.01.004

Studies aimed at enhancing flexural strength have led to a rapid increase in the use of various additives and fibers (steel, basalt, glass, polymeric, carbon) in plain concrete, as reflected in the literature (Çelik et al. 2024). The utilization of fibers improves the service life and mechanical properties of concrete (Karahan and Atiş 2011; Zhang and Li 2013; Şengel et al. 2022; Gultekin 2023; Eryılmaz Yıldırım et al. 2024). Glass fibers are the most commonly used synthetic fibers to enhance the flexural strength of concrete, a critical parameter for concrete pavements under cyclic loading, owing to their availability and ease of application (Akram et al. 2024).

Jagannadha and Ahmed (2009) revealed that incorporating just 0.03% glass fiber into plain concrete resulted in greater flexural and compressive strengths compared to both 0.1% glass fiber and plain concrete. Kizilkanat et al. (2015) conducted a study using glass fiber and basalt fiber and reported that splitting tensile strength improved with increasing basalt fiber ratios; however, no further increase was observed beyond a 0.5% glass fiber ratio. Afroz et al. (2019) demonstrated that a 1% addition of steel fiber increased flexural and compressive strengths by 80% and 10%, respectively. Ali and Qureshi (2019) observed that adding 0.25% to 1.0% glass fiber to concrete enhanced its flexural strength by 25%. Lau et al. (2020) found that fiber addition increased fatigue cycles in concrete pavements by 135%. Hussain et al. (2020) concluded that a 1% addition of steel fiber reduced pavement thickness by 34%. Tunçel et al. (2020) reported that 0.5% Kevlar fiber improved the flexural strength of concrete pavements. Abdulridha et al. (2021) investigated the effects of varying cement content, steel and polypropylene fiber ratios, and silica fume ratios, concluding that cement content had the greatest impact on reducing shrinkage cracking. Sharbatdar and Rahmati (2022) reported that adding 20 kg of steel fibers per m^3 increased flexural and tensile strengths by 83% and 20%, respectively. Bhogone and Subramaniam (2022) observed that hybrid use of polypropylene and steel fibers reduced plastic shrinkage cracking by 90%. Mola et al. (2024) studied Kevlar fiber's effect on concrete pavements, finding that it enhanced flexural and compressive strengths by 15% and 5%, respectively.

In recent years, there has been a growing focus on the numerical modeling of fiber-reinforced concrete. The finite element method offers a numerical approach for addressing issues involving complex structures, varying loads, and diverse materials.

Kumara et al. (2003) developed a finite element model to examine flexural stresses in ultra-thin pavements, observing that Florida pavement test sections in poor condition generated higher flexural stresses beneath the concrete layer. Sultana (2010) developed a finite element model using SolidWorks software to analyze the bonding conditions between whitetopping concrete and flexible pavements. The findings indicated that bond conditions were the most critical factor influencing pavement performance, with increased concrete layer thickness resulting in reduced flexural stress beneath the concrete layer. Çelik (2014) reported that, in a finite element model subjected to tandem axle dual tire loading, flexible pavements exhibited vertical stress levels 119% higher than those in concrete pavements. Additionally, Baş et al. (2022) developed a 3D finite element model to investigate flexural stresses in concrete pavements constructed on deteriorated flexible bases, concluding that concrete thickness was the most influential parameter in controlling bending stresses under the concrete layer.

In addition to the purchase costs of fibers used to enhance flexural strength, their impact on reducing workability, requiring the use of plasticizers, adds significant costs to the overall pavement design. Therefore, to make the use of fiber in concrete pavements more feasible, it is essential to reduce the thickness of the concrete layer, as well as the thickness and rigidity (quality) of the base layer. Besides, standard beam flexural strength tests often cannot be reliably used to estimate concrete pavement performance (Roesler et al. 2004).

This study aimed to investigate the effects of enhanced mechanical properties of concrete reinforced with glass fiber on the performance of concrete pavements under heavy vehicle loading, reflecting real-world conditions. The influence of glass fiber on the thickness of both the concrete and base layers, as well as the quality of the base layer material, was evaluated. Nonlinear finite element analysis was performed using ANSYS (SAS 2024) software with a cast iron material model. Finite element models were developed based on the Taguchi experimental design method, incorporating parameters such as concrete thicknesses of 100, 150, and 200 mm, glass fiber ratios of 0%, 0.5%, and 1%, base layer elastic moduli of 100, 200, and 300 MPa, and transverse joint spacings of 300, 450, and 600 mm.

2. Materials and Method

When complex problems cannot be solved directly, the main problem can be divided into smaller and more manageable sub-problems called finite elements. The solution to the original problem can then be obtained from the solutions to these sub-problems. In this process, a sufficient model can be obtained using a well-defined finite number of elements (Moaveni 2011). Cheung and Zinkiewicz (1965) were the first to apply finite element analysis for pavement analysis.

2.1. Finite element modeling

Ali et al. (2020) conducted an in-depth study on the effects of adding glass fiber to pavement concrete, examining its mechanical properties at fiber ratios of 0%, 0.5%, and 1%. They evaluated compressive strength and elastic modulus in accordance with ASTM-C39 (2015). Additionally, flexural strength was assessed using a four-point loading test on 100 x 100 x 350 mm specimens, following ASTM-C78 (2018). In this study, the findings of Ali et al. (2020) were applied to evaluate the effects of glass fiber on concrete pavement via finite element modeling. The load-deflection curve from the bending test is shown in Fig. 1, and Table 1 summarizes the mechanical properties of both plain and glass fiber reinforced concrete.

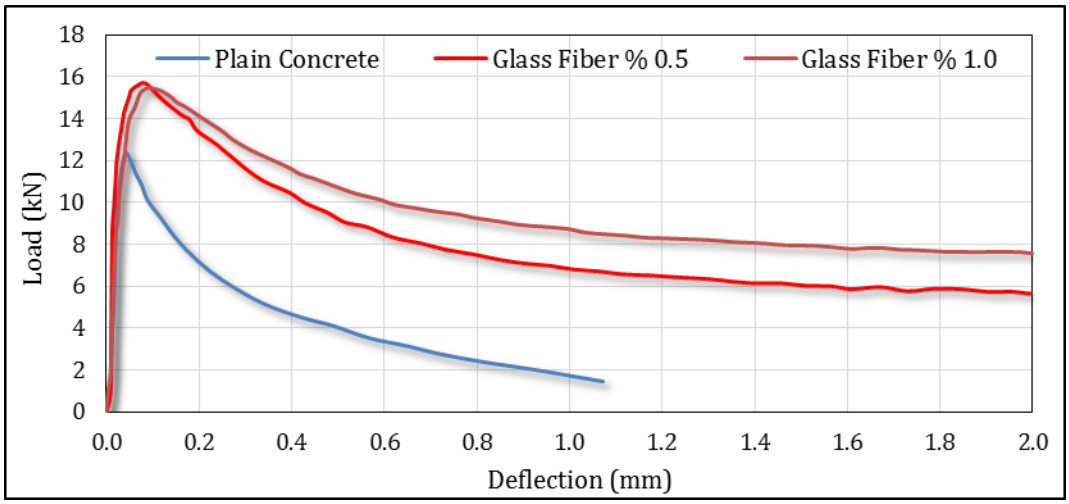

Fig. 1. Load deflection data of plain concrete and glass fiber reinforced concretes.

Table 1. Mechanical properties of plain and glass fiber reinforced concretes.

Type	Compressive strength (MPa)	Elastic modulus (MPa)	Flexural strength (MPa)
Plain concrete	34.66	23472	3.79
Glass fiber % 0.5	36.87	24583	4.75
Glass fiber % 1.0	35.57	23842	4.68

The Cast Iron plasticity model was utilized to capture the non-linear behavior of glass fiber-reinforced concrete, incorporating compressive and tensile stress-strain test data (Nguyen Dinh 2016; Jawdhari and Fam 2020; Noorvand et al. 2022). As the load-deflection data for compression tests were not provided in the study and only compression yield strengths were available, load-deflection curves were generated based on these yield strengths. This model presumes identical elastic behavior in both tension and compression; therefore, the division of stress by strain in the initial rows of compression and flexural tests was idealized to be the same, ensuring consistent results. Table 2 summarizes the stress–strain input values for the flexural response used in the Cast Iron plasticity model for both plain and glass fiber-reinforced concretes, based on experimental data.

Table 2. Flexural response input parameters for finite element analysis.

Plain concrete		Glass fiber % 0.5		Glass fiber % 1.0	
Strain (mm/mm)	Stress (MPa)	Strain (mm/mm)	Stress (MPa)	Strain (mm/mm)	Stress (MPa)
0.00010	2.35	0.00010	2.46	0.00005	1.19
0.00024	3.03	0.00024	3.64	0.00021	2.48
0.00043	3.79	0.00034	4.09	0.00029	3.08
		0.00039	4.29	0.00036	3.49
		0.00055	4.60	0.00046	4.04
		0.00085	4.75	0.00072	4.53
				0.00078	4.60
				0.00094	4.68

Axle weight studies conducted on 14,488 vehicles across 79 locations in Türkiye show that the most common truck type, representing 32% of the sample, has a 1.22 axle configuration (KGM 2023). For finite element analysis, heavy vehicles with this axle type were selected to reflect real-world loading conditions accurately. The wheelbases for 1.22-axle trucks range from 3.33 m to 6.69 m, depending on the vehicle brand in Türkiye; the shortest wheelbase, 3.3 m, was chosen to simulate a critical loading scenario.

Tire pressure for heavy vehicles generally varies from 500 to 1000 kPa worldwide, with 700 to 800 kPa recommended for pavement design (Moffatt 2017). Korkiala-Tanttu (2009) conducted extensive laboratory and ac-

celerated road tests, finding that the tire contact areas measured 250 mm by 225 mm for single tires and 225 mm by 200 mm for dual tires. In this study, a tire pressure of 700 kPa was applied, with contact areas of 250 mm by 225 mm for the front wheels and 225 mm by 200 mm for the rear wheels. A sample loading model for a pavement section with a 4.5-meter transverse joint spacing is illustrated in Fig. 2.

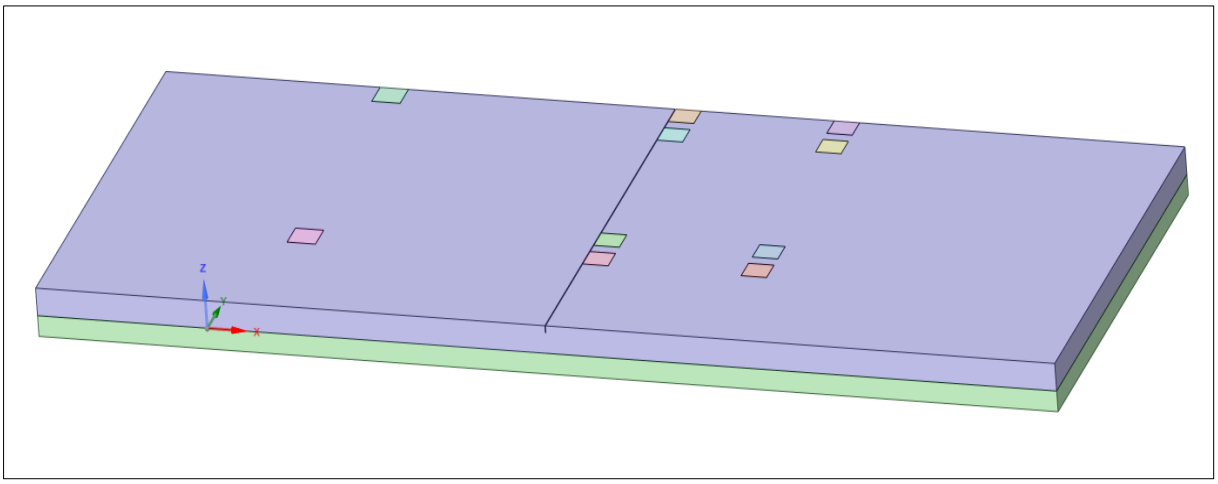

Fig. 2. Loading model of the pavement section with a 4.5-meter transverse joint spacing.

The finite element model consisted of a glass fiber-reinforced concrete pavement layer and a base layer arranged from top to bottom. The contact surface between the concrete pavement and the base layer was modeled as bonded. The base layer bottom was constrained in all directions, and the subgrade was excluded to improve the displacement analysis. Symmetry conditions were applied to the left side of the model, and the end faces along the y-axis were constrained in the x-axis to model the transverse joints. The right side of the model was not subjected to any constraints.

The element type SOLID185 was chosen for the base layer to represent the granular material. The modulus of elasticity was set at 100 MPa, 200 MPa, and 300 MPa, based on the AASHTO recommended range of 103 to 310 MPa. Poisson's ratio was set to 0.3. The base layer thickness was taken as 150 mm, the minimum thickness recommended by AASHTO.

ACPA (1992) and ACI 302.1R-11 (2011) recommend that joint spacing should be between 24 and 30 times the pavement thickness. Accordingly, the spacings for pavement thicknesses of 100 mm, 150 mm, and 200 mm were adjusted to 300 cm, 450 cm, and 600 cm, respectively, with the recommended upper limit. KGM (2016) recommends a joint width of 4.8 mm ± 1.5 mm and a minimum joint depth of one-fourth the concrete thickness. In this study, the joint width was considered to be 6 mm, and the depth was taken as one-fourth of the slab thickness.

2.2. Taguchi method

Finite element analyses were carried out using the Taguchi Method, which employs orthogonal arrays to minimize the number of experiments needed while maintaining the reliable confidence intervals (Mohammed and Najim 2020). In this approach, the S/N (Signal-to-Noise) ratio serves as a performance metric, where the signal represents the desired effect, and the noise reflects factors that adversely affect. Taguchi method addresses complex optimization problems through three solution targets: maximizing, minimizing, and achieving nominal values (Sünbül and Tortum 2024). Overall, this optimization process offers an effective and systematic approach, ensuring the production of high-performance, quality-enhanced products (Çolak et al. 2023).

The four parameters and their three levels, used for finite element analyses and optimization, are presented in Table 3. An L9 orthogonal array was selected for the experimental plan, with a 95% confidence interval applied; the details are provided in Table 4.

Table 3. Parameters and levels used in finite element analyses.

Parameters	Levels		
	1	2	3
Thickness (mm)	100	150	200
Glass fiber (%)	0.00	0.50	1.00
Modulus of elasticity of base layer (MPa)	100	200	300
Transverse joint space (mm)	300	450	600

Table 4. Experimental plan for finite element analysis.

Experiment No.	Thickness (mm)	Glass fiber (%)	Modulus of elasticity of base layer (MPa)	Joint space (mm)
1	100	0.00	100.00	300
2	100	0.50	200.00	450
3	100	1.00	300.00	600
4	150	0.00	200.00	600
5	150	0.50	300.00	300
6	150	1.00	100.00	450
7	200	0.00	300.00	450
8	200	0.50	100.00	600
9	200	1.00	200.00	300

3. Results and Discussion

3.1. Validation of the established FEM models

To validate the established models using compression and flexural test data on a concrete slab, Experiment 5 was selected. The model analysis results of the compression test for equivalent stress and equivalent total strain are shown in Fig. 3, with maximum equivalent stress and maximum equivalent total strain values of 36.87 MPa and 0.0022703 mm/mm, respectively.

The model analysis results of the flexural test for maximum principal stress and equivalent total strain are shown in Fig. 4, with maximum principal stress and maximum equivalent total strain values of 4.6791 MPa and 0.001834 mm/mm, respectively.

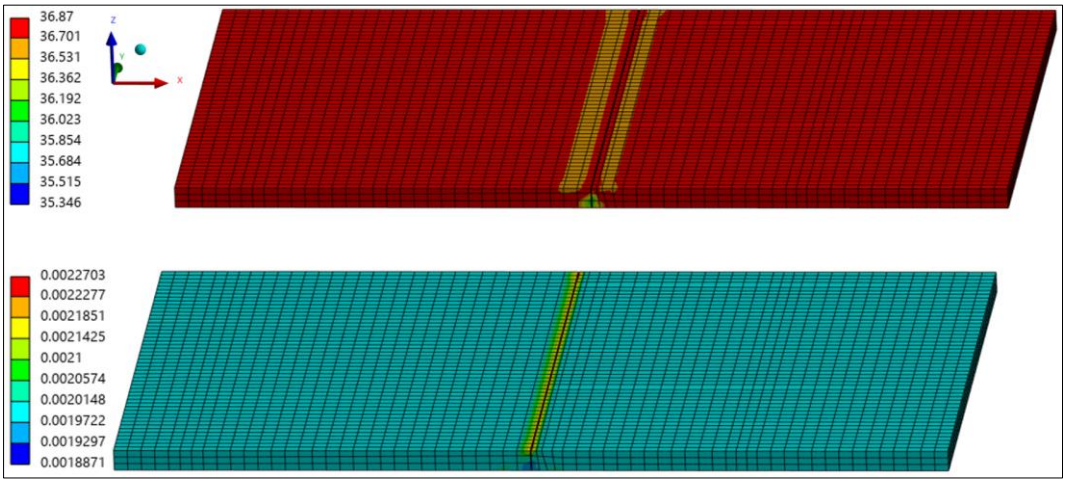

Fig. 3. Validation of compression test on a concrete slab for Experiment 5: Equivalent stress and equivalent total strain.

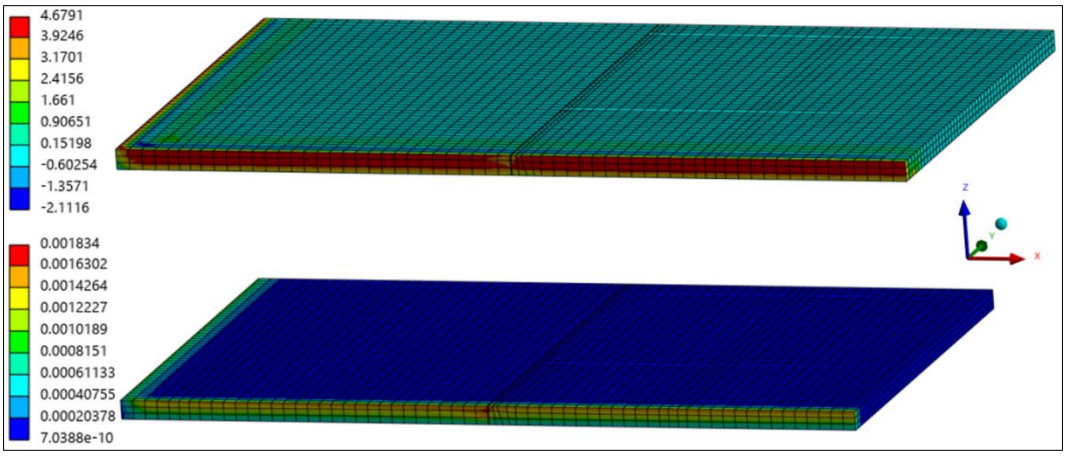

Fig. 4. Validation of flexural test on a concrete slab for Experiment 5: Maximum principal stress and equivalent total strain.

Fig. 5 presents the comparison between finite element analysis results and test data for compression and flexural tests. A reasonable agreement was observed, confirming the suitability of the selected constitutive iron cast model for simulating the real behavior of glass fiber-reinforced concrete.

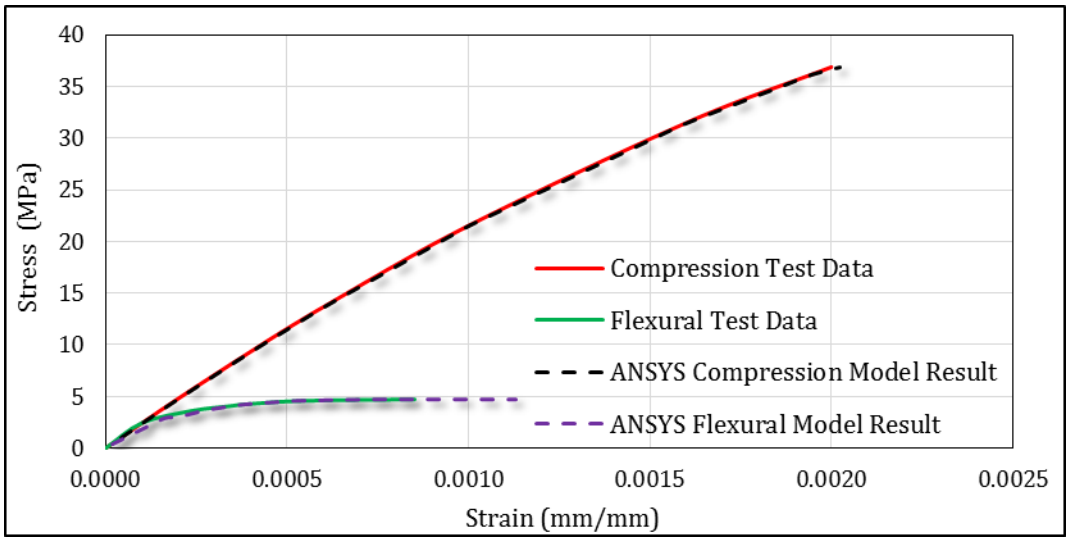

Fig. 5. Comparison of finite element results with compression and flexural tests.

3.2. Maximum principal stress analysis results

Maximum principal stress results used to evaluate the flexural stress arising at the bottom of the glass fiber-reinforced concrete layer are presented in Fig. 6.

As shown in Table 5, an ANOVA (Analysis of Variance) test was conducted to determine whether the S/N values of finite element results are statistically significant and to enable estimations with a 95% confidence interval. This study's error degree of freedom is zero, as all four parameters have three levels. To increase the error degree of freedom and enable estimations at a %95 confidence level, the transverse joint spacing parameter, with the smallest contribution at 0.28%, was pooled. The model demonstrated a high level of accuracy, with an R^2 of 0.9972 and a predicted R^2 of 0.9434, both in close agreement with the adjusted R^2 of 0.9888 (difference < 0.2). Additionally, the adequate precision, an indicator of signal-to-noise ratio, was 30.97, well above the threshold of 4, confirming the model's suitability for navigating the design space.

At a 95% confidence level, the F-values for the remaining parameters (concrete thickness, glass fiber ratio, and modulus of elasticity of the base layer) were higher than the F-table value of 19 for (2;2). Additionally, the model is statistically significant, as all unpooled parameters have p-values below 0.05.

The S/N contributions of all parameters are given in Table 6. The optimum levels were identified as A3, B3, C3, and D3. As shown in the experiment plan in Table 4, no experiment includes the optimum levels.

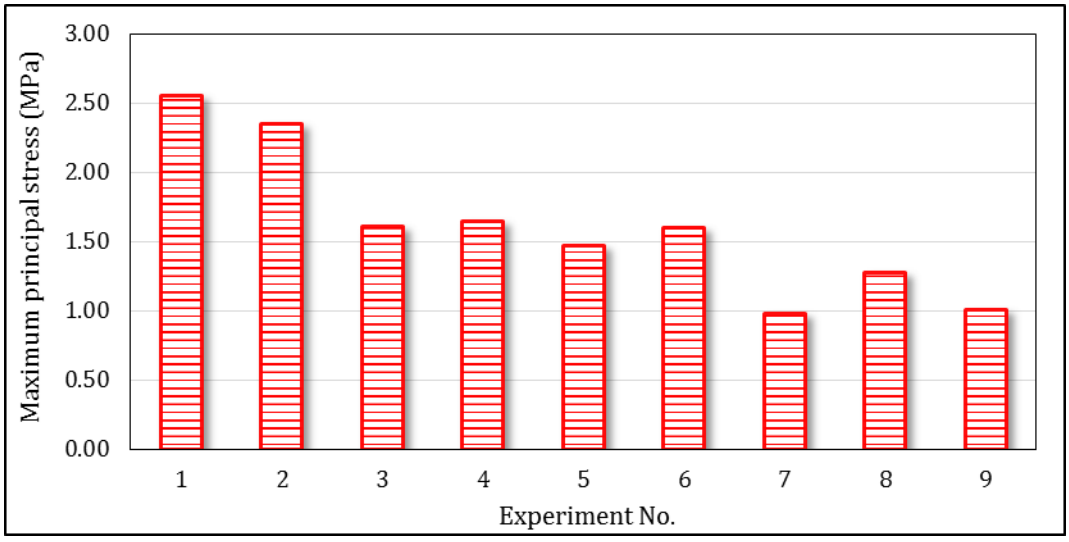

Fig. 6. Maximum principal stress results according to the experimental plan.

Table 5. Taguchi ANOVA table for maximum principal stress results.

Parameters	df	Sums of squares	Variance	F-value	Contribution (%)	p-value
Thickness (mm)	2	52.41	26.20	287.65	80.43	0.003
Glass fiber (%)	2	4.11	2.05	22.55	6.31	0.042
Modulus of elasticity of base layer (MPa)	2	8.46	4.23	46.45	12.99	0.021
Joint space (mm)			Pooled			
Error	2	0.18	0.09		0.28	
Total	8	65.16			100	

Table 6. S/N contributions of all parameters.

Parameters	Optimum levels	S/N contribution
Thickness (mm)	3	3.052
Glass fiber (%)	3	0.949
Modulus of elasticity of base layer (MPa)	3	1.284
Joint space (mm)	3	0.000
The sum of contributions (S/N)		5.285
Average performance statistics (S/N)		-3.716
Optimum predicted result (S/N) / (MPa)		1.569 / 0.835
Validation result (S/N) / (MPa)		0.141 / 0.98393
Confidence interval (α=95%) (S/N)		- 0.162 - 3.301

A validation finite element model was created using the optimum levels: 200 mm concrete thickness, 1% glass fiber ratio, 300 MPa modulus of elasticity of the base layer, and 600 mm joint spacing. The maximum principal stress in the validation finite element model was observed to be 0.98393 MPa, located at the bottom of the concrete layer at the transverse joint, as shown in Fig. 7. This value falls within the range of 0.684 to 1.018 MPa, indicating that the result is accurate within a 95% confidence interval.

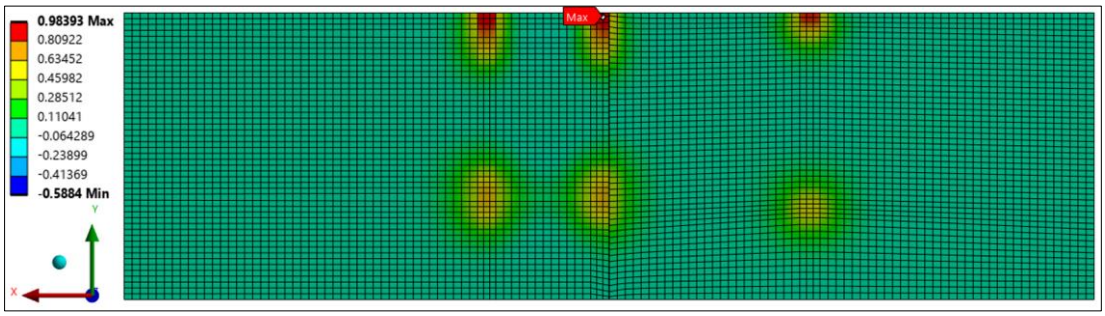

Fig. 7. Maximum principal stress at the bottom of the concrete slab for validation model.

Performance statistics for minimizing maximum principal stress values are shown in Fig. 8. The signal-to-noise (S/N) contribution of the concrete slab thickness was found to be the most effective parameter in minimizing flexural stress at the bottom of the concrete layer, with a value of 3.052. This was followed by the modulus of elasticity of the base layer, glass fiber ratio, and joint spacing, with respective values of 1.284, 0.949, and 0.194.

As the concrete thickness increased, the maximum principal stress at the bottom of the slab decreased significantly, consistent with previous studies (Sultana 2010; Baş et al. 2022). This is attributed to the higher load transfer efficiency of the thicker plates, particularly at the joints (Sii 2015). The 0.5% glass fiber ratio had a similar effect on maximum principal stress as plain concrete (showing no significant impact), while the 1.0% glass fiber ratio reduced the maximum principal stress. The theoretical critical fiber volume, the amount of fiber needed to significantly impact the concrete's strength, is between 1% and 3% (Bentur and Mindess 2006). Since the 0.5% fiber ratio was below this threshold, it had a similar effect to the plain concrete. The 1.0% ratio's effectiveness is attributed to the strong bond between the

fibers and the concrete matrix, causing the fibers to fracture before debonding (Roesler et al. 2019). The maximum principal stress decreased as the modulus of elasticity of the base layer increased, aligning with previous studies conducted on concrete slabs (Wu et al. 1993; Kim 2017). The transverse joint spacing had the least effect on maximum principal stress; however, it is important to note that increasing the transverse joint spacing may lead to more cracking in the concrete slab (Shoukry et al. 2007; Roesler et al. 2019).

3.3. Total deformation analysis results

Total deformation results obtained from the finite element models on the glass fiber-reinforced concrete layer are presented in Fig. 9.

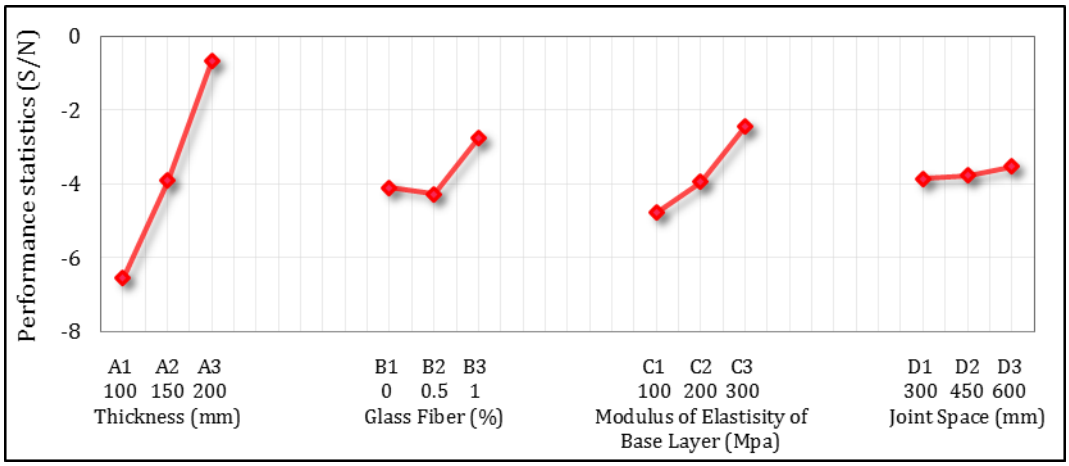

Fig. 8. Performance statistics minimizing maximum principal stress for all levels.

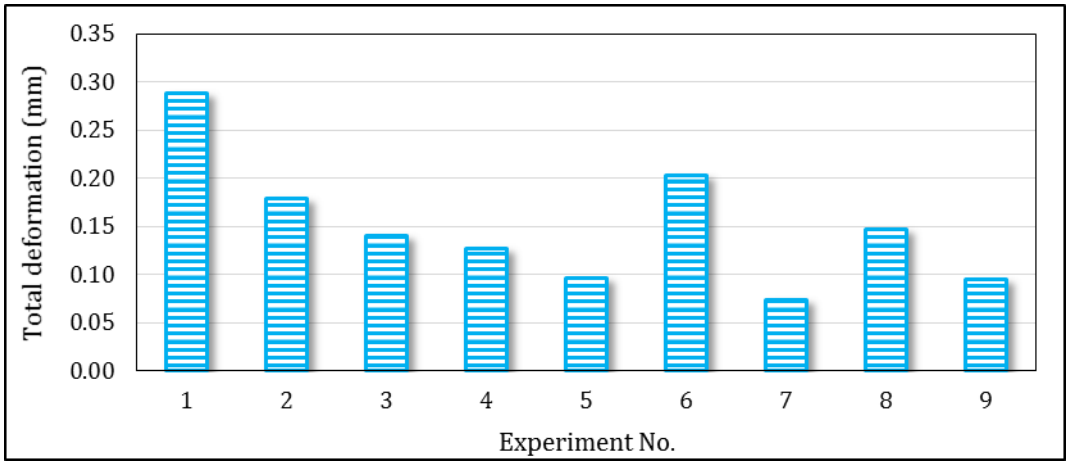

Fig. 9. Total deformation results according to the experimental plan.

As shown in Table 7, the Taguchi ANOVA table for total deformation results demonstrates a perfect model fit. With an R^2 of 0.9998, the model achieves error-free prediction accuracy by accounting for all variability in the total deformation results. Furthermore, the predicted R^2 of 0.9996 and adjusted R^2 of 0.9997 highlight the model's robustness and reliability, confirming its predictive power without the risk of overfitting.

Table 7. Taguchi ANOVA table for total deformation results.

Parameters	df	Sums of squares	Variance	F-value	Contribution (%)	p-value
Thickness (mm)	2	48.468	24.234	20,812	44.16	0.00005
Glass fiber (%)	2	0.056	0.028	24.096	0.05	0.03985
Modulus of elasticity of base layer (MPa)	2	61.242	30.621	26,297	55.79	0.00004
Joint space (mm)			Pooled			
Error	2	0.002	0.001			
Total	8	109.768			100	

The performance statistics for the total deformation results are shown in Fig. 10. The optimal levels for minimizing total deformation in the concrete layer were identified as A3, B2, C3, and D1. The base layer modulus of elasticity made the highest contribution to reducing total deformation, with a value of 55.79, followed by the concrete layer thickness at 44.16. Glass fiber had a minor contribution of 0.05, and transverse joint spacing, contributing only 0.002, was therefore pooled. As both the base layer modulus of elasticity and concrete thickness increased, total deformation decreased. The concrete layer became stiffer with the increased thickness, and this situation led to less deformation under the vehicle loads since it distributed the vehicle load more effectively through the pavement. The increase in the elasticity modulus of the base layer led to lower deformation, as it measures the layer's rigidity. The effect of the glass fiber ratio on deformation was minor compared to the thickness and the base layer's modulus of elasticity. Although the increase in elasticity modulus and flexural strength slightly improved the concrete material's stiffness, the impact was limited because the vehicle loading with a 1.22 axle type did not generate stresses at the edge and transverse joint high enough to exceed the tensile yield strength, keeping the material within the elastic region and preventing it from entering the plastic region. Transverse joint spacing had a minimal effect on deformation; however, it is important to note that shorter transverse joint spacings are necessary for stiffer base layers to reduce the risk of transverse cracking (Huang 2004).

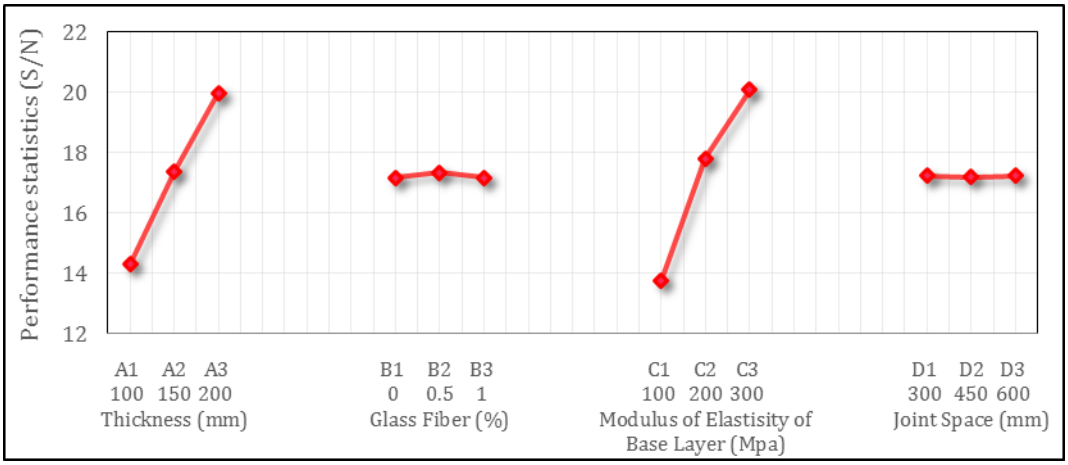

Fig. 10. Performance statistics minimizing total deformation for all levels.

The maximum total deformation observed in the finite element model for validating maximum principal stress optimization at levels A3, B3, C3, and D3 was 0.072384 mm, located at the transverse joint, as shown in Fig. 11. This value falls within the range of 0.0709894 to 0.0742625, confirming model accuracy within a 95% confidence interval.

3.4. Equivalent total strain analysis results

Equivalent total strain results obtained from the finite element models on the glass fiber-reinforced concrete layer and corresponding S/N values are presented in Table 8.

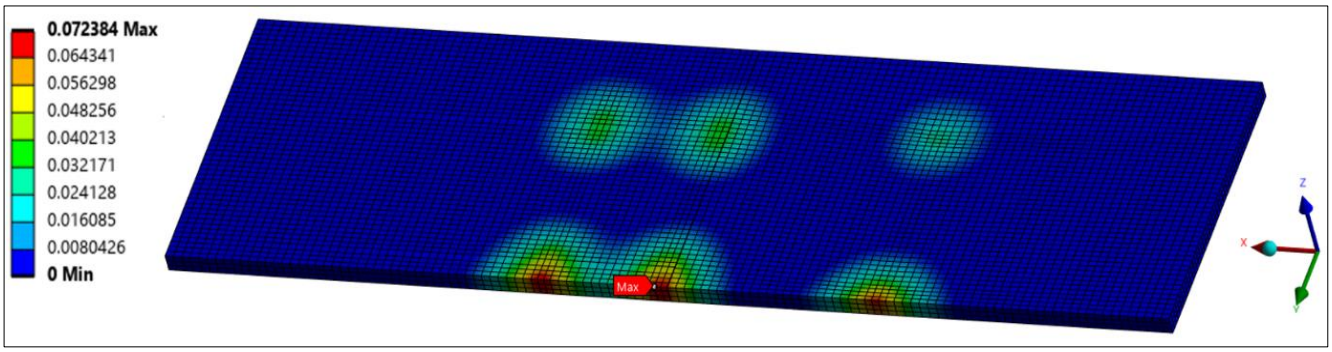

Fig. 11. Total deformation result at levels A3, B3, C3, and D3.

The ANOVA table for minimizing the maximum equivalent total strain results is given in Table 9. The close alignment between R^2 (0.9997), adjusted R^2 (0.9996) and predicted R^2 (0.9993) confirms that the model is well-fitted and robust without overfitting and bias. The high predicted R^2 value, close to 1.00, validates the model's estimation capability. Optimum levels that minimize the equivalent total strains were found as A3, B2, C3, and D3.

Table 8. Equivalent total strain results and corresponding S/N values.

Experiment No.	Equivalent total strain (mm/mm)	S/N
1	0.00188930	54.47
2	0.00112380	58.99
3	0.00086532	61.26
4	0.00081253	61.80
5	0.00060235	64.40
6	0.00131750	57.60
7	0.00046139	66.72
8	0.00096555	60.30
9	0.00060722	64.33

Table 9. Taguchi ANOVA table for equivalent total strain results.

Parameters	df	Sums of squares	Variance	F-value	Contribution (%)	p-value
Thickness (mm)	2	46.279	23.140	11,364	40.36%	0.00009
Glass fiber (%)	2	0.086	0.043	21.166	0.08%	0.04511
Modulus of elasticity of base layer (MPa)	2	68.301	34.151	16,771	59.56%	0.00006
Joint space (mm)			Pooled			
Error	2	0.004	0.002			
Total	8	114.671			100	

The modulus of elasticity of the base layer and concrete thickness had the greatest impact in minimizing the equivalent total strain, with values of 59.56 and 40.36, respectively. In contrast, the glass fiber ratio and joint spacing parameters had minimal effects, with values of 0.075 and 0.004. The equivalent total strain decreased as both the modulus of elasticity of the base layer and the thickness of the concrete layer increased.

The finite element model for validating maximum principal stress optimization at levels A3, B3, C3, and D3 showed a maximum equivalent total strain of 0.00045942 mm at the transverse joint, as illustrated in Fig. 12. This value lies within the range of 0.000444698 to 0.000472011, verifying model accuracy within a 95% confidence interval.

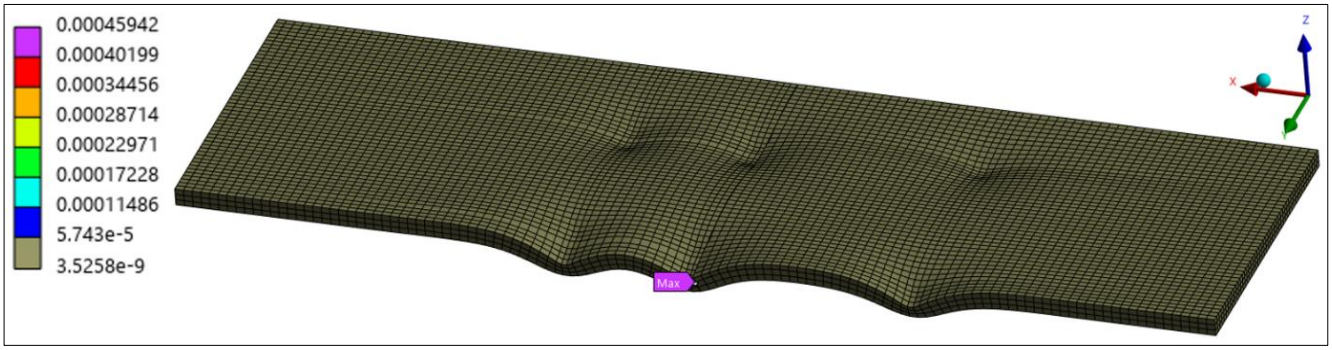

Fig. 12. Equivalent total strain result at levels A3, B3, C3, and D3 (0.5x Auto scaled).

The high predicted R^2 value for all three models validates the robustness of the model's predictive ability. The transverse joint spacing parameter was pooled for all three models, and predictions were made without this parameter, considering all remaining factors across all levels at a 95% confidence level, as summarized in Table 10.

4. Conclusions

This study evaluated the addition of glass fibers at 0%, 0.5%, and 1% to enhance the flexural strength of concrete pavements, examining the effects on maximum principal stress, total deformation, and equivalent total strain. The concrete pavements had thick-

nesses of 100, 150, and 200 mm, with base layer elastic moduli of 100, 200, and 300 MPa, and transverse joint spacings of 300, 450, and 600 mm. The findings are summarized below:

Table 10. Taguchi predictions for all parameters except transverse joint spacing.

Levels	Maximum principal stress (MPa)	Total deformation (mm)	Equivalent total strain (mm/mm)
A1-B1-C1	2.513	0.288	0.00188318
A1-B1-C2	2.283	0.181	0.00115498
A1-B1-C3	1.919	0.139	0.00087427
A1-B2-C1	2.568	0.283	0.00183341
A1-B2-C2	2.333	0.178	0.00112445
A1-B2-C3	1.961	0.137	0.00085117
A1-B3-C1	2.156	0.289	0.00186887
A1-B3-C2	1.959	0.181	0.00114620
A1-B3-C3	1.646	0.140	0.00086763
A2-B1-C1	1.853	0.202	0.00132836
A2-B1-C2	1.683	0.127	0.00081470
A2-B1-C3	1.415	0.098	0.00061670
A2-B2-C1	1.894	0.198	0.00129325
A2-B2-C2	1.720	0.125	0.00079317
A2-B2-C3	1.446	0.096	0.00060040
A2-B3-C1	1.590	0.202	0.00131827
A2-B3-C2	1.444	0.127	0.00080851
A2-B3-C3	1.214	0.098	0.00061201
A3-B1-C1	1.274	0.150	0.00099441
A3-B1-C2	1.157	0.094	0.00060988
A3-B1-C3	0.973	0.073	0.00046166
A3-B2-C1	1.302	0.147	0.00096813
A3-B2-C2	1.183	0.092	0.00059377
A3-B2-C3	0.994	0.071	0.00044946
A3-B3-C1	1.093	0.150	0.00098685
A3-B3-C2	0.993	0.094	0.00060525
A3-B3-C3	0.835	0.073	0.00045815

- The concrete thickness and the base layer modulus of elasticity were the most influential factors in minimizing stress, deformation, and strain, with greater thickness and stiffness resulting in improved pavement performance. The glass fiber addition had a more notable impact on maximum principal stress, especially at the 1% ratio, but had a minimal effect on total deformation and strain. Transverse joint spacing had the least effect, although shorter spacings are still recommended to reduce the risk of transverse cracking in stiffer base layers.
- Across all levels of glass fiber ratio and base layer elasticity modulus, concrete thicknesses of 100 mm and 150 mm produced maximum principal stresses approximately 1.97 and 1.45 times higher, respectively, than the thickness of 200 mm. These thicknesses also led to deformations and strains approximately 1.91 and 1.35 times higher, respectively, compared to the 200 mm thickness.
- Similarly, across all levels of glass fiber ratio and concrete thickness, base layer elasticity moduli of 100 MPa and 200 MPa generated maximum principal stresses about 1.31 and 1.19 times higher, respectively, than a modulus of 300 MPa. These moduli also resulted in deformations and strains approximately 2.11 and 1.31 times greater than those observed with a modulus of 300 MPa.
- Lastly, across all levels of concrete thickness and base layer elasticity modulus, glass fiber ratios of 0% and 0.5% produced maximum principal stresses approximately 1.18 times higher than a ratio of 1%. No effect of glass fiber ratio on deformation and strain was observed.

Acknowledgements
None declared.

Funding
The author received no financial support for the research, authorship, and/or publication of this manuscript.

Conflict of Interest
The author declared no potential conflicts of interest with respect to the research, authorship, and/or publication of this manuscript.

Data Availability
The datasets created and/or analyzed during the current study are not publicly available, but are available from the corresponding author upon reasonable request.

REFERENCES

Abdulridha MA, Salman MM, Banyhussan QS (2021). Effect polypropylene of fiber on drying shrinkage cracking of concrete pavement using response surface methodology. *Journal of Engineering Sustainable Development,* 25(3), 10-21.

ACI 302.1R-11 (2011). Guide to concrete floor and slab construction. American Concrete Institute, Farmington Hills, MI.

ACPA (1992). Design and construction of joints for concrete streets. American Concrete Pavement Association, Skokie, IL.

Afroz M, Venkatesan S, Patnaikuni I (2019). Effects of hybrid fibers on the development of high volume fly ash cement composite. *Construction and Building Materials,* 215, 984-997.

Ağar E, Sütaş İ, Öztaş G (1998). Beton Yollar: Rijit Yol Üstyapıları; Malzeme-Tasarım-Üretim-Yapım-Bakım Teknikler. İstanbul Technical University, İstanbul. (in Turkish)

Akram H, Hozayen HA, Abdelfatah A, Khodary F (2024). Fiber showdown: A comparative analysis of glass vs. polypropylene fibers in hot-mix asphalt fracture resistance. *Buildings,* 14(9), 2732.

Ali B, Qureshi LA (2019). Influence of glass fibers on mechanical and durability performance of concrete with recycled aggregates. *Construction and Building Materials,* 228, 116783.

Ali B, Qureshi LA, Khan SU (2020). Flexural behavior of glass fiber-reinforced recycled aggregate concrete and its impact on the cost and carbon footprint of concrete pavement. *Construction Building Materials,* 262, 120820.

Araz NG, Aksoy A, Aslan MT and İskender E (2023). Asfalt kaplamalarda bitüm oranına bağlı olarak sıkıştırma sıcaklığının etkisinin Marshall Deneyi parametreleri ile incelenmesi. *Recep Tayyip Erdogan University Journal of Science and Engineering,* 4(1), 39-50. (in Turkish)

ASTM-C39 (2015). Standard test method for compressive strength of cylindrical concrete specimens. ASTM International, West Conshohocken, PA.

ASTM-C78 (2018). Standard test method for flexural strength of concrete (using simple beam with third-point loading). ASTM International, West Conshohocken, PA.

Baş Fİ, Bayrak OÜ, Bayata HF (2022). A Practical design guide for unbonded jointed plain concrete roads over deteriorated HMA roads: Realistic traffic loading. *Coatings,* 12(12), 1817.

Bentur A, Mindess S. (2006). Fibre Reinforced Cementitious Composites. CRC Press, Boca Raton, FL.

Bhogone M, Subramaniam KV (2022). Improvement in early-age cracking performance of concrete with hybrid steel-macropolypropylene fiber blends. *Materials Today: Proceedings,* 65, 1589-1593.

Cheung Y, Zinkiewicz O (1965). Plates and tanks on elastic foundations–an application of finite element method. *International Journal of Solids Structures,* 1(4), 451-461.

Çelik M (2014). Karadeniz Bölgesi Köy Yolları için Rijit ve Esnek Kaplamanın Mekanistik ve Maliyet Açısından Karşılaştırılması. *M.Sc. thesis*, Karadeniz Technical University, Trabzon. (in Turkish)

Çelik Z, Turan E, Oltulu M, Öner G (2024). Reinforcement of concrete beams using waste carbon-nanoclay-fiberglass laminate pieces. *Challenge Journal of Concrete Research Letters*, 15(1), 1-6.

Çolak MA, Zorlu E, Çodur MY, Baş Fİ, Yalçın Ö, Kuşkapan E (2023). Investigation of physical and chemical properties of bitumen modified with waste vegetable oil and waste agricultural ash for use in flexible pavements. *Coatings,* 13(11), 1866.

Eryılmaz Yıldırım M, Aybar K, Canbaz M (2024). Size effect on compressive behavior of GFRP bars. *Challenge Journal of Structural Mechanics*, 10(1), 14-20.

Gultekin A (2023). Effect of hemp and basalt fiber on fracture energy of cement-based composites: a comparative study. *Challenge Journal of Concrete Research Letters*, 14(4), 107-117.

Huang YH (2004). Pavement Analysis and Design (vol. 2). Pearson Prentice Hall, Upper Saddle River, NJ.

Hussain I, Ali B, Akhtar T, Jameel MS, Raza SS (2020). Comparison of mechanical properties of concrete and design thickness of pavement with different types of fiber-reinforcements (steel, glass, and polypropylene). *Case Studies in Construction Materials,* 13, e00429.

Jagannadha RK, Ahmed KT (2009). Suitability of glass fibers in high strength recycled aggregate concrete-An experimental investigation. *Asian Journal of Civil Engineering (Building and Housing),* 10(6), 681-689.

Jawdhari A, Fam A (2020). Thermal-structural analysis and thermal bowing of double Wythe UHPC insulated walls. *Energy Buildings,* 223, 110012.

Karahan O, Atiş CD (2011). The durability properties of polypropylene fiber reinforced fly ash concrete. *Materials Design,* 32(2), 1044-1049.

KGM (2016). Beton Yol Kaplamaları Teknik Şartnamesi. General Directorate of Highways, Ankara. (in Turkish)

KGM (2023). Trafik ve ulaşım bilgileri, otoyollar ve devlet yollarinin trafik dilimlerine göre yillik ortalama günlük trafik değerleri ve ulaşim bilgileri. General Directorate of Highways, Ankara. (in Turkish)

KGM (2024). Yol Ağı Bilgileri. Karayolları Genel Müdürlüğü. https://www.kgm.gov.tr/Sayfalar/KGM/SiteTr/Kurumsal/YolAgi.aspx [accessed 20-08-2024] (in Turkish)

Kim K (2017). Enhanced Finite Element Analysis Tools and Instrumentation Method to Evaluate the Structural Behavior of Non-Conventional Concrete Pavements. *Ph.D. thesis*, University of Florida, Gainesville, FL.

Kizilkanat AB, Kabay N, Akyüncü V, Chowdhury S, Akça AH (2015). Mechanical properties and fracture behavior of basalt and glass fiber reinforced concrete: An experimental study. *Construction and Building Materials, 100*, 218-224.

Korkiala-Tanttu L (2009). Calculation Method for Permanent Deformation of Unbound Pavement Materials. VTT Publications, Helsinki.

Kosmatka SH, Kerkhoff B, Panarese WC (2003). Design and Control of Concrete Mixtures. Engineering Bulletin 001, Portland Cement Association, Skokie, Illinois.

Kumara W, Tia M, Wu C-L, Choubane B (2003). Evaluation of applicability of ultra-thin whitetopping (UTW) in Florida*. 2003 Annual Transportation Research Board Meeting*.

Lau CK, Chegenizadeh A, Htut TN, Nikraz H (2020). Performance of the steel fibre reinforced rigid concrete pavement in fatigue. *Buildings,* 10(10), 186.

Moaveni S (2011). Finite element analysis theory and application with ANSYS, 3/e. Pearson Education, India.

Moffatt M (2017). Guide to Pavement Technology Part 2: Pavement Structural Design. Austroads Ltd., Sydney, Australia.

Mohammed SI, Najim KB (2020). Mechanical strength, flexural behavior and fracture energy of recycled concrete aggregate self-compacting concrete. *Structures,* 23, 34-43.

Mola E, Bayrak OÜ, Baş Fİ, Bayata HF (2024). Investigating the usability of kevlar and steel fibers as a hybrid in concrete pavements. *Sigma Journal of Engineering Natural Sciences,* 42(2), 344-355.

Nazki MA, Chopra T, Chandrappa AK (2020). Rheological properties and thermal conductivity of bitumen binders modified with graphene. *Construction and Building Materials,* 238, 117693.

Nguyen Dinh N (2016). Precast ultra-thin whitetopping (PUTW) in Singapore and its application for electrified roadways. *Ph.D. thesis*, Technische Universität, München,

Noorvand H, Arce GA, Hassan MM (2022). Evaluation of the effects of engineered cementitious composites (ECC) plasticity on concrete pavement performance. *International Journal of Pavement Engineering,* 23(13), 4474-4486.

Ntimugura F, Vinai R, Harper A, Walker P (2020). Mechanical, thermal, hygroscopic and acoustic properties of bio-aggregates–lime and alkali-activated insulating composite materials: a review of current status and prospects for miscanthus as an innovative resource in the South West of England. *Sustainable Materials Technologies,* 26, e00211.

Roesler J, Bordelon A, Brand AS, Amirkhanian A (2019). Fiber-reinforced concrete for pavement overlays: Technical overview. In-Trans Project, 15-532.

Roesler JR, Lange DA, Altoubat SA, Rieder K-A, Ulreich GR (2004). Fracture of plain and fiber-reinforced concrete slabs under monotonic loading. *Journal of materials in Civil Engineering,* 16(5), 452-460.

SAS (2024). ANSYS Engineering Simulation Student Software. SAS IP Inc.

Sharbatdar MK, Rahmati F (2022). Experimental evaluation of multifunctional effects of fibers on mechanical and performance properties of Roller-compacted concrete pavements (RCCP). *Construction and Building Materials,* 316, 125890.

Shoukry SN, Fahmy M, Prucz J, William G (2007). Validation of 3DFE analysis of rigid pavement dynamic response to moving traffic and nonlinear temperature gradient effects. *International Journal of Geomechanics,* 7(1), 16-24.

Sii HB (2015). Three-Dimensional Finite Element Analysis of Concrete Pavement on Weak Foundation. *Ph.D. thesis,* Griffith University, Queensland, Australia.

Sultana S (2010). Extending Asphalt Pavement Life with Thin Whitetopping. *Ph.D. thesis,* Kansas State University, Manhattan, KS.

Sünbül Ş, Tortum A (2024). Investigation of the use of nano powder on roller compressible fibrous concrete roads. *Case Studies in Construction Materials,* 21, e03572.

Şengel H, Kınık K, Erol H, Canbaz M (2022). Effect of waste steel tire wired concrete on the mechanical behavior under impact loading. *Challenge Journal of Structural Mechanics*, 8(4), 150-158.

Tunçel M, Bayrak OÜ, Baş Fİ, Bayata HF (2020). Atık kevların beton yol kaplamalarında kullanılabilirliğinin araştırılması. *Avrupa Bilim ve Teknoloji Dergisi,* 19, 668-678. (in Turkish)

Wu C, Tia M, Larsen T (1993). Analysis of structural response of concrete pavements under critical thermal-loading conditions. *5th International Conference on Concrete Pavement Design and Rehabilitation,* Purdue University, Lafayette, Ind., 1, 317–340. USA.

Zain MFM, Mahmud H, Ilham A, Faizal M (2002). Prediction of splitting tensile strength of high-performance concrete. *Cement Concrete Research,* 32(8), 1251-1258.

Zhang P, Li Q-f (2013). Effect of polypropylene fiber on durability of concrete composite containing fly ash and silica fume. *Composites Part B: Engineering,* 45(1), 1587-1594.

Challenge Journal of Structural Mechanics

Research Article

The mechanical properties of cement mortar reinforced with silica fume subjected to sulfate and chloride environment

Sulaiman Al-Safi [a], Abdulghani Altharehi [a,*], Ibrahim A. Alameri [a], Abdulmalek Al-Jolahy [a]

[a] *Department of Civil Engineering, Sana'a University, 13341 Sana'a, Yemen*

ABSTRACT

This study investigates the effect of incorporating micro-sized silica fume on the mechanical properties and durability of cement mortar when exposed to sulfate and chloride environments. Mortar samples were prepared by replacing cement with micro-sized silica fume in varying proportions of 5%, 10%, 15%, 20%, 25%, 30%, and 35% by weight. The specimens were cured in water and chemically aggressive conditions, including 5% and 10% sodium sulfate solutions, as well as mixtures of 5% and 10% sodium chloride solutions, to simulate real-world exposure to such environments. Experimental results revealed that the addition of silica fume significantly enhanced the mortar's resistance to chemical deterioration caused by sulfates and chlorides. This improvement is attributed to the pozzolanic reaction of silica fume, which contributed to denser microstructures, reduced porosity, and a stronger bond within the matrix. Among the tested proportions, the optimal replacement ratios for achieving the best balance between mechanical strength and durability were identified up to 20%. These findings highlight the efficiency of silica fume as a supplementary cementitious material in mitigating the adverse effects of aggressive chemical agents. Such modifications can be particularly valuable in improving the service life of concrete structures exposed to harsh environmental conditions, enhancing sustainability and cost-effectiveness in construction practices.

ARTICLE INFO

Article history:
Received – November 5, 2024
Revision requested – December 23, 2024
Revision received – January 13, 2025
Accepted – January 21, 2025

Keywords:
Cement mortar
Silica fume
Sulfate attack
Chloride attack
Reactivity

Citation: Al-Safi S, Altharehi A, Alameri IA, Al-Jolahy A (2025). The mechanical properties of cement mortar reinforced with silica fume subjected to sulfate and chloride environment. *Challenge Journal of Structural Mechanics*, 11(1), 55–69.

1. Introduction

Although concrete is widely recognized for its strength and durability, it is susceptible to environmental factors that can degrade its integrity over time (Alameri et al. 2020). Among these, sulphate and chloride attacks are particularly insidious. Sulfate ions, common in some soils and groundwater, initiate expansive chemical reactions within the concrete matrix, leading to cracking and deterioration. Chloride ions, on the other hand, often originating from de-icing salts or marine environments, penetrate the concrete to corrode its steel reinforcement and weaken micro-structural stability. Acid attacks typically result from various industrial processes and related applications (Atabey et al. 2023).

Pozzolans have long been recognized as vital supplementary materials in enhancing the performance and durability of concrete (Saif Allah et al. 2024). These materials, including natural pozzolans such as fly ash (Harirchian 2024), silica fume (Güney and Yıldızel 2024), and volcanic ash (Atasever and Tokyay 2024), are widely utilized to improve the longevity of concrete structures (McCarthy and Dyer 2019). By refining the microstructure and reducing permeability, pozzolans effectively limit the ingress of aggressive sulfate and chloride ion (Anwar 2005). This significantly reduces the risk of chloride-induced corrosion in steel reinforcement. Additionally, certain pozzolans, such as silica fume, possess unique properties that further enhance the overall performance of concrete. (Feng et al. 2018).

* *Corresponding author*. E-mail address: a.altharhi@su.edu.ye (A. Altharehi)
ISSN: 2149-8024 / DOI: https://doi.org/10.20528/cjsmec.2025.01.005

Silica fume, which is rich in silicon dioxide, enhances the durability of concrete by improving its resistance to sulfate and chloride attacks (Şimşek et al. 2022). This ultra-fine pozzolan reacts with the calcium hydroxide produced during cement hydration to form additional calcium silicate hydrate (C-S-H) (Al-Saffar et al. 2023). It results in a much denser and more refined microstructure, significantly reducing the permeability of the concrete. This dense matrix acts as a barrier against the penetration of sulphate ions, which are known to cause expansive chemical reactions leading to cracking and deterioration (Shannag and Shaia 2003). By minimising the entry of these harmful ions, silica fume prevents the formation of harmful compounds such as gypsum and ettringite, thus preserving the integrity of the concrete. In chloride-laden environments, such as coastal areas or areas where de-icing salts are used, the low permeability caused by silica fume is equally beneficial, as silica fume not only slows low chloride ingress but also increases the concrete's ability to chemically bind these ions, reducing their availability to initiate corrosion of steel reinforcement. This dual effect – as both a physical barrier and a chemical binder – makes silica fume an indispensable additive for concrete exposed to aggressive sulphate and chloride conditions (Ortega et al. 2018). Previous studies, listed in Table 1, have extensively investigated the effectiveness of silica fume in reducing sulphate and chloride attacks in concrete and have highlighted its fundamental role in enhancing the durability of the material. These studies used advanced analytical techniques such as scanning electron microscopy (SEM) and X-ray diffraction (XRD) to observe the microstructural changes and porosity reduction caused by silica fume. In addition, long-term exposure tests in aggressive environments confirmed the superior performance of silica fume-modified concrete, with results showing significantly lower sulphate-induced expansion and chloride-induced corrosion rates compared to conventional concrete (Sharaky et al. 2019). Understanding the mechanisms and effects of these attacks is crucial for engineers and builders aiming to increase the longevity and durability of concrete structures (Abed et al. 2018).

This article highlights the important role of using silica fume in cement mortars, especially in enhancing the fresh, physio-mechanical and durability of mortars subjected to high silica fume volume (up to 35%) and exposed to different concentration of NaCl and Na_2SO_4 conditions.

Table 1. Previous research related to the study.

Authors	Silica fume ratio (%)	Experiments	Optimum silica fume ratio found (%)
Saif Allah et al. (2024)	23, 46, 69	Compressive strength, Splitting tensile strength, Absorption test	69
Anwar (2005)	10	Compressive strength, Flexural strength, Pulse velocity, Dynamic elastic modulus	10
Kumar et al. (2022)	5,10, 15 (2.5%SF+2.5%FA, 5%SF+5%FA, 7.5%SF+7.5%FA)	Compressive strength, Splitting tensile strength, Water absorption	10 (with 7.5%SF+7.5%FA)
Şimşek et al. (2022)	0, 2.5, 5, 7.5, 10, 12.5, 15	Density, Setting time, Soundness, Compressive strength, Flexural strength	10
Ramezanianpour et al. (2020)	7.5 (with a natural pozzolan: 17.5)	Compressive strength, Capillary absorption, Penetration depth, Penetration profile, RCMT analysis, XRD analysis	7.5
Tripathi et al. (2020)	5, 10, 15, 20, 25	Fresh concrete properties, Compressive strength, Weight change	20
Sharaky et al. (2019)	5, 10, 15	Length expansion, Compressive strength, X-ray diffraction, DSC analysis, SEM analysis, EDX analysis	30
Abed et al. (2018)	0, 15, 25, 35	Compressive strength	25
Shetti and Das (2015)	1, 2, 3, 4, 5, 6	Slump, Compaction factor, Compressive strength, Acid attack, Water absorption, Chloride attack, Alkali attack	6
Lee et al. (2005)	5, 10, 15	Compressive strength	5, 10
Shannag and Shaia (2003)	0, 20, 40, 60 (+ natural pozzolan: 0, 5, 10, 15)	Compressive strength, UPV	15

2. Methodology

2.1. Materials

In this study, cement mortar samples were prepared using ordinary Portland cement (OPC) according to ASTM C150 (2024) was supplied by Amran Cement Plant. Specific gravity and fineness for cement were 3.15 g/cm^3 and 3140 cm^2/g. The used silica fume (SF) powder has a specific surface area of 20 m^2/g; it was sieved from a 75 μm sieve for eliminating large particles, an average diameter of 0.15 μm, silicon dioxide of 88.6%, and a specific gravity of 2.20 g/cm^3 (Fig. 1). Moreover, the chemical composition of both cement and silica fume is listed in Table 2.

Sand was used as a fine aggregate, and the specific gravity and water absorption were laboratory determined as 2.60 g/cm^3 and 1.40%, respectively.

Fig. 1. Silica fume.

Table 2. Chemical composition of the portland cement and silica fume.

Material	Oxide composition by mass (%)					
	SiO_2	CaO	MgO	Al_2O_3	Fe_2O_3	SO_3
Cement	23.2	55.1	2.2	7.4	5.4	2.0
Silica fume	88.6	0.99	0.26	1.11	0.66	0.33

2.2. Mix proportions, curing methods and sample preparation

In this study, based on the trial-and-error method to produce the best homogeneous, optimum cement dosage and W/B ratio, the control cement mortar sample was prepared as 1:1:0.45 for cement, fine aggregate, and water, respectively. A water reduction additive (superplasticizers (SPZ)) was used by a constant percentage (0.8%) of binder weight to increase mix workability. The other groups were prepared by replacing silica fume with 5%, 10%, 15%, 20%, 25%, 30%, and 35% by weight of cement. Table 3 shows the mixing ratios for each group.

Table 3. Mixture details and formulation code of the control and silica fume based mortar exposed to different solutions.

Group	Component weight (g)				
	Cement	Silica fume	Fine aggregate	SPZ	W/B
SF0	1000	--	1000	8	450
SF5	950	50	1000	8	450
SF10	900	100	1000	8	450
SF15	850	150	1000	8	450
SF20	800	200	1000	8	450
SF25	750	250	1000	8	450
SF30	700	300	1000	8	450
SF35	650	350	1000	8	450

Test samples were cured under five different conditions: water (laboratory conditions), 5% NaCl solution, 10% NaCl solution, 5% Na_2SO_4 solution, and 10% Na_2SO_4 solution, for 28 days. They were then air-dried for one day before testing.

2.3. Experiments

2.3.1. Slump test

In this study, the slump test was done according ASTM C143 (2020). This test is used for fresh concrete to determine the workability and percentage of water.

2.3.2. Density test

In this study, the average density of three samples in each group was calculated after 28 days. Samples were weighed with a sensitive electronic scale to an accuracy of 0.1 gm, and then density values (ρ) in g/cm^3 were calculated by dividing their mass (m) to their volume according to ASTM C642 (2021).

2.3.3. Ultra-sonic test (UPV)

The UPV test is a non-destructive technique used to evaluate the quality and integrity of mortar specimens. Sound's velocity through mortars gives details about their homogeneity, internal structure, and possible flaws. In this study, cubes with 50×50×50 mm^3 dimensions were directly measured for velocity as per ASTM C597 (2022) and using Eq. (1).

$$V = {}^{L}/_{T} \quad \text{(m/sec)} \tag{1}$$

2.3.4. Dynamic modulus of elasticity

In this study, the dynamic modulus of elasticity was calculated as per ASTM E494 (2020). For each sample and Eq. (2) were applied, then the average dynamic modulus of elasticity value was found for each group. Poisson's ratio of mortar was assumed as 0.17.

$$E_d = \frac{V_{\text{long}}^2 \cdot \rho \cdot (1+\nu) \cdot (1-2\nu)}{1-\nu} \tag{2}$$

where E_d is the dynamic modulus of elasticity, ρ is the mass density (g/cm^3), ν is the Poisson's ratio of mortar, and V_{long} is the speed rate of wave in specimen m/sec.

2.3.5. Capillary water absorption test

The capillary water absorption test was conducted in accordance with the standard ASTM C1585 (2020) after 28 days. The sides of the specimens were sealed with tape up to 20 mm in height so that only one face of the specimen was subjected to water. Water absorption measures were recorded from 2 min to 24 hr.

2.3.6. Compressive strength test

In this study, compression test was applied after 28 days by different curing methods (water, sodium sulfate and sodium chloride solve). The specimens were placed on a compression testing machine with a capacity of 2500 kN and a loading rate of 0.4 N/mm^2/sec, according to the ASTM C109 (2020). The load is applied gradually until the specimen fails. Stress-strain curved

were drawn and then, the modulus of elasticity, maximum compressive stress and strain values were calculated.

2.3.7. Flexural test

In this study, the flexural strength of prismatic beams (40×40×160 mm³) was obtained through a three-point bending (TPB) test based on the ASTM D790 (2017). A test machine of 50 kN with a controlled displacement rate of 0.2 mm/min was used. Average flexural strength values were measured at 28 days.

3. Results and Discussion

This study evaluated the fresh, physio-mechanical, and durability properties of mortars containing silica fume (up to 35%) under varying concentrations of NaCl and Na_2SO_4. The assessment included visual inspections, density measurements, ultrasonic pulse velocity, dynamic modulus of elasticity, capillary absorption, compressive strength, modulus of elasticity, and flexural tensile strength. The findings are systematically summarized in this section.

3.1. Slump

The results of the slump test were summarized in Table 4 and Fig. 2. Results clearly show that, as the amount of silica fume increases, the workability decreases. For the reference group (SF0), a 250 mm slump value was observed, and a linearly slight decrease was observed in the SF5, SF10, and SF10 groups. While a significant sudden drop was observed at SF20 to SF35 by 52% to 80%, respectively. Thus, silica fume particles with a high surface area require more water in combinations more than mixtures without silica fume.

Table 4. Physical and mechanical results.

Group	Slump (mm)	Density (kg/m³)	UPV test (m/sec)	Dynamic modulus of elasticity (GPa)	Flexural strength (MPa)
SF0	250	2,003.3	4,168.0	31.96	7.031
SF5	230	2,019.2	4,170.4	32.22	8.906
SF10	220	2,064.1	4,610.6	40.28	8.438
SF15	200	2,055.8	4,312.3	35.11	7.575
SF20	120	1,974.2	4,239.9	32.59	6.976
SF25	80	1,945.4	4,204.2	31.58	6.064
SF30	60	1,968.1	4,034.7	29.38	4.098
SF35	30	1,954.2	4,148.4	30.88	3.642

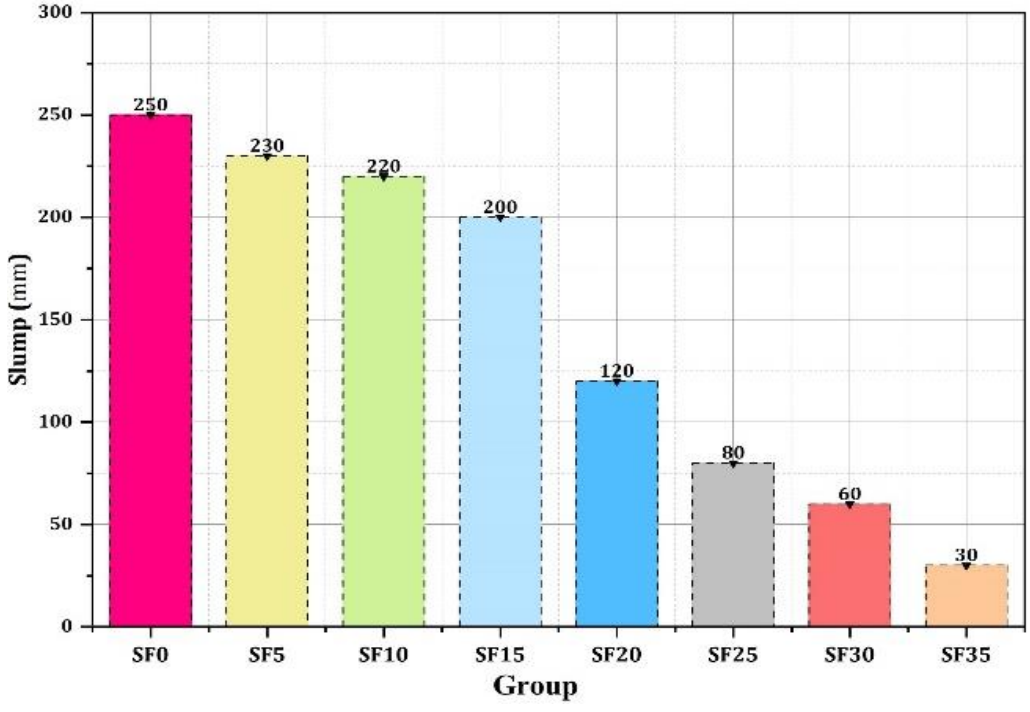

Fig. 2. Slump test results.

3.2. Density

The results of the density test on cement mortars with varying percentages of silica fume reveal a particular trend which indicates the effect of silica fume on the microstructure of the matrix. The density rises from 2.00 g/cm^3 with 0% silica fume to a maximum of 2.06 g/cm^3 with 10% silica fume. This is so because silica fume consists of ultrafine particles, it also fills in the cracks between cement bases or grains and makes more C-S-H, which effectively enhances the density. However, beyond 10%, the density begins to decline, with values dropping to 2.05 g/cm^3 at 15%, 1.98 g/cm^3 at 25%, and further to 1.95 g/cm^3 at 35% silica fume. The decline feature at higher percentages can be explained due to excessive fine nature of silica fume increasing the water demand hence poor workability and compaction uniformity. The findings indicate that silica fume densifies the composite up to an optimum amount of 10%. Beyond this amount, SiO_2 constitutes the mortar, which may lead to disruptions in homogeneity and segregation, making the mortar comparatively less dense.

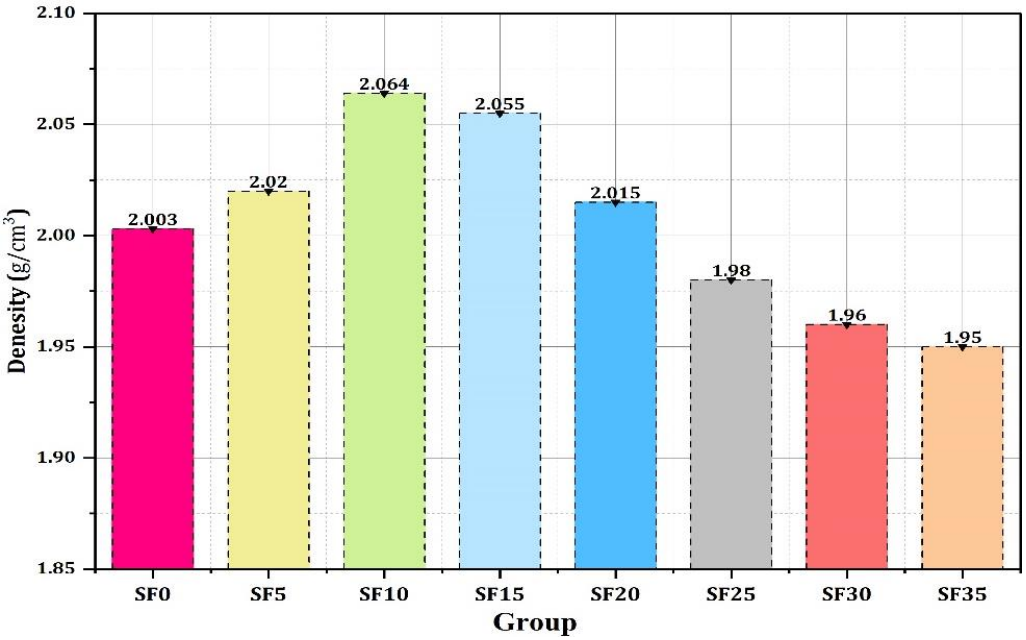

Fig. 3. Density test results.

3.3. Ultrasonic pulse velocity (UPV)

The results of UPV were listed in Table 4 and shown in Fig. 4. The UPV and density test results for cement mortars with varying silica fume contents show a parallel trend that highlights how microstructural changes affect both wave transmission and material density. Initially, both UPV and density increase, with UPV rising from 4168 m/s at 0% silica fume to a peak of 4610 m/s at 10%, and density increasing from 2.00 g/cm^3 to 2.06 g/cm^3 over the same range. This simultaneous rise in UPV and density indicates that up to 10% silica fume contributes to a denser, more uniform microstructure, likely due to improved particle packing and enhanced C-S-H formation through the pozzolanic reaction. This densification reduces porosity, allowing sound waves to travel faster and improving the mortar's structural integrity.

However, as silica fume content increases beyond 10%, both UPV and density begin to decline. UPV values drop from 4610 m/s to 4034 m/s at 30% silica fume, while density decreases from 2.06 g/cm^3 to 1.96 g/cm^3, indicating that higher silica fume levels may introduce microstructural inconsistencies. This parallel decline in UPV and density at higher silica fume levels underscores the importance of balanced silica fume content for enhancing both the material's structural integrity and wave propagation properties. Fig. 5 shows the correlation between UPV and density with R^2=0.657.

3.4. Dynamic modulus of elasticity

Fig. 6 and Table 4 show the dynamic modulus of elasticity results of each group. The results for the dynamic modulus of elasticity, UPV, and density tests for cement mortars for all groups containing silica fume exhibit a closely related trend that illustrates how micro structural densification influences each property. Initially, all three properties - dynamic modulus, UPV, and density - show an increase with silica fume addition up to 10%. The dynamic modulus rises from 31.9 GPa at 0% to a peak of 40.2 GPa at 10% silica fume, UPV increases from 4168 m/s to 4610 m/s, and density reaches its maximum at 2.06 g/cm^3. This parallel improvement suggests that up to 10% silica fume promotes a denser and more uniform matrix.

Beyond the 10% silica fume content, however, all three properties begin to decline, with the dynamic modulus dropping to 29.4 GPa at 30% silica fume, UPV falling to 4034 m/s, and density decreasing to 1.96 g/cm^3. This trend suggests that excess silica fume may negatively impact the compactness and uniformity of the matrix, likely due to reduced workability.

The alignment in the trends of dynamic modulus, UPV, and density indicates that around 10% silica fume is optimal for enhancing the mortar's overall physical and mechanical properties.

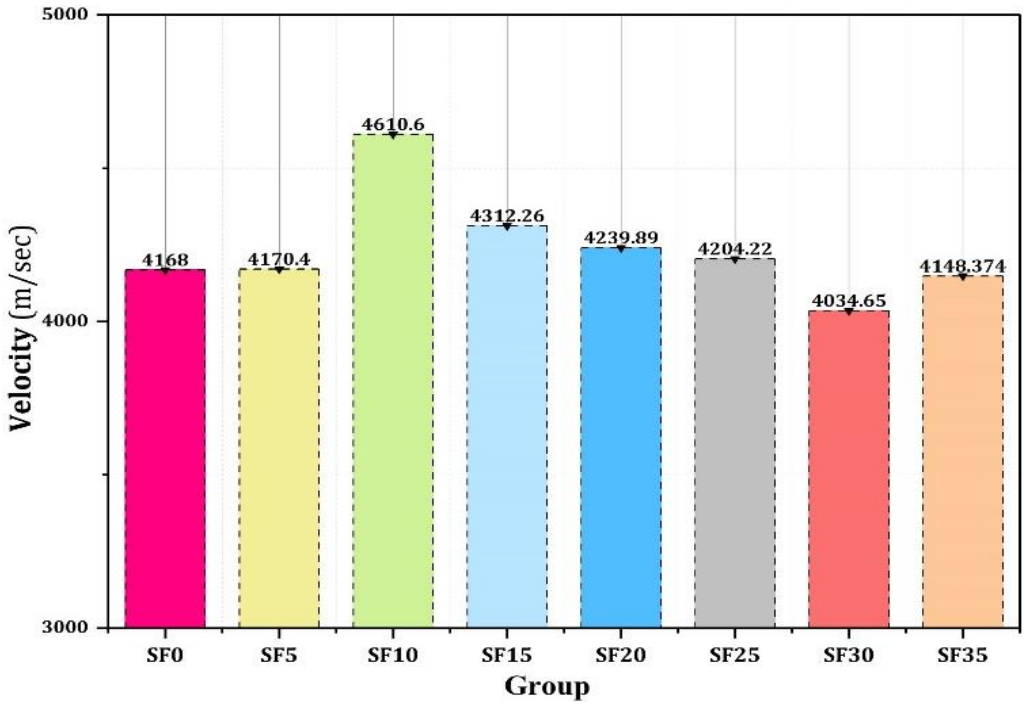

Fig. 4. UPV test results.

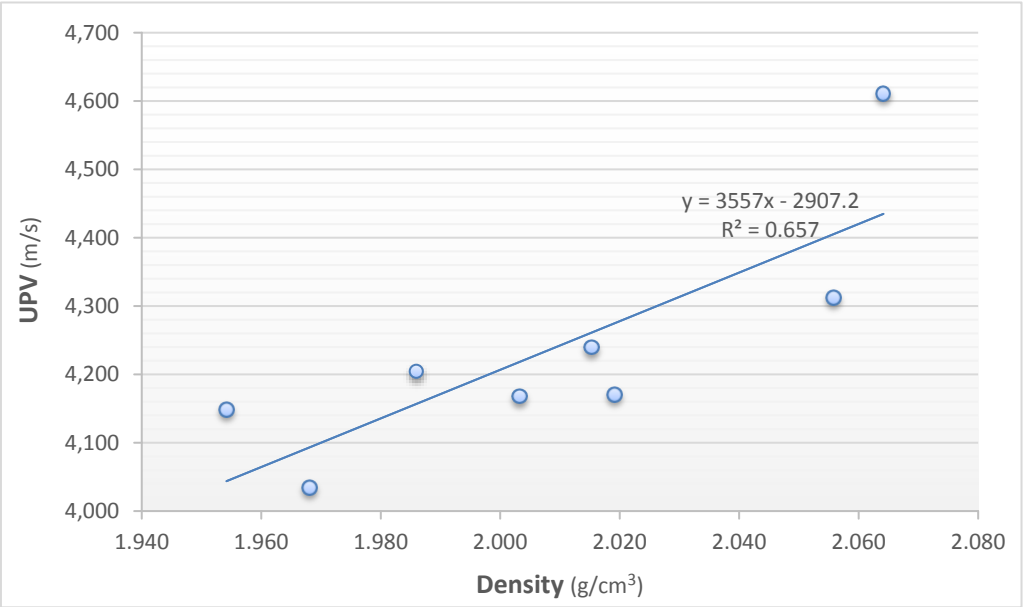

Fig. 5. Correlation between UPV and density.

3.5. Capillary absorption

Each point in Fig. 7 is the average value of measurements of three specimens. The capillary permeability of the mortar changed depending on the amount of SF. The graph shows an overall increasing trend in capillary rise with time for all samples. All the other samples (SF5 to SF35) show higher capillary rise at any given time compared to SF0. The highest increase is observed in FS35, with a 160%.

3.6. Compressive strength

The results of compressive strength for specimens cured in water, 5% NaCl solution, 10% NaCl solution, 5% Na_2SO_4 solution, and 10% Na_2SO_4 solution for 28 days were calculated as the average of three samples from each group, as shown in Table 5 and Figs. 8–10. The compressive strength results for all groups reveal a trend that aligns with observed changes in UPV and density, providing insight into how silica fume influences the

overall matrix strength and compactness. Initially, compressive strength increases sharply from 38 MPa at 0% silica fume to 53.1 MPa at 5%, reaching 46.8 MPa at 10%. This improvement mirrors the rise in both UPV (from 4168 m/s to 4610 m/s) and density (from 2.00 g/cm^3 to 2.06 g/cm^3) within the same range, indicating that the addition of silica fume enhances matrix densification. Up to 10% silica fume, the finer particles fill micro voids and engage in a pozzolanic reaction with calcium hydroxide to form additional C-S-H, which binds the matrix more effectively, increases compaction, and boosts strength.

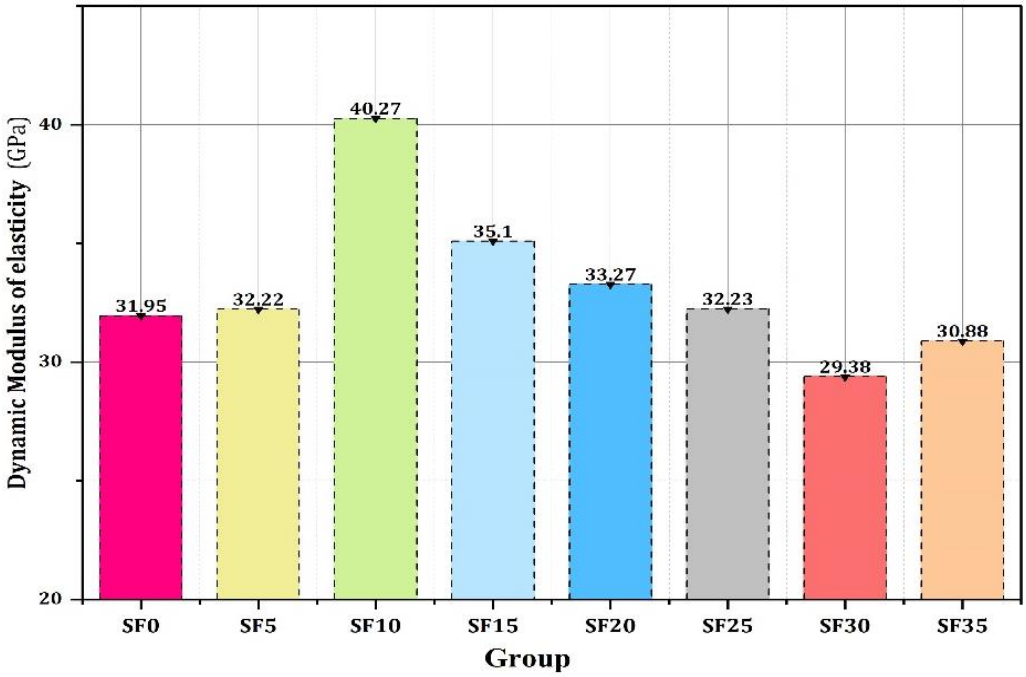

Fig. 6. Dynamic modulus of elasticity test results.

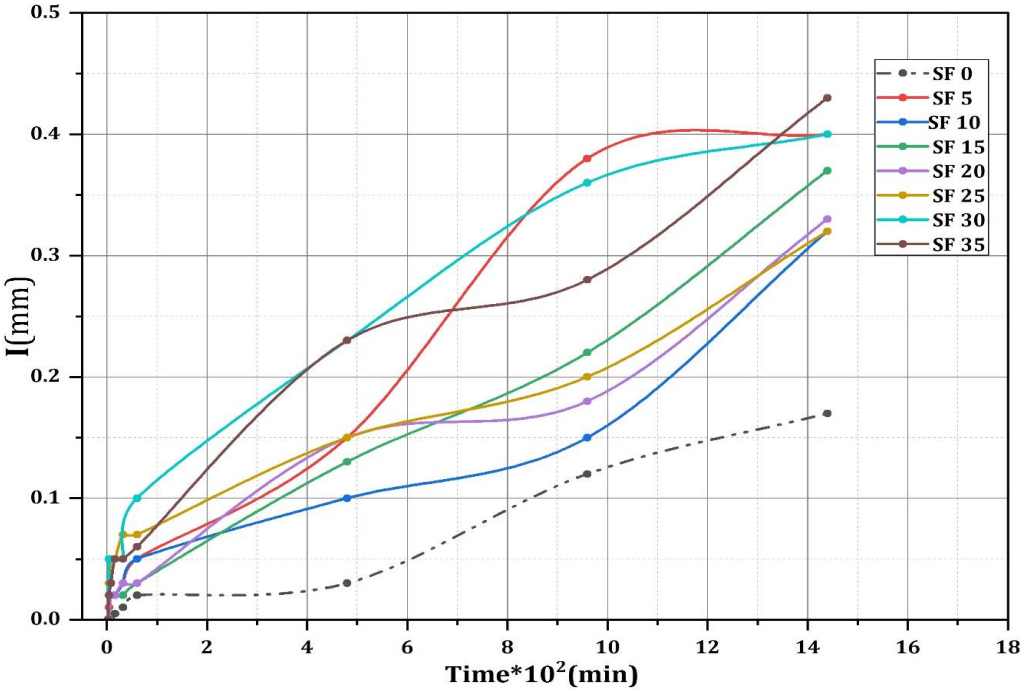

Fig. 7. Capillary test results.

Beyond 10% silica fume, compressive strength begins to decline, reaching 44.2 MPa at 15% and further decreasing to 36.8 MPa at 35%. This downward trend in compressive strength aligns with the reductions in UPV (dropping to 4034 m/s) and density (falling to 1.96 g/cm^3) observed at higher silica fume contents.

These results suggest that while adding silica fume around 5–10% enhances compressive strength by im-

proving microstructural densification hence higher silica fume contents lead to diminishing returns across all properties.

The compressive strength results for cement mortars cured in a 5% NaCl solution reveal a notable decrease for all silica fume groups compared to samples cured in water.

Compressive strength values drop from 38 MPa at 0% silica fume to 35 MPa, from 53.1 MPa at 5% to 39 MPa, and from 46.8 MPa at 10% to 36.6 MPa. This trend indicates that exposure to a saline environment adversely affects the mechanical properties, likely due to the corrosive effects of sodium chloride on the concrete matrix. The reductions in compressive strength are particularly pronounced at higher silica fume contents, with values decreasing to 32 MPa at 30% and 27.8 MPa at 35%, compared to 40.7 MPa and 36.8 MPa in the water-cured results.

The compressive strength results for cement mortars cured in a 10%NaCl solution demonstrate a further decline in strength across all silica fume content levels compared to the both water and 5%NaCl conditions. Specifically, compressive strength values decrease from 38 MPa at 0% silica fume to 34 MPa, from 53.1 MPa at 5% to 36.8 MPa, and from 46.8 MPa at 10% to 30.5 MPa. The decline in compressive strength is particularly significant at 10% and higher silica fume contents, where the strengths drop to 31.4 MPa at 15%, 31.5 MPa at 20%, 31.3 MPa at 25%, and 28.1 MPa at 35%.

The observed reductions in strength can be attributed to the higher concentration of sodium chloride intensifies the corrosive impact on the cement matrix, which can disrupt the formation and integrity of C-S-H and compromise the bond between the silica fume and the cement matrix. Additionally, the presence of NaCl at elevated concentrations may also induce internal stresses and microcracking, particularly in mortars with higher silica fume content, which are already predisposed to brittleness (Zhou et al. 2015).

Table 5. Compressive strength results.

Group	Compressive strength at 28 days (MPa)				
	Water	5% NaCl	10% NaCl	5% Na_2So_4	10% Na_2So_4
SF0	38.00	35.08	34.03	34.36	30.45
SF5	53.12	39.20	36.85	39.42	38.00
SF10	46.76	36.64	30.53	37.81	35.16
SF15	44.21	41.94	31.44	40.77	36.05
SF20	40.70	37.40	35.60	44.50	43.40
SF25	40.58	32.00	31.50	39.13	35.53
SF30	41.62	32.12	31.30	31.21	29.87
SF35	36.78	27.81	28.10	30.55	28.00

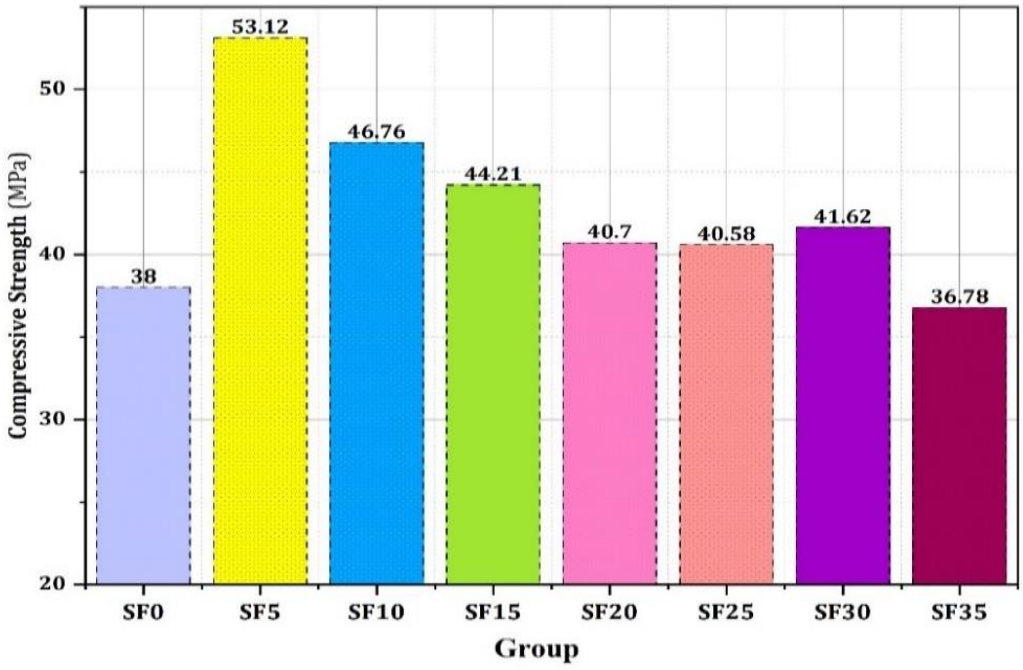

Fig. 8. Compressive strength results for the samples cured in water.

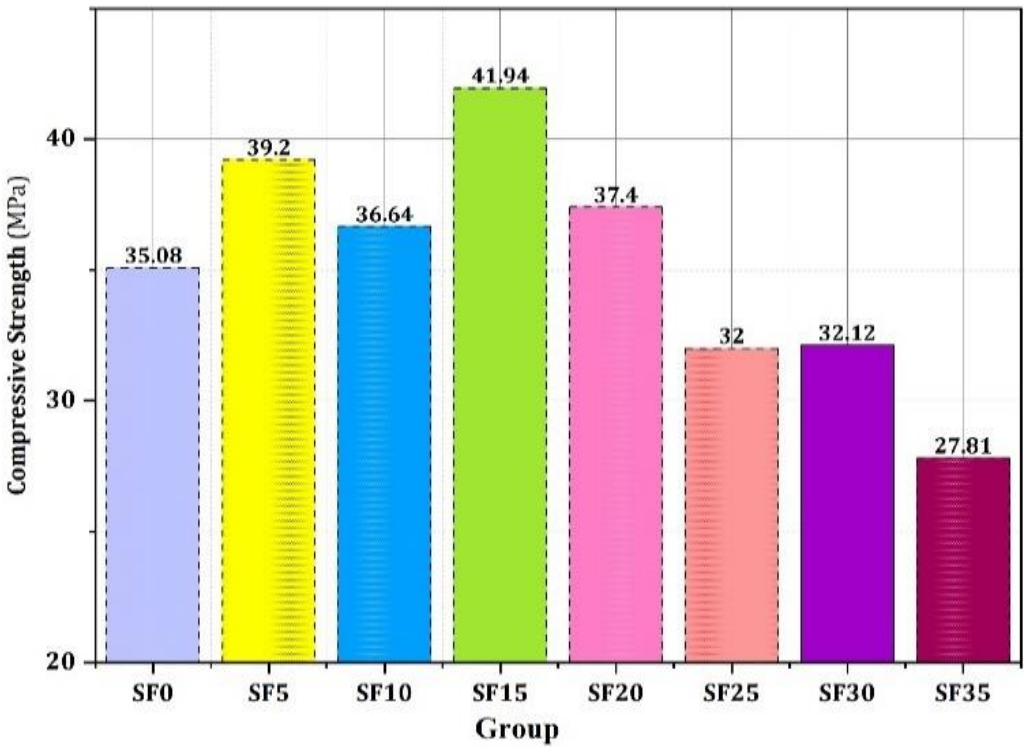

Fig. 9. Compressive strength results for the samples cured in 5% NaCl solution.

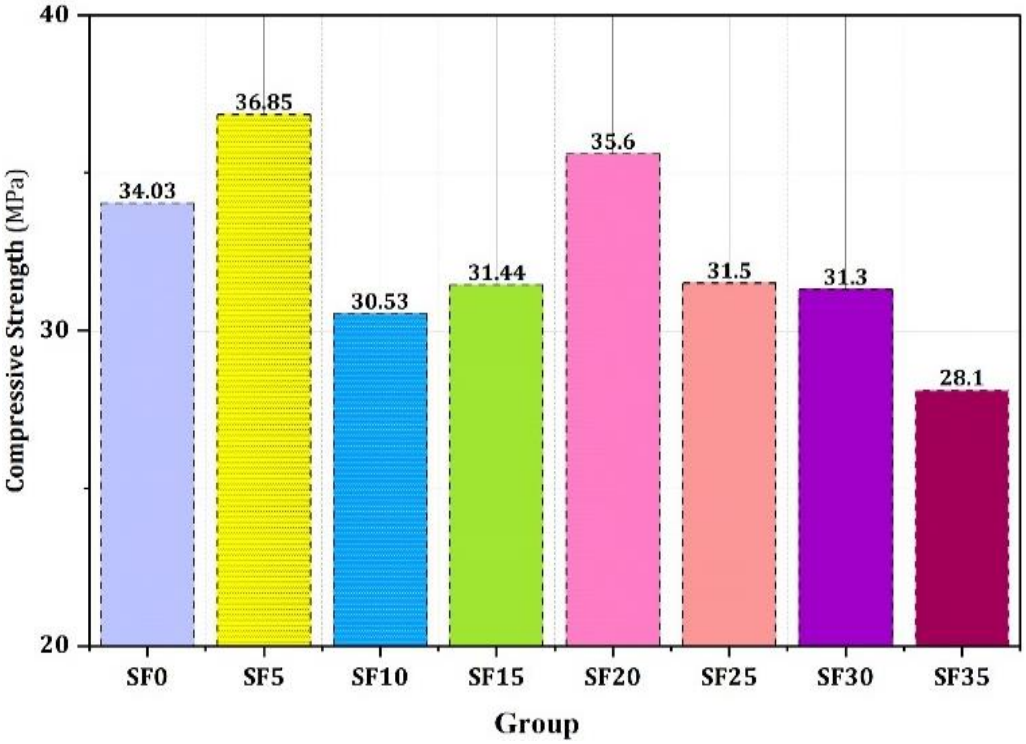

Fig. 10. Compressive strength results for the samples cured in 10% NaCl solution.

The compressive strength results for cement mortars cured in 5% and 10% Na_2SO_4 solutions reveal a significant decline in strength across all silica fume content levels compared to the compressive strengths obtained under water curing conditions (Figs. 11–12). In the 5% Na_2SO_4 solution, compressive strength values are recorded as 34.36 MPa at 0% silica fume, 39.4 MPa at 5%, 37.8 MPa at 10%, 40.77 MPa at 15%, 44.5 MPa at 20%, 39.13 MPa at 25%, 31.2 MPa at 30%, and 30.5 MPa at 35%. In comparison, the results for specimens cured in 10% Na_2SO_4 show further reductions, with compressive strengths of 30.4 MPa at 0%, 38 MPa at 5%, 35.2 MPa at 10%, 36.1 MPa at 15%, 43.4 MPa at 20%, 35.5 MPa at 25%, 29.8 MPa at 30%, and 28 MPa at 35%.

The initial decline in compressive strength in the 5% Na_2SO_4 solution compared to water-cured specimens

reflects the detrimental effects of sulfate ions, which can react with the hydration products in cement, potentially leading to the formation of expansive products such as ettringite. This expansive reaction may create internal stresses within the mortar matrix, promoting cracking and reducing overall strength. The further decrease in compressive strength observed in the 10% Na_2SO_4 solution suggests that higher sulfate concentrations exacerbate these effects, leading to increased permeability and more significant microstructural damage (Han and Li 2024). Notably, while some mortars, particularly those with 20% silica fume, show relatively higher strength retention in both sulfate solutions compared to others, the overall trend emphasizes the vulnerability of silica fume-enhanced mortars to Na_2SO_4 attack.

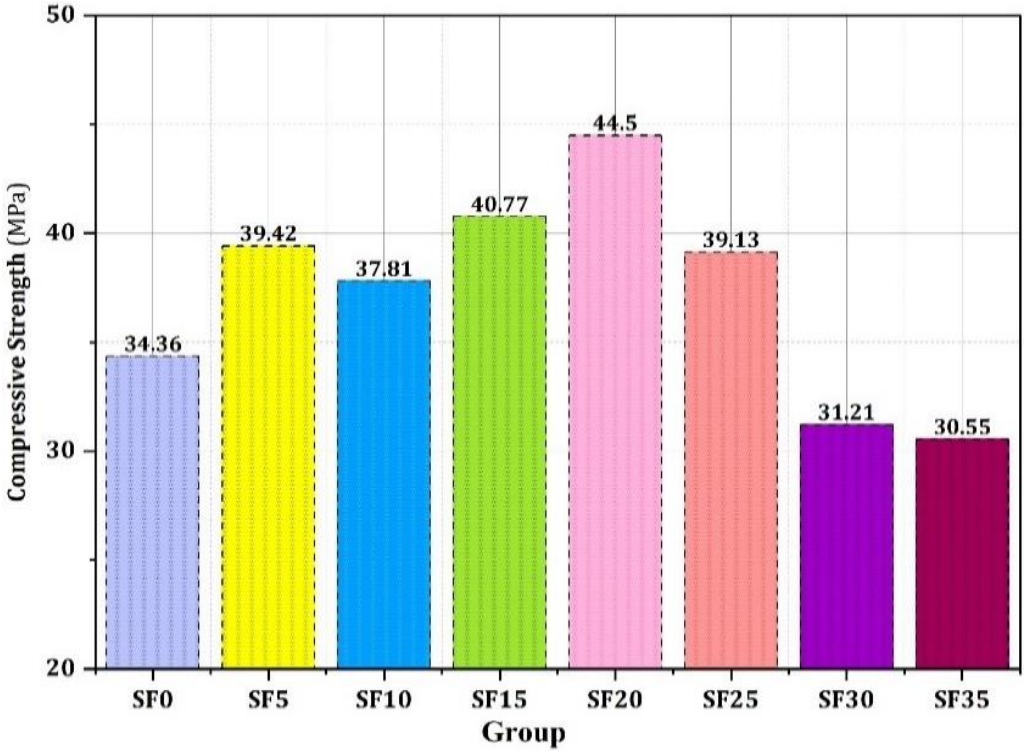

Fig. 11. Compressive strength results for the samples cured in 5% Na_2So_4 solution.

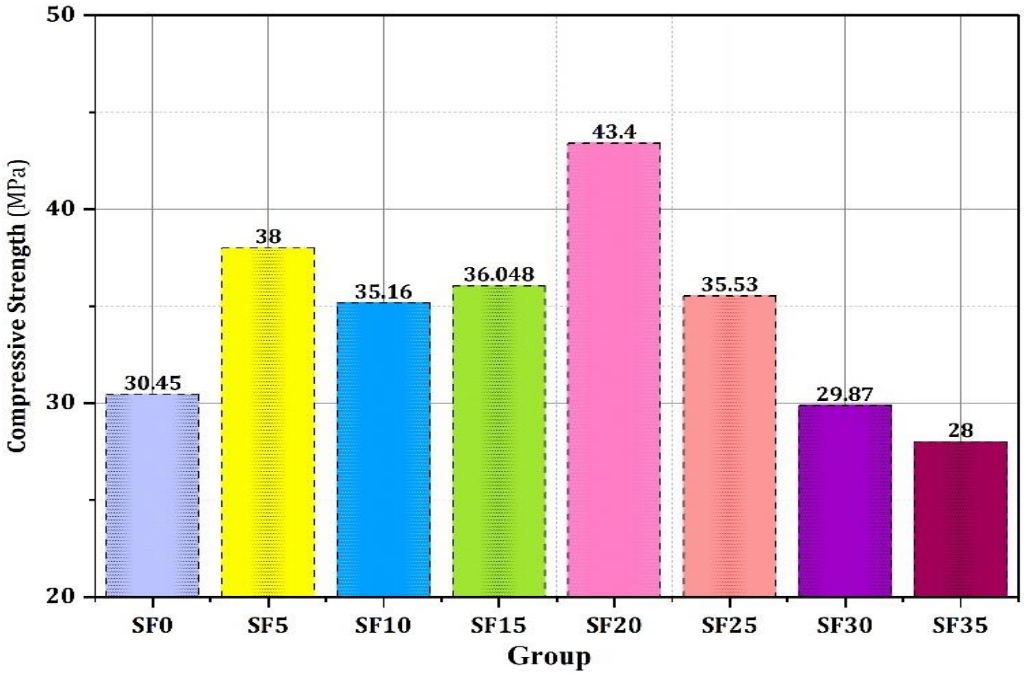

Fig. 12. Compressive strength results for the samples cured in 10% Na_2So_4 solution.

3.7. Modulus of elasticity

Table 6 summarizes the results of modulus of elasticity and Figs. 13–17 show the stress-strain curves under compression for all curing methods. The modulus of elasticity results reflects significant differences based on the curing conditions, showcasing how aggressive environmental factors influence the mechanical behaviour. For specimens cured in water, the modulus values range from 4.3 GPa at 0% silica fume to a peak of 12.3 GPa at 10%. The optimal hydration conditions provided by water curing facilitate the pozzolanic reaction, allowing the silica fume to effectively contribute to the matrix's strength and elasticity.

In contrast, when the specimens are cured in a 5% Na_2SO_4 solution, the modulus values drop significantly, ranging from 3.3 GPa at 0% silica fume to 9.3 GPa at 15%. The decline in modulus continues to be pronounced in specimens cured in a 10% Na_2SO_4 solution, with values ranging from 3.1 GPa at 0% silica fume to a maximum of only 8.4 GPa at 15%. The formation of ettringite and other expansive products is likely intensified, leading to greater microstructural damage and a more significant loss of elasticity.

Comparatively, the results from specimens cured in saline environments exhibit similar downward trends in modulus of elasticity. In the 5% NaCl-cured specimens, modulus values range from 4.8 GPa at 0% silica fume to 6.6 GPa at 15%. Although the modulus is higher than that observed in the sulphate-cured specimens, the presence of sodium chloride still negatively impacts the mortar's stiffness.

Finally, the lowest modulus values are recorded for specimens cured in a 10% NaCl solution, where results range from 3.4 GPa at 0% silica fume to 4.98 GPa at 20%. The decline in modulus compared to both water-cured and 5% NaCl specimens suggests that the higher concentration of chloride exacerbates the detrimental effects on the mortar's mechanical properties. The increased salinity may enhance the likelihood of microcracking and reduce the overall elastic behaviour of the mortar.

Table 6. Modulus of elasticity results.

Group	Modulus of elasticity at 28 days (GPa)				
	Water	5% NaCl	10% NaCl	5% Na_2So_4	10% Na_2So_4
SF0	4.34	4.77	3.41	3.29	3.13
SF5	11.91	4.42	3.55	5.54	8.84
SF10	12.33	5.36	4.14	4.95	5.33
SF15	9.70	6.60	3.22	9.30	3.74
SF20	9.63	6.40	4.98	8.36	8.40
SF25	7.46	5.05	3.80	7.28	3.76
SF30	9.50	3.67	3.54	4.66	2.70
SF35	8.71	3.37	3.27	4.00	3.52

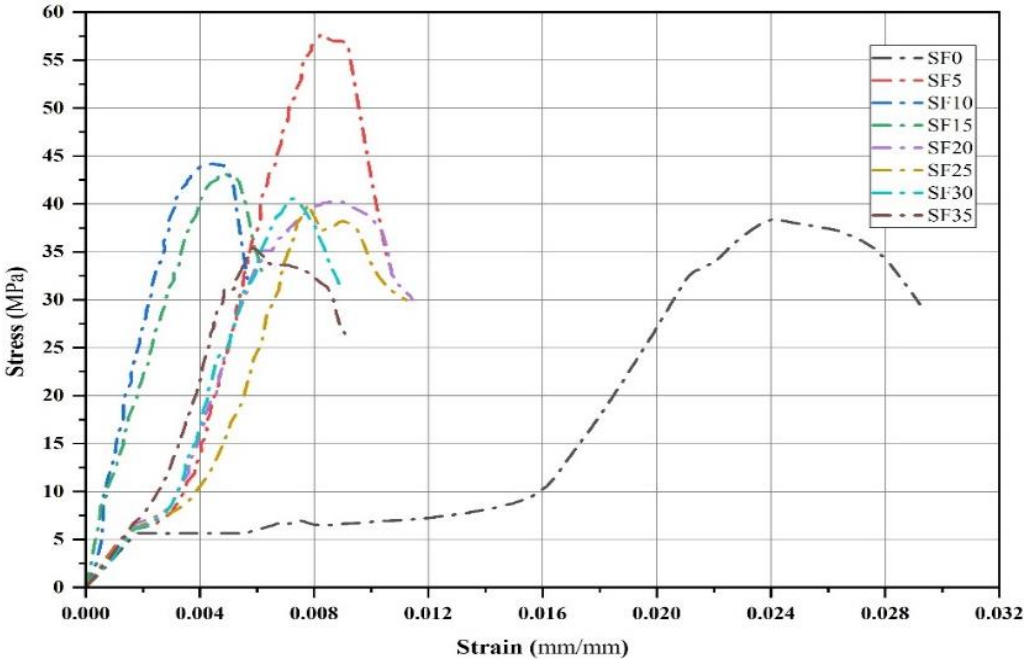

Fig. 13. Stress-strain curve for the groups cured in water.

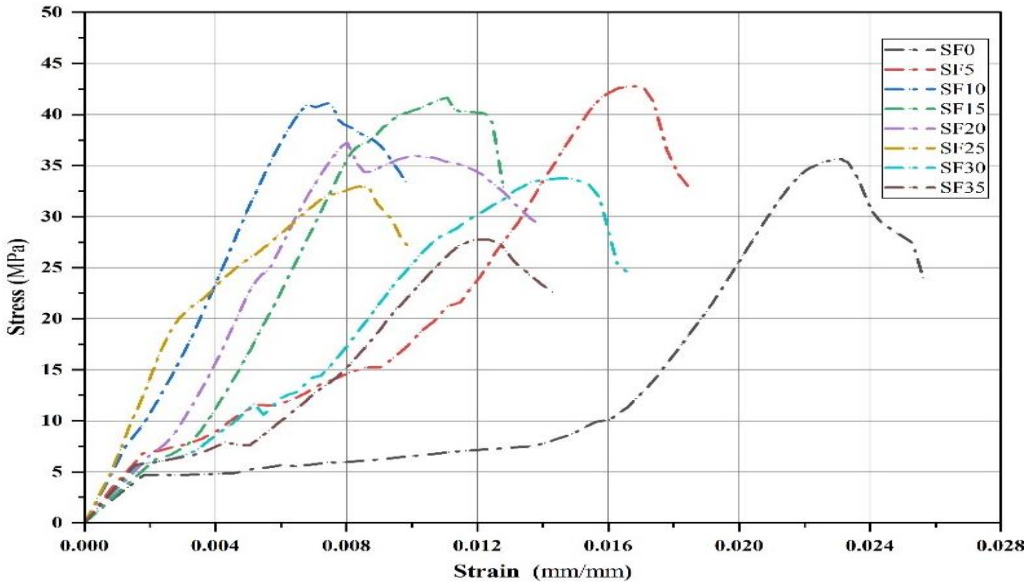

Fig. 14. Stress-strain curve for the groups cured in 5% NaCl solution.

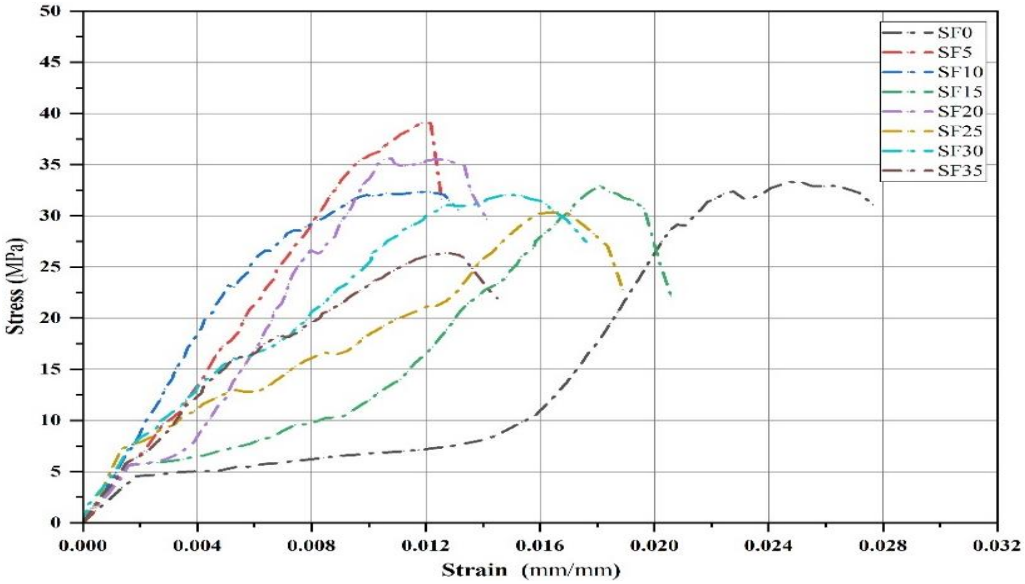

Fig. 15. Stress-strain curve for the groups cured in 10% NaCl solution.

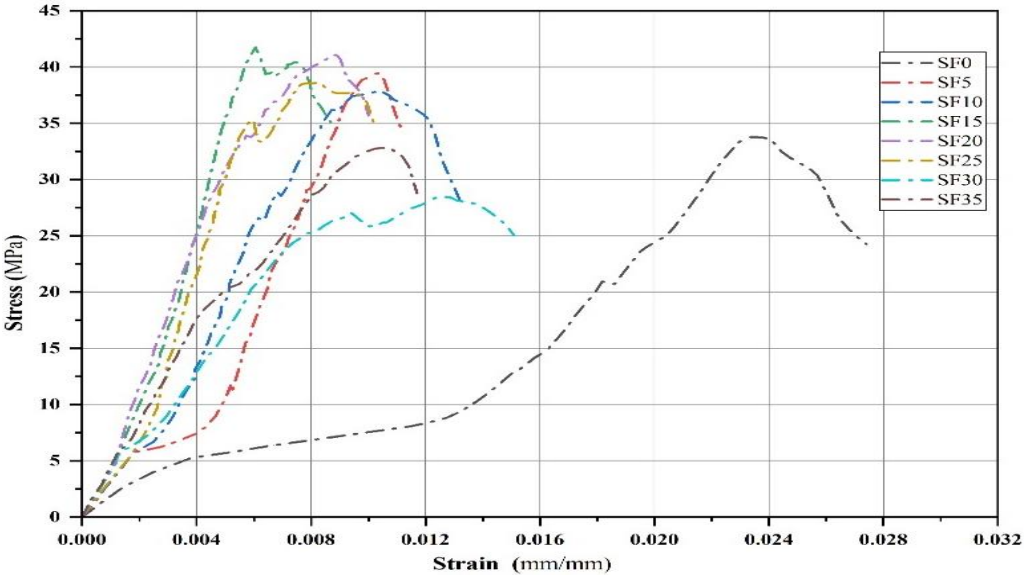

Fig. 16. Stress-strain curve for the groups cured in 5% Na_2So_4 solution.

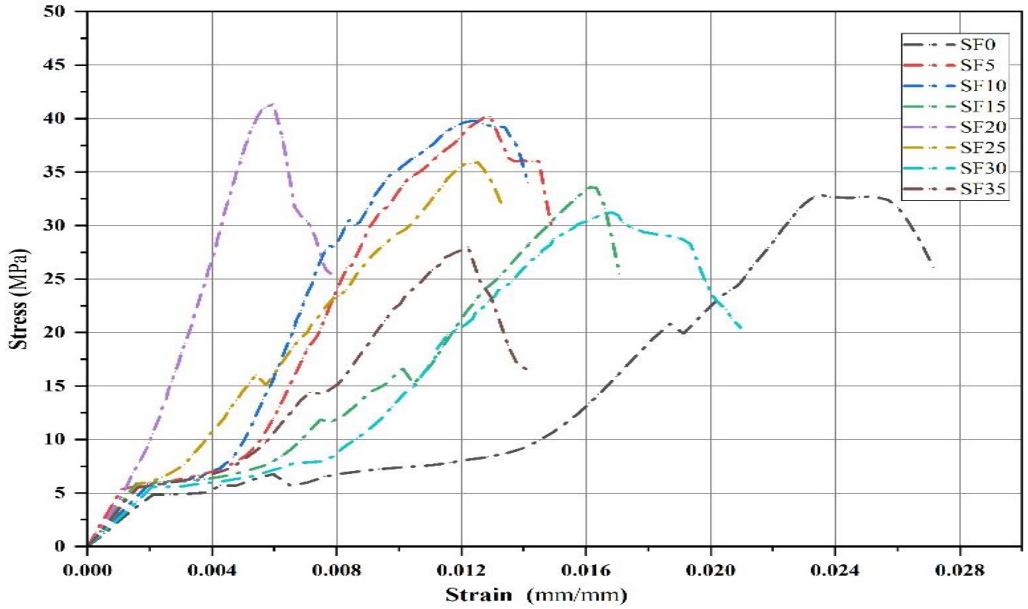

Fig. 17. Stress-strain curve for the groups cured in 10% Na_2So_4 solution.

3.8. Flexural strength

The results of flexural test for specimens submerged in water were calculated as the average of three samples from each group as shown in Fig. 18. The flexural strength results for cement mortars with varying silica fume contents indicate a moderate performance under normal curing conditions, with values ranging from 7.03 MPa at 0% silica fume to a peak of 8.91 MPa at 5%. However, the observed decline in flexural strength at higher silica fume contents, specifically at 10% (8.44 MPa), 15% (7.6 MPa), and beyond, suggests that excessive silica fume may lead to a more brittle mix with reduced flexural capacity.

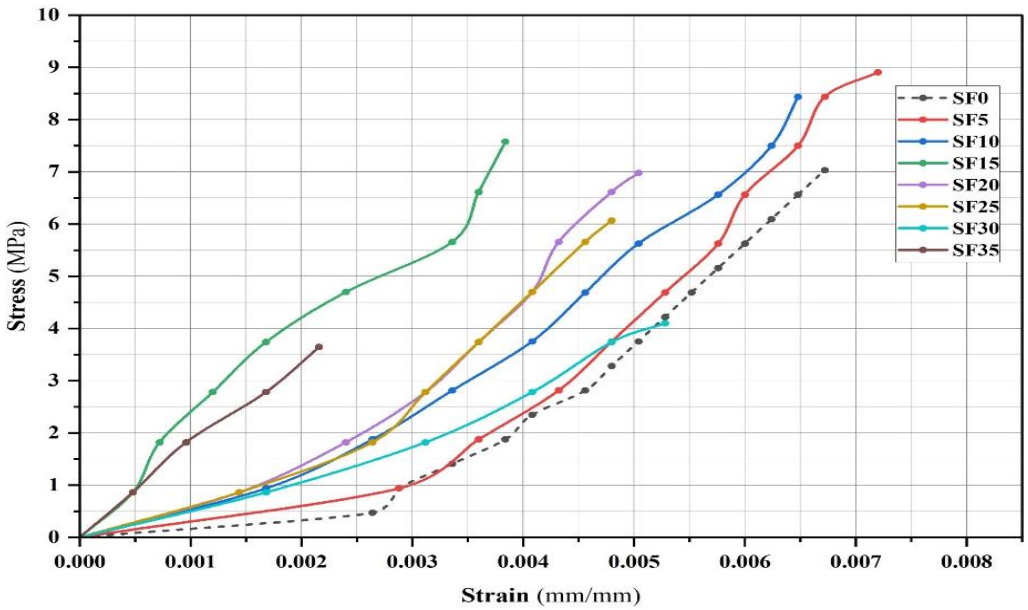

Fig. 18. Stress-strain curve for the water cured samples in 3-point test.

Furthermore, the decrease in flexural strength at higher silica fume levels is also supported by the lower values observed at 20% (6.98 MPa), 25% (6.06 MPa), 30% (4.1 MPa), and 35% (3.64 MPa). These results indicate a significant reduction in the material's ability to withstand bending stresses, highlighting the diminishing returns of silica fume as a partial replacement for cement. The increased brittleness at higher percentages may be due to the high silica fume content creating a dense, but less flexible, structure that is more susceptible to crack propagation under load (Hamada et al. 2023).

The maximum flexural strength of 8.91 MPa at 5% silica fume corresponds with a compressive strength peak of 53.1 MPa under similar water curing conditions, highlighting how the optimal silica fume content can enhance both properties effectively.

However, as the silica fume content increases beyond 5%, a notable decline in both flexural and compressive strengths occurs, particularly at 10% (8.44 MPa flexural) and 15% (7.6 MPa flexural), which correlates with a decrease in compressive strength (46.8 MPa and 40.7 MPa, respectively). This trend suggests that while moderate amounts of silica fume enhance strength, excessive content can lead to increased brittleness and reduced ductility, impacting the material's overall performance under both compressive and flexural loads (Lou et al. 2023).

The lower flexural strength values observed at higher silica fume levels, such as 6.98 MPa at 20% and 3.64 MPa at 35%, correspond with significant drops in compressive strength, indicating that the microstructural integrity may be compromised due to the high pozzolanic content.

4. Conclusions

This study aimed to investigate the effects of varying silica fume contents on cement mortar properties, including compressive strength, flexural strength, modulus of elasticity, and UPV, under different curing conditions. The findings provide insight into the effectiveness of silica fume as a partial cement replacement and highlight the importance of environmental factors in determining the performance of these mortars. The following points are highlighted:

- Peak compressive strength of 53.1 MPa was observed at 5% silica fume content under water curing, indicating enhanced strength due to improved microstructure, while a general decline in compressive strength was noted at higher silica fume levels, with values dropping to 36.8 MPa at 35%, suggesting increased brittleness and microcracking at excessive silica fume contents.
- Flexural strength reached a maximum of 8.91 MPa at 5% silica fume, correlating with the highest compressive strength, which emphasizes the role of silica fume in enhancing ductility. While a significant reduction in flexural strength was noted at higher percentages, with values falling to 3.64 MPa at 35%, reflecting the negative impact of excessive silica fume on the material's ability to resist bending.
- The modulus of elasticity peaked at 12.3 GPa for the water-cured specimens at 10% silica fume, supporting the enhanced stiffness observed with optimal silica fume levels. While exposure to harmful environments, such as 5% and 10% Na_2SO_4 and NaCl solutions, led to substantial decreases in modulus values, with the lowest recorded at 2.7 GPa in 10%Na_2SO_4, indicating significant degradation of the material's mechanical properties.
- The compressive and flexural strengths, as well as modulus values, significantly declined in saline and sulphate environments, highlighting the vulnerability of silica fume-enhanced mortars to chemical attack.
- Results showed that while silica fume can enhance performance, excessive content in harmful environments can lead to severe reductions in mechanical properties, emphasizing the need for careful material design.

In addition, recommendations for the further research could be summarized as following:

- Conduct long-term exposure tests to evaluate the durability of silica fume-enhanced mortars in aggressive environments over extended periods.
- Perform detailed microstructural investigations using techniques such as scanning electron microscopy (SEM) or X-ray diffraction (XRD) to better understand the interactions between silica fume and cementitious materials.
- Investigate the effectiveness of protective coatings or sealers that could enhance the resistance of silica fume mortars to chemical attacks, such as saline and sulphate environments.
- Assess the behaviour of silica fume-enhanced mortars under various loading conditions.
- Conduct a cost-benefit analysis of incorporating silica fume in cementitious materials to determine its economic advantages.

Acknowledgements
None declared.

Funding
The authors received no financial support for the research, authorship, and/or publication of this manuscript.

Conflict of Interest
The authors declared no potential conflicts of interest with respect to the research, authorship, and/or publication of this manuscript.

Author Contributions
All of the authors made substantial contributions to conception and design, or acquisition of data, or analysis and interpretation of data; were involved in drafting the manuscript or revising it critically for important intellectual content; and gave final approval of the version to be published.

Data Availability
The datasets created and/or analyzed during the current study are not publicly available, but are available from the corresponding author upon reasonable request.

References

Abed M, Nasr M, Hasan Z (2018). Effect of silica fume/binder ratio on compressive strength development of reactive powder concrete under two curing systems. *MATEC Web of Conferences*, 162, 02022.

Alameri I, Oltulu M, Ardahanlı M (2020). Influence of preheating on the mechanical properties of high strength concrete with micro silica filler. *Bilecik Seyh Edebali University Journal of Science*, 7(2), 1084-1093.

Al-Saffar FY, Wong LS, Paul SC (2023). An elucidative review of the nanomaterial effect on the durability and calcium-silicate-hydrate (CSH) gel development of concrete. *Gels*, 9(8), 613.

Anwar M (2005). Effect of cementitious materials on concrete against sulfate attack. *Engineering Research Journal*, 99, C92-C104.

ASTM C109/C109M-20 (2020). Standard test method for compressive strength of hydraulic cement mortars (using 2-in. or [50-mm] cube specimens). ASTM International, West Conshohocken, PA.

ASTM C143/C143M-20 (2020). Standard test method for slump of hydraulic-cement concrete. ASTM International, West Conshohocken, PA.

ASTM C150/C150M-24 (2024). Standard specification for portland cement. ASTM International, West Conshohocken, PA.

ASTM C597-22 (2022). Standard test method for ultrasonic pulse velocity through concrete. ASTM International, West Conshohocken, PA.

ASTM C642-21 (2021). Standard Test method for density, absorption, and voids in hardened concrete. ASTM International, West Conshohocken, PA.

ASTM C1585-20 (2020). Standard test method for measurement of rate of absorption of water by hydraulic-cement concretes. ASTM International, West Conshohocken, PA.

ASTM D790-17 (2017). Standard test methods for flexural properties of unreinforced and reinforced plastics and electrical insulating materials. ASTM International, West Conshohocken, PA.

ASTM E494-20 (2020). Standard practice for measuring ultrasonic velocity in materials by comparative pulse-echo method. ASTM International, West Conshohocken, PA.

Atabey İ, Çelikten S, Canbaz M (2023). Chemical resistance of hardened mortar containing andesite and marble industry waste powder. *Challenge Journal of Concrete Research Letters*, 14(2), 31-38.

Atasever M, Tokyay M (2024). Determining datum temperature and apparent activation energy: an approach for mineral admixtures incorporated cementitious systems. *Challenge Journal of Concrete Research Letters*, 15(4), 142-149.

Feng L, Zhao P, Wang Z, Gao J, Su X, Li H (2018). Improvement of mechanical properties and chloride ion penetration resistance of cement pastes with the addition of pre-dispersed silica fume. *Construction and Building Materials*, 182, 483-492.

Güney B, Yıldızel S (2024). Optimization of mechanical properties in lime-based composites using the Taguchi method. *Challenge Journal of Structural Mechanics*, 10(3), 109-115.

Hamada HM, Abed F, Katman HYB, Humada AM, AlJawahery MS, Majdi A, Yousif ST, Thomas BS (2023). Effect of silica fume on the properties of sustainable cement concrete. *Journal of Materials Research and Technology*, 24, 8887-8908.

Han M, Li J (2024). Enhancement of compressive strength and durability of sulfate-attacked concrete. *Buildings*, 14(7), 2187.

Harirchian E (2024). Predicting compressive strength of AAC blocks through machine learning advancements. *Challenge Journal of Concrete Research Letters*, 15(2), 56-68.

Lee, FH, Lee Y, Chew SH, Yong KY. (2005). Strength and modulus of marine clay-cement mixes. *Journal of Geotechnical and Geoenvironmental Engineering*, 131(2), 178–186.

Lou Y, Khan K, Amin MN, Ahmad W, Deifalla AF, Ahmad A (2023). Performance characteristics of cementitious composites modified with silica fume: A systematic review. *Case Studies in Construction Materials*, 18, e01753.

McCarthy MJ, Dyer TD (2019). Pozzolanas and pozzolanic materials. *In: Hewlett PC, Liska M, editors*. Lea's Chemistry of Cement and Concrete (5th edition), Butterworth-Heinemann, Oxford, United Kingdom, 363-467.

Ortega JM, Esteban MD, Williams M, Sánchez I, Climent MÁ (2018). Short-term performance of sustainable silica fume mortars exposed to sulfate attack. *Sustainability*, 10(7), 2517.

Ramezanianpour, AA, Riahi Dehkordi E, Ramezanianpour AM (2020). Influence of sulfate ions on chloride attack in concrete mortars containing silica fume and jajrood trass. *Iranian Journal of Science and Technology, Transactions of Civil Engineering*, 44(4), 1135–1144.

Saif Allah JS, Kassim MM, Salman GA (2024). The durability of concrete mortars with different mineral additives exposed to sulfate attack. *Salud, Ciencia y Tecnología - Serie De Conferencias*, 3, 851.

Shannag M, Shaia HA (2003). Sulfate resistance of high-performance concrete. Cement and Concrete Composites, 25(3), 363-369.

Sharaky IA, Megahed FA, Seleem MH, Badawy AM (2019). The influence of silica fume, nano silica and mixing method on the strength and durability of concrete. *SN Applied Sciences*, 1(6), 575.

Shetti, AP, Das BB. (2015). Acid, alkali and chloride resistance of early age cured silica fume concrete. *In: Matsagar V, editor.* Advances in Structural Engineering. Springer India, New Delhi, India, 1849-1862.

Şimşek O, Aruntaş HY, Demir İ, Yaprak H, Yazıcıoğlu S (2022). Investigation of the effect of seawater and sulfate on the properties of cementitious composites containing silica fume. *Silicon*, 14(2), 663–675.

Tripathi D, Kumar R, Mehta PK, Singh A (2020). Silica fume mixed concrete in acidic environment. *Materials Today: Proceedings*, 27, 1001–1005.

Zhou ZY, Gencturk B, Willam K, Attar A (2015). Carbonation-induced and chloride-induced corrosion in reinforced concrete structures. *Journal of Materials in Civil Engineering*, 27(9), 04014245.